

Polyol Synthesis and Characterization of Magnetic Nanocrystalline Cobalt and Cobalt Platinum

by

Erick Edgardo Chávarri Pajares

A thesis submitted in partial fulfillment of the requirements for the degree of

MASTER OF SCIENCES
in
MECHANICAL ENGINEERING

UNIVERSITY OF PUERTO RICO
MAYAGÜEZ CAMPUS
2007

Approved by:

Oscar Perales Perez, PhD
President, Graduate Committee

Date

Gustavo Gutiérrez, PhD
Member, Graduate Committee

Date

Paul A. Sundaram, PhD
Member, Graduate Committee

Date

Paul A. Sundaram, PhD
Chairperson of the Department

Date

Carlos Rinaldi, PhD
Representative of Graduate Studies

Date

ABSTRACT

The present work addresses the systematic study of the synthesis and characterization of cobalt nanoparticles produced in polyol solutions. The kinetics of the metal forming reaction strongly influenced the stability conditions of cobalt phases. The control of the reaction kinetics was achieved through a suitable selection of the solution chemistry in the Polyol–Co (II) system. The addition of hydroxyl ions into the cobalt polyol solution under boiling conditions not only accelerated the formation of the magnetic phase but also affected the stability conditions of the metallic precipitate. Depending on the OH/Co mole ratio and the type of cobalt salt, hexagonal close packed (hcp), face centered cubic (fcc), and metastable pseudo-cubic epsilon cobalt (ϵ -Co) phases were formed. Highly monodisperse ϵ -Co nanoparticles were produced when cobalt acetyl-acetonate salt was used instead of the acetate alone. Furthermore, the presence of Pt ions –added to promote heterogeneous nucleation- caused a dramatic shortening of the time required for the complete formation of the magnetic phase. The shortening in reaction time was conducive to the formation of the ordered face centered tetragonal (fct)-CoPt nanoparticles although co-existing with fcc and ϵ -Co structures. Excess of platinum was present as fcc-Pt. The room-temperature saturation magnetization (M_s) and coercivity (H_c) of the nanocrystalline cobalt powders ranged from 80 to 110 emu/g and 101 to 211 Oe, respectively. The coercivity was as high as 248 Oe when CoPt was present. The co-existence of Pt ions in starting solutions not only promoted the nucleation rate and

accelerated the cobalt reduction but also induced the formation of ordered fct-CoPt nanocrystals at low temperature (487 K).

RESUMEN

El presente trabajo se enfoca en el estudio sistemático de la síntesis y caracterización de nanopartículas de cobalto producidas en soluciones de polyol. La cinética de la reacción de formación de metal influencia fuertemente las condiciones de estabilidad de las fases de cobalto. El control de la cinética de reacción fue lograda a través de la selección adecuada de la solución química en el sistema polyol-Co (II). La adición de iones hidroxilo dentro de la solución de polyol y cobalto bajo condiciones de ebullición no solo acelera la formación de la fase magnética también afecta la estabilidad de las condiciones del metal precipitado. Dependiendo de la razón molar OH/Co y del tipo de sal de cobalto, se formaron estructuras de empaquetamiento hexagonal compacto (hcp), cúbica centrada en las caras (fcc) y meta estable pseudo -cúbica épsilon-cobalto (ϵ -Co). Altamente nanopartículas monodispersas de ϵ -Co fueron producidas cuando la sal de cobalto acetil acetato fue empleada en vez de la sal de acetato. Además, la presencia de iones de Pt - adicionadas para promover la nucleación heterogénea- causan el dramático acortamiento del tiempo requerido para la formación completa de la fase magnética. El acortamiento del tiempo de reacción indujo a la formación de nanopartículas ordenadas tetragonales centradas en las caras (fct)-CoPt con la coexistencia de las estructuras fcc y ϵ -Co. Exceso de platino estuvo presente como fcc-Pt. La magnetización de saturación a temperatura ambiente (M_s) y la coersitividad (H_c) de los polvos nanocristalinos de cobalto estuvieron en un rango de 80 a 110 emu/g y 101 a 211 Oe respectivamente. La coersitividad fue tan

alta como 248 Oe cuando CoPt estuvo presente. La coexistencia de iones Pt en la solución inicial no solo promueve la razón de nucleación y acelera la reducción de cobalto además induce la formación de nanocristales ordenados fct-CoPt a baja temperatura (487 K).

Dedicated to my parents María Yolanda and Antero.

ACKNOWLEDGEMENTS

During the development of my graduate studies in the University of Puerto Rico several persons and institutions collaborated directly and indirectly with my research. Without their support it would have been impossible for me to finish my work. Hence, I wish to dedicate this section to recognizing their support.

I want to start expressing a sincere acknowledgement to my advisor, Dr. Oscar Juan Perales-Perez because he gave me the opportunity to research under his guidance and supervision. I received motivation; encouragement and support from him during all my studies. With him, I learned the importance of the nanotechnology.

This material is based upon work supported by the NSF under Grant No. 0351449. Any opinions, findings and conclusions or recommendations expressed in this material are of the author and do not necessarily reflect the views of the National Science Foundation (NSF). Thanks are also extended to NSF-Start Up Program for providing partial support for this research. We also appreciate the support from Eric Calderón with SQUID measurements and José Almodovar for SEM images.

Table of Contents

ABSTRACT	II
RESUMEN	IV
ACKNOWLEDGEMENTS	VII
TABLE OF CONTENTS.....	VIII
LIST OF ABBREVIATIONS.....	X
LIST OF TABLES.....	XII
LIST OF FIGURES	XIII
1 INTRODUCTION	19
1.1 MOTIVATION.....	19
1.2 OBJECTIVES	19
1.3 CONTENTS OF THE THESIS	20
2 THEORETICAL BACKGROUND.....	21
2.1 INTRODUCTION TO MAGNETISM	21
2.1.1 <i>Origin of magnetism</i>	21
2.1.2 <i>Types of magnetism</i>	23
2.1.3 <i>Magnetization</i>	26
2.1.4 <i>Origin of coercivity</i>	28
2.1.5 <i>Magnetic hysteresis loop</i>	30
2.1.6 <i>Magnetic anisotropy</i>	33
2.2 COBALT AND COBALT-PLATINUM ALLOYS	34
2.2.1 <i>Magnetic materials for data storage applications</i>	34
2.2.2 <i>Cobalt and Cobalt Platinum alloys as magnetic materials</i>	35
2.2.3 <i>Crystallography of Cobalt Platinum ordered phase</i>	40
2.2.4 <i>CoPt phase stability diagram</i>	41
2.3 THE POLYOL PROCESS	42
2.3.1 <i>Introduction</i>	42
2.3.2 <i>Structural, physical, and chemical properties of polyols</i>	43
2.3.3 <i>Thermodynamics of the polyol process</i>	45
2.3.4 <i>General mechanism of the reduction reaction in polyols</i>	48
2.3.5 <i>Related Works of Cobalt and Cobalt Platinum in Polyols</i>	51
2.4 FUNDAMENTALS OF MATERIALS CHARACTERIZATION TECHNIQUES.....	52
2.4.1 <i>X-Ray diffractometry</i>	52
2.4.2 <i>Scanning Electron Microscopy</i>	58
2.4.3 <i>SQUID (Super Quantum Interference Device) Magnetometer</i>	60
3 EXPERIMENTAL	62

3.1	MATERIALS	62
3.2	EXPERIMENTAL PROCEDURE	62
3.3	CHARACTERIZATION TECHNIQUES	64
4	RESULTS AND DISCUSSION	66
4.1	EFFECT OF THE TYPE OF POLYOL	66
4.1.1	<i>Structural characterization</i>	66
4.1.2	<i>Magnetic characterization</i>	69
4.1.3	<i>Morphological analyses</i>	73
4.2	EFFECT OF THE OH/CO MOLE RATIO AND TYPE OF COBALT SOURCE	77
4.2.1	<i>Structural characterization</i>	77
4.2.2	<i>Morphological analyses</i>	84
4.2.3	<i>Magnetic characterization</i>	98
4.3	EFFECT OF THE CONCENTRATION OF CO IONS	101
4.3.1	<i>Structural characterization</i>	101
4.3.2	<i>Magnetic characterization</i>	108
4.4	EFFECT OF THE CO-EXISTENCE OF PT IONS IN STARTING SOLUTIONS	109
4.4.1	<i>Hexachloro-platinate as source of platinum ions</i>	110
i)	<i>Structural characterization</i>	110
ii)	<i>Morphological analyses</i>	113
iii)	<i>Magnetic characterization</i>	115
4.4.2	<i>Platinum acetyl-acetonate as source of platinum ions</i>	118
i)	<i>Structural characterization</i>	118
ii)	<i>Magnetic characterization</i>	125
5	CONCLUDING REMARKS	127
	REFERENCES.....	130

List of abbreviations

a	lattice parameter of the crystalline structure
Å	angstroms
A.U.	arbitrary units
BP	boiling point
c	lattice parameter of the crystalline structure different of the other “a”
Co	cobalt
Cu	cooper
Co(ac) ₂	cobalt acetate
Co(acac) ₂	cobalt acetylacetonate
CoPt	cobalt platinum alloy
CoPtCr	cobalt platinum chromium
DC	direct current
°C	degree Celsius
d	interplanar distance
D _p	minimal grain size for data storage times of 10 years
EA	easy axis
EDS	Energy Dispersive Spectroscopy.
EDX	Energy dispersive x-ray.
EG	ethylene glycol
EPMA	Electron probe Microanalysis.
emu/g	electromagnetic unit per gram
erg	a cgs unit of energy equal to 10 ⁻⁷ joules
ε-Co	epsilon cobalt
fcc	face centered cubic
fct	face centered tetragonal
FePd	iron palladium alloy
FePt	iron platinum alloy
Fe ₁₄ Nd ₂ B	iron neodymium boron alloy
g	gram
Gb/in ²	gigabits (10 ⁹ bits) per square inch
hcp	hexagonal close packing
(h k l)	Miller index of a crystallographic plane
H	magnetic field expressed in Oe
H _c	coercivity expressed in Oe
H ₂ PtCl ₆	hexa-chloroplatinate
W-H	Williamson Hall
K	Degree Kelvin
K _α	s orbital
KOe	kilo Oersted

K_u	constant of uniaxial crystalline anisotropy expressed in erg/cm^3
KV	kilovolts
λ	wavelength
M	molarity (mole per liter)
mA	miliampere
ml	milliliter
μm	micrometer
M_r	remanent magnetization
M_s	saturation magnetization
MnAl	manganese aluminum alloy
MPMS	magnetic properties measurement system
n	smallest entire value of λ ($n=1$)
nm	a nanometer equal to 10^{-9} m or 10 \AA
NaOH	sodium hydroxide
Oe	Oersted
OH/Co	molar ratio of hydroxyl ions to cobalt
R	equal to OH/Co mole ratio
SmCo_5	samarium cobalt alloy
SEM	scanning electron microscopy
SQUID	superconducting quantum interference device
t	crystallite size
torr	Torricelli, a unit of pressure equal to 1 mm of mercury
T	Tesla, a unit of magnetic induction equal 10^4 Gauss
TEG	triethylene glycol
TMEG	trimethylene glycol
TREG	tetraethylene glycol
UPRM	University of Puerto Rico at Mayagüez
VSM	vibrating sample magnetometer
XRD	X-ray diffractometer

List of tables

Tables	Page
TABLE 2.1: The electron spins in Co and Pt, with arrows indicating the positive and negative direction of the spin.	22
TABLE 2.2: Representation of the orientation of magnetic moment vector () in a domain () for different types of magnetic behavior of the materials when external magnetic field () is applied.	25
TABLE 2.3: Conversion factors and units used in this thesis.	26
TABLE 2.4: Characteristic hysteresis loop for different types of magnetic behavior.....	32
TABLE 2.5: Alloy systems for data storage [7].	35
TABLE 2.6: Atomic coordinates in the unit cell of ϵ -Co structure.	37
TABLE 2.7: Magnetic properties of bulk (hcp-fcc) cobalt.....	37
TABLE 2.8: Reported values of coercivity in equiatomic CoPt.	40
TABLE 2.9: Properties of some polyols: Comparison with water and monoalcohols under atmospheric pressure [21].	44
TABLE 2.10: General mechanism of Co(OH)_2 reduction by ethyleneglycol.	49
TABLE 4.1: Reported values of magnetic properties for as synthesized cobalt particles in different polyols using SQUID at 300 K.	70
TABLE 4.2: Reported values of magnetic properties for cobalt particles as synthesized using SQUID at 300 K.	99
TABLE 4.3: Comparison of the lattice parameter and crystallite size of as-synthesized ϵ -Co powders from 0.005 M Co solutions using Co(acac)_2 precursor, TMEG at 487 ± 5 K.	106
TABLE 4.4: Comparison of the lattice parameter and crystallite size of as-synthesized ϵ -Co powders from 0.0025 M Co solutions using Co(acac)_2 precursor, TMEG at 487 ± 5 K.	106

List of figures

Figures	Page
Figure 2.1: Origin of magnetic dipoles: a) the spin of the electron produces a magnetic field. b) Outer unfilled electron shells orbiting about the core (protons, neutrons and inner filled electron shells) create a magnetic field about the atom.....	22
Figure 2.2: Domains and domain-walls in magnetic materials.....	23
Figure 2.3: Regions in the M-H variation. I: Partial magnetization by domain-wall movement; II: Irreversible rotation of domain magnetization; III: Magnetic saturation. Adapted from reference [2].	27
Figure 2.4: Schematic variation of coercivity with particle size. The scale at the bottom shows critical sizes for cobalt. MD: multi-domain region; SD: single domain region and SPM: superparamagnetic region. Adapted from references [4][5].	29
Figure 2.5: Magnetization (M) vs. Applied Field (H) hysteresis loop. Adapted from reference [2].	30
Figure 2.6: Cobalt structures: (a) fcc structure, (b) ϵ -Co structure, cubic cell filled with eight atoms of Type I (red) and twelve atoms of Type II (blue), and (c) hcp structure.....	38
Figure 2.7: Allotropic transformation of nanocrystalline cobalt [12].	39
Figure 2.8: Unit cells of a) fct-CoPt type, and b) fcc-CoPt ₃ type superstructures.	41
Figure 2.9: Phase diagram of Co-Pt system [12].	42
Figure 2.10: Calculated ΔG of reduction (ΔG_{red}) in ethylene glycol at 473 K for various hydroxides assuming a total oxidation of the alcohol and the formation of the metal according to reaction [26]. The shadowed and no shadowed labels indicate experimentally nonreduced and reduced hydroxides, respectively. Dashed frames indicate unstable hydroxides [10].	47
Figure 2.11: Reaction steps and intermediate phases observable during the reaction of various oxides in EG. Adapted from reference [10].	47
Figure 2.12: LaMer's model for the formation of a monodisperse system: I-precursor formation step; II-nucleation step; III-growth step [28].	50
Figure 2.13: Schematic representation of the X-ray diffraction, the incoming x-rays (red) diffract with θ angle (blue) in the lattice of the material and only the waves in face can be detected.	53
Figure 2.14: (a) Schematic representation of the X-ray diffractometer; (b) Photograph of XRD SIEMENS D500, available on the materials research laboratory at UPRM.	57

Figure 2.15: (a) Schematic representation of the SEM [34]; (b) Scanning Electron Microscopy (JEOL model JSM-5410 LV available in the Biology microscopy laboratory at UPRM).....	59
Figure 2.16: (a) Schematic representation of the SQUID unit; (b) Photograph of Quantum Design MPMSXL available at UPRM.....	61
Figure 3.1: Experimental set-up for the synthesis in polyol.	63
Figure 3.2: Experimental procedure for the synthesis of Co nanoparticles.....	65
Figure 4.1: XRD patterns of intermediate and cobalt powders synthesized at different reaction times in TEG, from 0.01M Co solution using $\text{Co}(\text{ac})_2$, TEG and 'R' = 45. Peaks corresponding to fcc (●) cobalt phase is indicated.	67
Figure 4.2: XRD patterns of as-synthesized cobalt powders from 0.01M Co solutions using $\text{Co}(\text{ac})_2$ and EG (BP = 468 K), TEG (BP = 551 K) and TMEG (BP = 487 K) at 468 ± 5 K, with 'R' = 45 and the suitable reaction time to obtain metallic precipitates. Peaks corresponding to fcc (●), hcp () and ϵ (■) cobalt phases are indicated.....	69
Figure 4.3: M-H loops for Co powders as-synthesized from 0.01M Co solution using $\text{Co}(\text{ac})_2$, EG at 468 ± 5 K, 'R' = 45 and 64 minutes of reaction time. The insert show the M-H loop around the origin.....	71
Figure 4.4: M-H loops for Co powders as-synthesized from 0.01M Co solution using $\text{Co}(\text{ac})_2$, TEG at 468 ± 5 K, 'R' = 45 and 83 minutes of reaction time. The insert show the M-H loop around the origin.....	71
Figure 4.5: M-H loops for Co powders as-synthesized from 0.01M Co solution using $\text{Co}(\text{ac})_2$, TMEG at 487 ± 5 K, 'R' = 45 and 240 minutes of reaction time. The insert show the M-H loop around the origin.....	72
Figure 4.6: SEM images of cobalt particles synthesized from 0.01M Co solution using $\text{Co}(\text{ac})_2$ as metal salt, EG at 468 ± 5 K, 'R' = 45 and 64 min. of reaction time. The scale bar in a) represents 10 μm and in the detail b) represents 1 μm	74
Figure 4.7: SEM images of cobalt particles synthesized from 0.01M Co solution using $\text{Co}(\text{ac})_2$ as metal salt, TMEG at 487 ± 5 K, 'R' = 30 and 83 min. of reaction time. The scale bar in a) represents 10 μm and in the detail b) represents 1 μm	75
Figure 4.8: SEM images of cobalt particles synthesized from 0.01M Co solution using $\text{Co}(\text{ac})_2$ as metal salt, TMEG at 487 ± 5 K, 'R' = 40 and 240 min of reaction time. The scale bar in a) represents 10 μm and in the detail b) represents 1 μm	76
Figure 4.9: XRD patterns of as-synthesized intermediate compound (like hydroxy-alkoxide) of cobalt powders from 0.01M Co solutions using $\text{Co}(\text{ac})_2$ and $\text{Co}(\text{acac})_2$ salt precursors in TMEG at 210 ± 5 °C.....	80
Figure 4.10: XRD patterns of as-synthesized intermediate compound (like hydroxy-alkoxide) of cobalt powders from 0.01M Co solutions using $\text{Co}(\text{ac})_2$ and $\text{Co}(\text{acac})_2$ salt precursors in TMEG at 210 ± 5 °C.....	80

Figure 4.11: XRD patterns of as-synthesized cobalt powders from 0.01M Co solutions using $\text{Co}(\text{ac})_2$ and $\text{Co}(\text{acac})_2$ precursors, TMEG at 210 ± 5 °C. Peaks corresponding to fcc (●), hcp () and ϵ (■) cobalt phases are indicated.	81
Figure 4.12: XRD patterns of as-synthesized cobalt powders from 0.01M Co solutions using $\text{Co}(\text{ac})_2$ and $\text{Co}(\text{acac})_2$ precursors, TMEG at 210 ± 5 °C. Peaks corresponding to fcc (●), hcp () and ϵ (■) cobalt phases are indicated.	81
Figure 4.13: XRD patterns of as-synthesized cobalt powders from 0.01M Co solutions using $\text{Co}(\text{ac})_2$ and $\text{Co}(\text{acac})_2$ precursors, TMEG at 210 ± 5 °C. Peaks corresponding to fcc (●), hcp () and ϵ (■) cobalt phases are indicated.	82
Figure 4.14: Comparative results. XRD patterns of as-synthesized cobalt powders from 0.01M Co solutions using: a) $\text{Co}(\text{ac})_2$, and b) $\text{Co}(\text{acac})_2$ precursors and 4 h of reaction time. Peaks corresponding to fcc (●), hcp () and ϵ (■) cobalt phases are indicated. Peaks corresponding to the sample produced at 'R'=0 correspond to a family of hydroxide-alkoxide compounds.	83
Figure 4.15: SEM images of bi-pyramidal intermediate (hydroxi-alkoxides) synthesized from 0.01M Co solution using $\text{Co}(\text{ac})_2$ as salt, TMEG at 483 ± 5 K, 'R' = 0 and 4 h of reaction time.	87
Figure 4.16: SEM images of dissolved intermediate synthesized from 0.01M Co solution using $\text{Co}(\text{ac})_2$ as salt, TMEG at 483 ± 5 K, 'R' = 10 and 4 h of reaction time.	88
Figure 4.17: SEM images of cobalt particles synthesized from 0.01M Co solution using $\text{Co}(\text{ac})_2$ as metal salt, TMEG at 483 ± 5 K, 'R' = 30 and 4 h of reaction time.	89
Figure 4.18: SEM images of cobalt particles synthesized from 0.01M Co solution using $\text{Co}(\text{ac})_2$ as metal salt, TMEG at 483 ± 5 K, 'R' = 40 and 4 h of reaction time.	90
Figure 4.19: SEM images of cobalt particles synthesized from 0.01M Co solution using $\text{Co}(\text{ac})_2$ as salt, TMEG at 483 ± 5 K, 'R' = 50 and 4 h of reaction time.	91
Figure 4.20: SEM images of dissolved intermediate synthesized from 0.01M Co solution using $\text{Co}(\text{acac})_2$ as salt, TMEG at 483 ± 5 K, 'R' = 0 and 4 h of reaction time.	92
Figure 4.21: SEM images of dissolved intermediate synthesized from 0.01M Co solution using $\text{Co}(\text{acac})_2$ as salt, TMEG at 483 ± 5 K, 'R' = 10 and 4 h of reaction time.	93
Figure 4.22: SEM images of cobalt particles synthesized from 0.01M Co solution using $\text{Co}(\text{acac})_2$ as metal salt, TMEG at 483 ± 5 K, 'R' = 30 and 4 h of reaction time.	94
Figure 4.23: SEM images of cobalt particles synthesized from 0.01M Co solution using $\text{Co}(\text{acac})_2$ as metal salt, TMEG at 483 ± 5 K, 'R' = 40 and 4 h of reaction time.	95

Figure 4.24: SEM images of cobalt particles synthesized from 0.01M Co solution using $\text{Co}(\text{acac})_2$ as metal salt, TMEG at 483 ± 5 K, 'R' = 50 and 4 h of reaction time.	96
Figure 4.25: SEM images of cobalt particles synthesized in TMEG at 483 ± 5 K with different 'R' values and using $\text{Co}(\text{ac})_2$ as source of cobalt ions: a) 'R' = 0; b) 'R' = 10 and c) 'R' = 50. The scale bar represents 10 μm	97
Figure 4.26: SEM images of cobalt particles synthesized in TMEG at 483 ± 5 K with different conditions using $\text{Co}(\text{acac})_2$ as source of cobalt ions: a) 'R' = 0; b) 'R' = 10 and c) 'R' = 50. The scale bar represents 10 μm	97
Figure 4.27: M-H loops for Co powders synthesized from 0.01M $\text{Co}(\text{ac})_2$, 'a', or 0.01M $\text{Co}(\text{acac})_2$, 'b', solutions. The insert show the M-H loop around the origin.	100
Figure 4.28: M-H loops for Co powders synthesized from 0.01M $\text{Co}(\text{ac})_2$, 'a', or 0.01M $\text{Co}(\text{acac})_2$, 'b', solutions. The insert show the M-H loop around the origin.	100
Figure 4.29: M-H loops for Co powders synthesized from 0.01M $\text{Co}(\text{ac})_2$, 'a', or 0.01M $\text{Co}(\text{acac})_2$, 'b', solutions. The insert show the M-H loop around the origin.	101
Figure 4.30: XRD patterns for 0.005 M Co particles synthesized from different precursors, TMEG at 487 ± 5 K. The reaction time was 4 hours and 'R' = 50. Peaks corresponding to CoO (\square), Co_2O_3 (\circ) and fcc (\bullet), hcp (\mid), ϵ (\blacksquare) cobalt phases are indicated.	105
Figure 4.31: XRD patterns for 0.0025 M Co particles synthesized from different precursors, TMEG at 487 ± 5 K. The reaction time was 4 hours and 'R' = 50. Peaks corresponding to CoO (\square), Co_2O_3 (\circ) and fcc (\bullet), hcp (\mid), ϵ (\blacksquare) cobalt phases are indicated.	105
Figure 4.32: Williamson Hall's plot for ϵ -Co sample for 0.005 M Co particles synthesized from $\text{Co}(\text{acac})_2$, TMEG at 487 ± 5 K. The reaction time was 4 hours and 'R' of 50.	107
Figure 4.33: Williamson Hall's plot for ϵ -Co sample for 0.0025 M Co particles synthesized from $\text{Co}(\text{acac})_2$, TMEG at 487 ± 5 K. The reaction time was 4 hours and 'R' of 50.	107
Figure 4.34: M-H loop for ϵ -Co powder synthesized from 0.0025 M $\text{Co}(\text{acac})_2$ in TMEG at 487 ± 5 K. The insert show the M-H loop around the origin.	109
Figure 4.35: M-H loop for ϵ -Co powder synthesized from 0.01 M $\text{Co}(\text{acac})_2$ in TMEG at 487 ± 5 K. The insert show the M-H loop around the origin.	109
Figure 4.36: XRD pattern of as-synthesized Co particles at 'R'= 50, a Pt/Co mole ratio of 0.15 in TMEG at 487 ± 5 K. XRD analysis revealed the coexistence of hcp (\mid), ϵ (\blacksquare); fcc-Pt (∇) and ordered fct-CoPt (\ast).	111
Figure 4.37 XRD pattern of as-synthesized Co particles at 'R'= 50, a Pt/Co mole ratio of 0.25 in TMEG at 487 ± 5 K. XRD analysis revealed the coexistence of fcc-Pt (∇) and ordered fct-CoPt (\ast). Sharp peaks are from the residual intermediate compound (IC).	112

Figure 4.38: XRD pattern of as-synthesized Co particles at 'R'= 50, a Pt/Co mole ratio of 1.0 in TMEG at 487±5 K. XRD analysis revealed only fcc-Pt (∇). Sharp peaks are from the residual intermediate compound (IC).....	112
Figure 4.39: SEM image of cobalt, platinum and cobalt platinum particles as-synthesized at 'R'= 50, 0.0025 M Co(acac) ₂ , a Pt/Co mole ratio of 0.15 in TMEG at 487±5 K.....	113
Figure 4.40: SEM image of platinum and cobalt platinum particles as-synthesized at 'R'= 50, 0.0015 M Co(acac) ₂ , a Pt/Co mole ratio of 0.25 in TMEG at 487±5 K.	114
Figure 4.41: SEM image of platinum particles as-synthesized at 'R'= 50, 0.0005 M Co(acac) ₂ , a Pt/Co mole ratio of 1.0 in TMEG at 487±5 K.....	114
Figure 4.42: M-H loop for cobalt, platinum and cobalt platinum particles synthesized at 0.0025 M Co(acac) ₂ and a Pt/Co mole ratio of 0.15 in TMEG at 487±5 K. The insert show the M-H loop around the origin.....	116
Figure 4.43: M-H loop for cobalt, platinum and cobalt platinum particles synthesized at 0.0015 M Co(acac) ₂ and a Pt/Co mole ratio of 0.25 in TMEG at 487±5 K. The insert show the M-H loop around the origin.....	117
Figure 4.44: M-H loop for cobalt, platinum and cobalt platinum particles synthesized at 0.0005 M Co(acac) ₂ and a Pt/Co mole ratio of 1.0 in TMEG at 487±5 K. The insert show the M-H loop around the origin.....	117
Figure 4.45: XRD pattern of as-synthesized CoPt particles in TMEG at 487±5 K with 'R'= 50 and a Pt/Co mole ratio of 0.15. XRD analysis revealed only nanocrystalline fct-CoPt (*)......	119
Figure 4.46: XRD pattern match with PDF # 29 0498 using the software phase identification from powder diffraction MATCH v 1.7 of as-synthesized CoPt particles in TMEG at 487±5 K with 'R'= 50 and a Pt/Co mole ratio of 0.15. XRD analysis revealed only nanocrystalline fct-CoPt.....	120
Figure 4.47: XRD pattern of as-synthesized Pt and CoPt particles at 'R'= 50 and a Pt/Co mole ratio of 1.0 in TMEG at 487±5 K. XRD analysis revealed the coexistence of fcc-Pt (∇) and ordered fct-CoPt (*). Non-assigned small peaks are attributed to residual intermediate (IC).....	121
Figure 4.48: XRD patterns at different reaction times of as-synthesized CoPt particles at 'R'= 50, a Pt/Co mole ratio of 0.15 in TMEG at 487±5 K. XRD analysis for 10 min, 1 h and 4 h of reaction time revealed only nanocrystalline fct-CoPt (*)......	123
Figure 4.49: XRD patterns at different reaction times of as-synthesized Pt and CoPt nanocrystalline particles at 'R'= 50, a Pt/Co mole ratio of 1.0 in TMEG at 487±5 K. XRD analysis revealed the coexistence of fcc-Pt (∇) and ordered fct-CoPt (*). Shape picks are from the residual intermediate compound (IC) that disappear in the others patterns.....	124
Figure 4.50: M-H loop for cobalt platinum particles synthesized at 0.0025 M Co(acac) ₂ , a Pt/Co mole ratio of 0.15 in TMEG for a) 10 minutes and b) 1 hour of reaction	

time in TMEG at 487 ± 5 K. The insert show the M-H loop around the origin.	126
Figure 4.51: M-H loop for cobalt platinum particles synthesized at 0.0025 M $\text{Co}(\text{acac})_2$ and a Pt/Co mole ratio of 1.0 in TMEG for a) 10 minutes and b) 1 hour of reaction time in TMEG at 487 ± 5 K. The insert show the M-H loop around the origin.	126

1 INTRODUCTION

1.1 Motivation

The development of high coercivity magnetic nanostructures opens new opportunities for ultra dense memory storage. Control of the physical, chemical, and structural properties of materials at the micro and nanoscale will become indispensable to achieve a fine tuning on materials properties. In the particular case of magnetic nanocrystals, they exhibit strong size-dependent properties that will permit determination of the scaling limits of magnetic storage, a key component of information technology.

From the above considerations, the present thesis was focused on the determination of the most suitable green synthesis approach leading to the tailoring of the magnetic properties in metallic cobalt nanostructures, an indispensable requirement to realize commercially applicable devices.

1.2 Objectives

The objective of the present research can be summarized as follows.

General Objectives:

1) Determination of the influence of the synthesis conditions on particle size and stability of magnetic cobalt phases.

2) Establishment of the relationship between the metal structure, magnetic properties at the micro and nanoscale.

Specific Objectives:

1) Define the influence of the type of polyol on the formation of nanocrystalline cobalt structures.

2) Determine the effect of the type of cobalt precursor, the OH/Co mole ratio and the co-existence of Pt ions on the rate of cobalt and cobalt-platinum alloy formation.

3) Determine the influence of synthesis conditions on the stability of the fcc-, hcp-, epsilon-, and fct-cobalt phases and the corresponding magnetic properties.

1.3 Contents of the thesis

A brief outline of the content of this thesis is as follows. Chapter 2 deals with the basic theories of magnetism, fundamentals of the polyol process, and the description characterization techniques that were used. Chapter 3 presents the experimental procedures to synthesize magnetic cobalt as well as a brief description of the different techniques used to characterize the products. Chapter 4 is focused on the analysis and interpretation of the obtained results. Chapter 5 presents the conclusions of this thesis and the bibliography used.

2 THEORETICAL BACKGROUND

2.1 Introduction to magnetism

In general, all materials can be divided into three groups according to their interaction with an external magnetic field: diamagnetic, paramagnetic, and cooperative magnetic; the last definition involves ferromagnetic, antiferromagnetic, and ferrimagnetic materials. The fundamentals of magnetism and the interaction between materials and external magnetic fields will be discussed in the following sections.

2.1.1 Origin of magnetism

In an atom, the electron possesses a spin which is equivalent to the strength of the magnetic field (magnetic moment) of the electron itself. Electrons are arranged in energy states of a successive order, and for each energy state there can only be two electrons of opposite spins as established by Pauli's principle. Magnetic moments can be generated by the orbital motion of the unpaired electron around the nucleus and the spin of the electron about its own axis (Figure 2.1 a).

The magnetic moment of each electron pair in an energy level is opposed and, consequently, whenever an energy level is completely full there is no net magnetic moment. Based on this reasoning, we expect any atom of an element

On the other hand, the interaction of atoms in a magnetic material generally consists of a large number of domains, each one magnetized in a random direction. Thus, in the absence of a field the average net magnetization of the domains is zero (Figure 2.2).

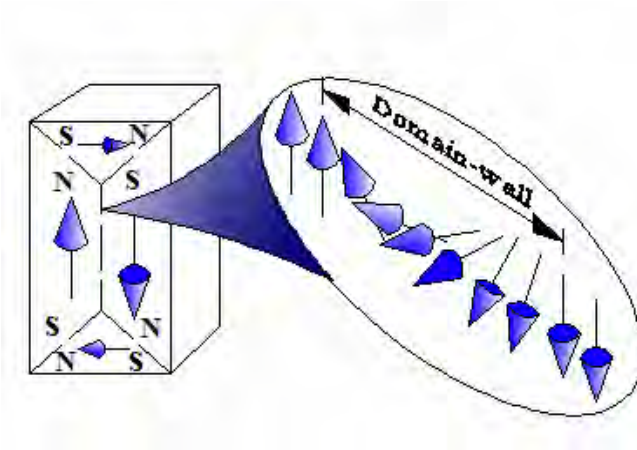


Figure 2.2: Domains and domain-walls in magnetic materials.

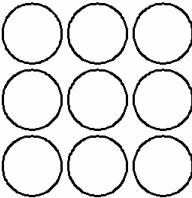
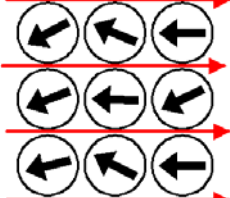
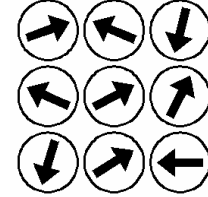
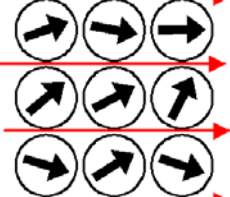
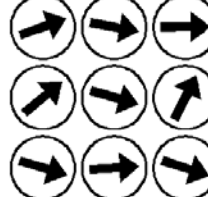
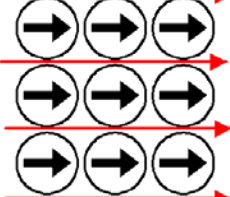
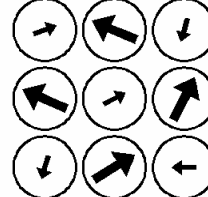
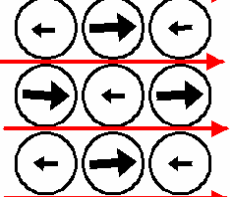
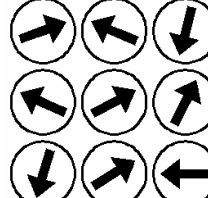
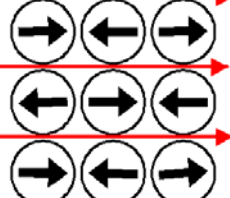
2.1.2 Types of magnetism

The response of the atom to an applied magnetic field depends on how the magnetic dipoles represented by each atom react to the field. In atoms with close shells of electrons, the spin magnetism is self-canceling and the application of a magnetic field has the effect of distorting the electron orbits so that the internal magnetic resultant net remains the same. This effect of realignment of electron orbits is very small and is called **diamagnetism**. If within the atomic shells there are some shells which contain electrons whose spin is not compensated by other electrons of corresponding opposite spin, we can have atoms which carry a

resultant magnetic moment, due to the unpaired or uncompensated spins. These moments tend to align with the applied field but are kept from total alignment by thermal energy. This behavior is referred as **paramagnetism**. If the magnetic atoms are in close enough contact with each other so that the magnetic electrons can be exchanged between neighboring magnetic atoms, a cooperative magnetization may occur which spontaneously aligns all atoms in the lattice and binds their moments very strongly. This spontaneous magnetization is characteristic of **ferromagnetic** materials. The spins are aligned parallel by the exchange coupling between atoms. Under some cases, the coupling can cause anti-parallel alignment of neighboring atoms, which is called **antiferromagnetism**. The resultant magnetization is small since the moments of opposite spins cancel each other. Finally, if the two interpenetrating lattices have anti-parallel magnetization of unequal magnitude a resultant magnetization remains in the direction of the stronger magnetic sub-lattice moment. This uncompensated antiferromagnetism is called **ferrimagnetism**. Table 2.2 summarizes the described behavior of materials when a magnetic field is applied. The vector sum of all magnetic moments within a material per unit volume is known as the intensity of magnetization or magnetization M . The response of a material to an applied field H is characterized by a quantity known as the magnetic susceptibility χ , defined as the ratio of M to H :

$$\chi = \frac{M}{H} \qquad \text{Equation 2.1}$$

TABLE 2.2: Representation of the orientation of magnetic moment vector (\blackleftarrow) in a domain (\bigcirc) for different types of magnetic behavior of the materials when external magnetic field (\longrightarrow) is applied.

Magnetic behavior	No applied magnetic field	Applied magnetic field	Example
Diamagnetic			Inert gas, Hg, P, S, Al ₂ O ₃ , Cu, Au, Si, Ag, Zn, salts.
Paramagnetic			Pt, Al, Cr, Mn, Mo, Na, Ti, Zr, NO.
Ferromagnetic			Co, Fe, Ni, Fe ₃ O ₄ , NiFe ₂ O ₄
Ferrimagnetic			Ni, Fe ₃ O ₄ , Gd
Antiferromagnetic			CoO, MnS, MnO, NiO, Mn

Diamagnetic materials have negative susceptibility values that are in the range between -10^{-6} and -10^{-5} [1]. Paramagnetic and antiferromagnetic materials show

small positive susceptibility in the order of 10^{-3} to 10^{-5} . On the other hand, ferromagnetic and ferrimagnetic materials show a large positive susceptibility $> 10^{-3}$. As a prelude to the discussion of magnetic materials, Table 2.3 provides the conversion factors and units used within this thesis.

TABLE 2.3: Conversion factors and units used in this thesis.

Quantity	Symbol	Gaussian units (emu)	Conversion factor	Sommerfeld units (SI)
Field	H	Oersted	$1000/(4\pi)$	$A \cdot m^{-1}$
Mass Magnetization	M	emu/g	1	$A \cdot m^2 \cdot Kg^{-1}$

2.1.3 Magnetization

Magnetization arises from the contribution of unpaired electron spin in transition metals. Each unpaired electron contributes a single Bohr magneton to the magnetic nature of the metal ($\mu_B = 9.27 \times 10^{-24}$ ampere·m²). The spontaneous magnetization at 0 K is given by the number of uncompensated Bohr magnetons. The magnetization decreases with increasing temperature and finally becomes zero at the so-called Curie temperature, T_C , because of thermal disturbance of the parallel alignment of the spins.

The magnetization of magnetic particles can be expressed as magnetic moment, emu, per unit volume or per unit mass. The approach to saturation as a function of

field is shown in Figure 2.3. In the low field, region I, a number of factors act against complete saturation, e. g. strains, impurities, and anisotropic effects. In this region magnetization changes occur by domain-wall displacements (Figure 2.3 b). Region II involves higher fields than region I. Although most of the limiting interactions would be overcome, anisotropic contributions and spin excitations may still be present. In region II the total magnetization varies only by rotation of the magnetic moments (Figure 2.3 c). In ultra-high fields region III, the interaction between the applied field and the magnetic system may be large enough to produce magnetic saturation (Figure 2.3 d), i.e., the material has reached its magnetic saturation value M_s .

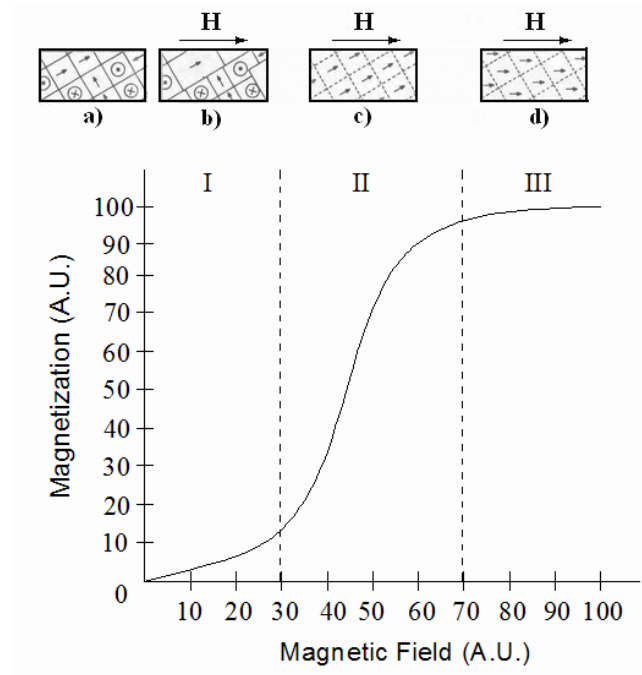


Figure 2.3: Regions in the M-H variation. I: Partial magnetization by domain-wall movement; II: Irreversible rotation of domain magnetization; III: Magnetic saturation. Adapted from reference [2].

2.1.4 Origin of coercivity

As shown in the preceding section, imperfections in the material would act as obstacles to the rotation of the magnetization and domain wall motion when the field is increased. These defects prevent domain-walls from returning to their initial position when the field is removed. The magnetic field required to cause the return of magnetic moment vectors to the initial conditions is defined as coercivity, H_c . For small crystals, domain wall motion does not control the coercivity; instead, magneto-crystalline anisotropies are the main factors that contribute to the coercivity. It has been reported that coercivity is strongly dependent on particle size [3]. Figure 2.4, shows schematically the variation of coercivity in relation to particle size. As the grain size decreases, a critical size will be reached where the grain can no longer accommodate a domain-wall. Below this critical size, the grain contains a single domain (SD). For smaller grain sizes, coercivity again decreases, but this time due to the randomizing effects of thermal energy. The maximum coercivity for a given material occurs within its SD range, the dashed zone in the Figure 2.4. For larger grain sizes, coercivity decreases as the grain subdivides into domains (MD). To change the magnetization of a MD grain, first translate the domain wall, a energetically easy process, which can be accomplished in relatively low fields. Thus MD grains are magnetically soft with low values of coercivity and remanence magnetization. However, the only way to change the magnetization of a SD grain is to rotate the

magnetization, an energetically difficult process. Thus, SD grains are magnetically hard and have high coercivities and remanence magnetization. As particle size continues to decrease within the SD range, another critical threshold is reached, at which remanence and coercivity go to zero. When this happens, the grain becomes superparamagnetic (SPM), where thermal energies cause the spins to flip between minimum energy and make that this kind of particles has unstable condition. This leads to these materials behaving as paramagnets (upon removal of the applied field, they retain no magnetization). Superparamagnetic materials showed a large positive susceptibility $> 10^{-3}$.

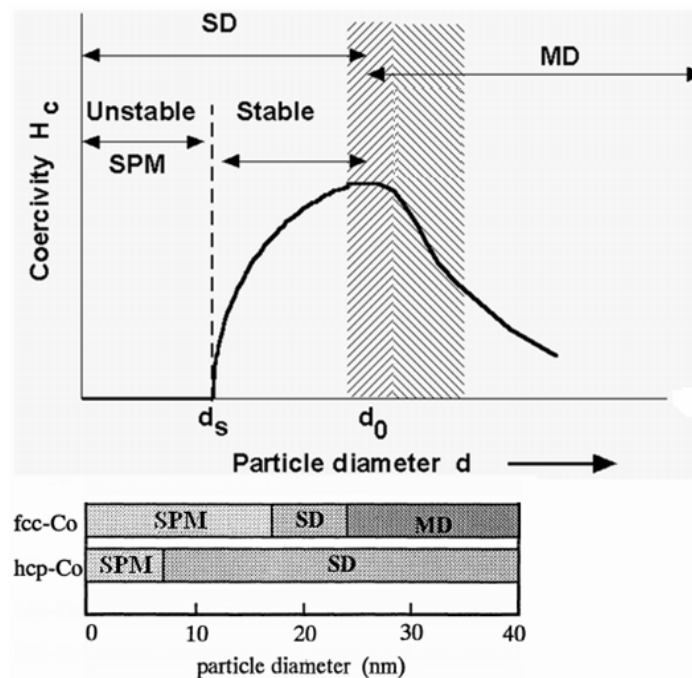


Figure 2.4: Schematic variation of coercivity with particle size. The scale at the bottom shows critical sizes for cobalt. MD: multi-domain region; SD: single domain region and SPM: superparamagnetic region. Adapted from references [4][5].

2.1.5 Magnetic hysteresis loop

When a magnetic field is applied to a ferromagnetic material its magnetization changes from zero to a maximum value, which eventually becomes M_s . Figure 2.5 illustrates the plot obtained during this magnetizing and demagnetizing process, which is known as the hysteresis loop. For the curve OA of the initial magnetization curve, the change in the magnetization of the material is reversible, which means that if the applied field is removed its magnetization will return to its original value. The region between points A, B, and C marks the irreversible region and the magnetization increases rapidly with the applied field.

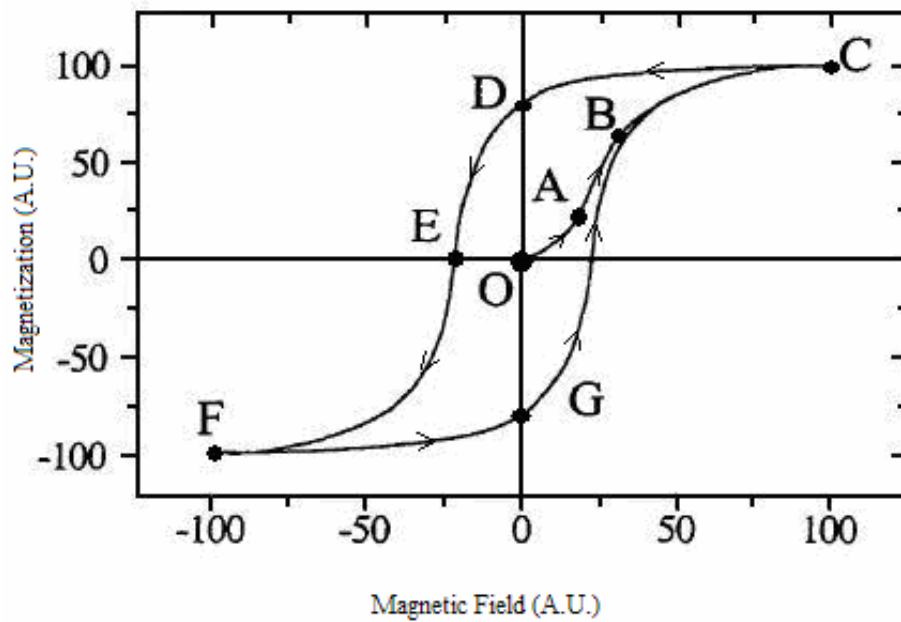
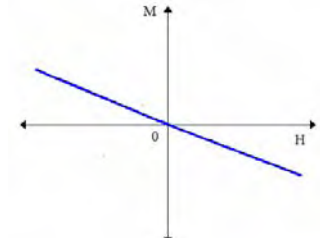
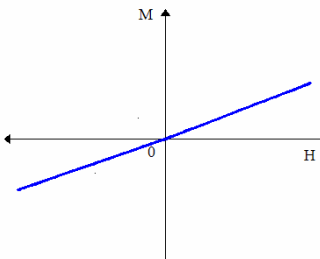
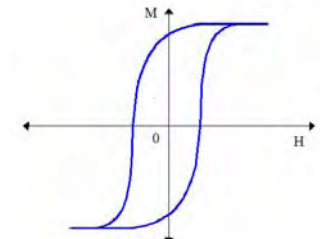
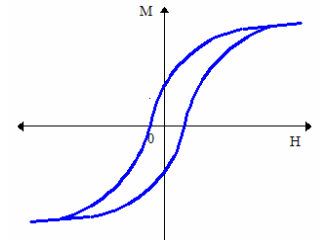
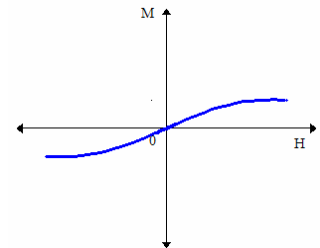


Figure 2.5: Magnetization (M) vs. Applied Field (H) hysteresis loop. Adapted from reference [2].

After point C, all the magnetic moments are aligned towards the direction of the applied field. Beyond this point the magnetization remains almost constant (M_s) and the sample is magnetically saturated. A further small magnetization increase is possible by applying high fields, which changes the population of the spin-up and spin-down electrons. As the applied field decreases from the saturation point, some of the magnetic moments "relax" from their strict parallel alignment, causing the internal magnetization to decrease in strength. When $H = 0$ (point D) the magnetization reaches a finite value known as remanence or remanent magnetization M_r . The value of the negative applied field at which the magnetization becomes zero is known as the coercive field or coercivity H_c and the sample is said to be magnetically demagnetized. One of the most important applications for magnetic materials is data storage. The basic goal of magnetic storage is the semi-permanent recording of information for the purpose of accessing it at a later time. The recording must be semi-permanent to allow for the removal of stored data or its replacement with new. This requires materials with high magnetic coercivity, which is a measure of the material's ability to resist erasure (ferromagnetic behavior). In addition, a high remanence M_r is required so that the recorded signal is large enough to be detected.

TABLE 2.4: Characteristic hysteresis loop for different types of magnetic behavior.

Magnetic behavior	Characteristic magnetic hysteresis loop
Diamagnetic	
Paramagnetic	
Ferromagnetic	
Ferrimagnetic	
Antiferromagnetic	

2.1.6 Magnetic anisotropy

When a physical property of a material is a function of direction, that property is said to exhibit anisotropy. The magnetization in ferromagnetic materials is in general anisotropic. When an applied field tries to reorient the spin of an electron, its orbit poses a resistance since the orientation of the electron orbit is strongly fixed to the crystal lattice. The demagnetized state of a crystal in which the spins, or spontaneous magnetization, lie along the easiest direction corresponds to a minimum in energy. The magnetocrystalline anisotropy energy is the energy required to break the spin-orbit coupling in order to magnetize a material by reorienting its spin direction, is equal to the product of K_u (uniaxial anisotropy energy per unit of volume) by V (Volume of the particle) [6]. The physical cause of magnetocrystalline anisotropy is attributed to spin-orbit coupling. Due to magnetocrystalline anisotropy, the magnetization tends to lie along certain preferred crystallographic directions, which are known as easy directions or easy axes. These are the directions of the spontaneous domain magnetization of a crystalline material in the demagnetized state, for example $\langle 100 \rangle$ for bcc, $\langle 111 \rangle$ for fcc, or $\langle 0001 \rangle$ for hcp structure. Magnetic anisotropy can have its origin in the shape, crystal symmetry, stress, or directed atomic pair ordering. Of these, only crystal anisotropy is intrinsic to the material. All others are extrinsic or “induced”. Generally, the magnetic anisotropy energy term has the same

symmetry as the crystal structure of the material, and we call it magnetocrystalline anisotropy.

2.2 Cobalt and Cobalt-Platinum alloys

2.2.1 Magnetic materials for data storage applications

Based on the above discussion, it is clear why high K_u materials are very attractive for ultrahigh density magnetic recording applications; they allow smaller, thermally stable media grains. Based on the information given in Table 2.5, prominent candidates are tetragonal inter-metallic compounds (face centered tetragonal phases FePt, CoPt...), which have 20 - 40 times higher K_u , than today's hexagonal Co-alloy based media. High anisotropy materials have high coercivity because more energy is needed ($K_u \cdot V$) for disorienting the magnetic moment vectors to make M_r equal to zero (Table 2.5). This allows for about 3 times smaller grain diameters, because this kind of materials with high K_u values remain stable with respect to thermal energy, and projected 40-100 Gbits/in² mark because with smaller particles with similar or superior magnetic properties than the actual used materials for data storage, increases the areal density, i.e., the number of bits that can be stored in a unit of area of a hard disk [7].

TABLE 2.5: Alloy systems for data storage [7].

Alloy System	Material	K_u (10^7 erg/cm 3)	M_s (emu/cm 3)	D_p (nm)
Co – alloys	CoPtCr	0.20	298	10.4
	Co	0.45	1400	8.0
	Co $_3$ Pt	2.00	1100	4.8
fcc structure	FePd	1.80	1100	5.0
	FePt	6.6 – 10	1140	3.3 – 2.8
	CoPt	4.90	800	3.6
	MnAl	1.70	560	5.1
Rare-earth	Fe $_{14}$ Nd $_2$ B	4.60	1270	3.7
Transition metals	SmCo $_5$	11 – 20	910	2.7 – 2.2

K_u : Uniaxial anisotropy energy per unit of volume.

M_s : Saturation magnetization.

D_p : Minimal stable grain size for data storage times of 10 years.

2.2.2 Cobalt and Cobalt Platinum alloys as magnetic materials

Cobalt, which is naturally ferromagnetic with an atomic number of 27, falls between iron and nickel on the periodic table. At temperatures below 690 K, cobalt has a hexagonal close-packed structure (Figure 2.6 a), which is the most stable phase for bulk cobalt at room temperature, the lattice parameters are $a = 2.505 \text{ \AA}$ and $c = 4.06 \text{ \AA}$ [8]. Between 695 K and its melting point of 1768 K, cobalt has a face-centered cubic structure (Figure 2.6 c) with a lattice parameter of $a = 3.5447 \text{ \AA}$ [9].

For small particles, however, the fcc-Co structure appears to be preferred even below room temperature. For nanocrystalline cobalt fcc- and hcp-Co structures can be present. Metastable epsilon cobalt (ϵ -Co) has been identified only under non-equilibrium synthesis conditions. This phase is not observed in the bulk and

exhibits cubic symmetry (Figure 2.6 b) similar to the β -Mn structure (a high temperature phase of manganese). The corresponding lattice parameter has been reported as $a = 6.097 \text{ \AA}$ [10]. The ϵ -Co unit cell contains 20 cobalt atoms (Table 2.6), which are divided into two types: twelve atoms of Type I (Figure 2.6 b: atoms in red) and eight atoms of Type II (Figure 2.6 b: atoms in blue). These two types of atoms differ in their local coordination. Unlike ideal hcp-Co, which has twelve nearest neighbors, ϵ -Co has only three nearest neighbors for Type I and two nearest neighbors for Type II atoms. This results in a structure for ϵ -Co that is less dense than both the hcp and fcc structures. The calculated density of ϵ -Co is $8.635 \text{ g}\cdot\text{cm}^{-3}$, compared to $8.788 \text{ g}\cdot\text{cm}^{-3}$ and $8.836 \text{ g}\cdot\text{cm}^{-3}$ for the fcc and hcp structures, respectively.

The ϵ -Co phase appears to be metastable under normal conditions for least several months. Heating ϵ -Co at 573 K in vacuum converts it into the hcp-Co structure [11], with the fcc structure is obtained when heated to 773 K [10]. Subsequent cooling does not reproduce the original ϵ -Co structure.

As a summary, Figure 2.7 shows the temperatures for allotropic transformation for nanocrystalline cobalt.

There is a strong correlation between crystal structure and the magnetic properties of cobalt. The anisotropic high-coercivity hcp-Co phase is the preferred structure for permanent magnet applications (recording media, etc), while the more symmetric low coercivity fcc phase is useful for soft magnetic applications. Epsilon cobalt may display magnetic properties different from the two previously

known structures, and this could be scientifically interesting and technologically useful.

As a reference, the magnetic properties of bulk (hcp-fcc) cobalt are presented in Table 2.7.

TABLE 2.6: Atomic coordinates in the unit cell of ϵ -Co structure.

Atom	X	Y	Z	
TYPE I	1	v	v	v
	2	$\frac{1}{2}+v$	$\frac{1}{2}-v$	1-v
	3	1-v	$\frac{1}{2}+v$	$\frac{1}{2}-v$
	4	$\frac{1}{2}-v$	1-v	$\frac{1}{2}+v$
	5	$\frac{3}{4}-v$	$\frac{3}{4}-v$	$\frac{3}{4}-v$
	6	$\frac{1}{4}+v$	$\frac{1}{4}-v$	$\frac{3}{4}+v$
	7	$\frac{1}{4}-v$	$\frac{3}{4}+v$	$\frac{1}{4}+v$
	8	$\frac{3}{4}+v$	$\frac{1}{4}+v$	$\frac{1}{4}-v$
TYPE II	9	1-u	$\frac{3}{4}+u$	$\frac{3}{8}$
	10	$\frac{1}{2}-u$	$\frac{3}{4}-u$	$\frac{5}{8}$
	11	u	$\frac{1}{4}+u$	$\frac{1}{8}$
	12	$\frac{1}{2}+u$	$\frac{1}{4}-u$	$\frac{7}{8}$
	13	$\frac{3}{8}$	1-u	$\frac{3}{4}+u$
	14	$\frac{5}{8}$	$\frac{1}{2}-u$	$\frac{3}{4}-u$
	15	$\frac{1}{8}$	u	$\frac{1}{4}+u$
	16	$\frac{7}{8}$	$\frac{1}{2}+u$	$\frac{1}{4}-u$
	17	$\frac{3}{4}+u$	$\frac{3}{8}$	1-u
	18	$\frac{3}{4}-u$	$\frac{5}{8}$	$\frac{1}{2}-u$
	19	$\frac{1}{4}+u$	$\frac{1}{8}$	U
	20	$\frac{1}{4}-u$	$\frac{7}{8}$	$\frac{1}{4}+u$

TABLE 2.7: Magnetic properties of bulk (hcp-fcc) cobalt.

Coercive force, Oe	8.9
Saturation magnetization, T	1.87
Curie temperature, K	1394

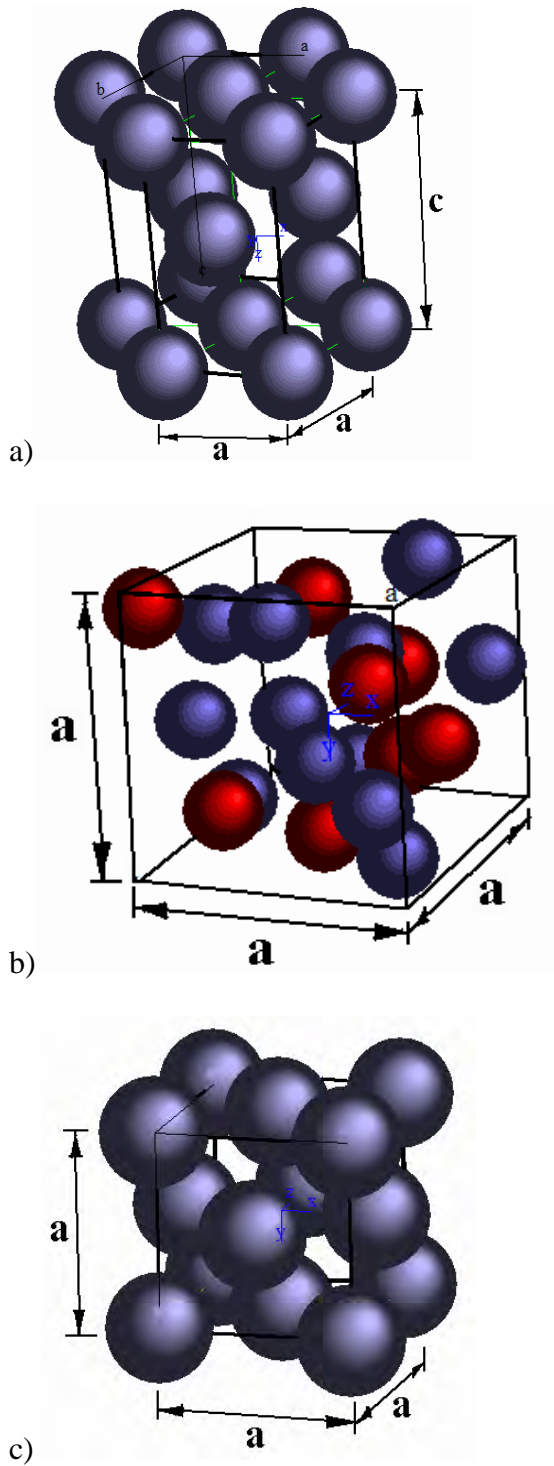


Figure 2.6: Cobalt structures: (a) fcc structure, (b) ϵ -Co structure, cubic cell filled with eight atoms of Type I (red) and twelve atoms of Type II (blue), and (c) hcp structure..

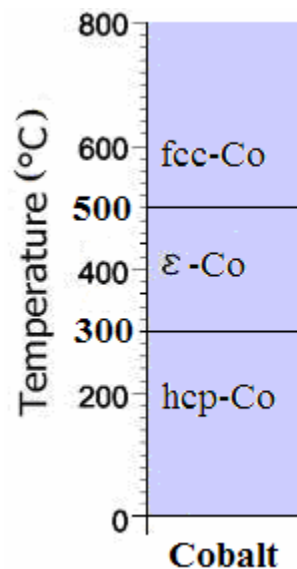


Figure 2.7: Allotropic transformation of nanocrystalline cobalt [12].

Platinum, which is naturally paramagnetic with a bulk magnetic susceptibility of 2.8×10^{-4} , and atomic number of 78, has exceptional resistance to oxidation. Upon heating in air at all temperatures to the melting point (2042 K), it remains untarnished. Platinum has a face-centered cubic structure with a lattice parameter of $a = 0.39231$ nm at 298 K [13].

Cobalt and Platinum can form a family of substitutional alloys due to the similarity of their structures (fcc-Co and fcc-Pt), difference in atomic radius of less than 15 % (Co = 1.67 Å; Pt = 1.83 Å), and small difference in electronegativity (Co = 1.7; Pt = 1.5). The reported magnetic properties of equiatomic CoPt vary widely, presumably due to the difference in the synthesis approach. In particular, reported coercivity values range from about 3 kOe in bulk samples to nearly 30 KOe in thin films. Table 2.8 lists some of the reported values

for coercivity in CoPt. In bulk form, the reported value for saturation magnetization (M_s) is 800 emu/cm^3 [14].

TABLE 2.8: Reported values of coercivity in equiatomic CoPt.

Coercive force (KOe)	Sample type	Reference
> 2.0	45 nm Thin film	Aboaf [15]
5.0	Bulk	Martin [16]
7.0	Single Crystal	Shur [17]
30.0	10 nm thin film	Liou [18]

The essential condition for a solid solution of a suitable composition to become ordered is that dissimilar atoms must attract each other more than similar atoms in order to obtain lower free energy. Under this premise, CoPt_3 should be formed when a high amount of Pt ions is present in the solid solution.

2.2.3 Crystallography of Cobalt Platinum ordered phase

Simple superlattices in cubic binary alloys of the type AB and AB_3 can be formed. Equiatomic CoPt can exhibit fct and fcc structures. Figure 2.8 shows the unit cells for equiatomic ordered fct-CoPt (Figure 2.8 a). Platinum atoms locate at the corners and one base center of the tetragonal unit cell, whereas cobalt atoms are located in the other two face centers of the same tetragonal cell. The lattice parameter 'c' is usually smaller than 'a'. For CoPt_3 type (Figure 2.8 b), Pt atoms locate in all the corners and Co in all the face centers of the unit cube. Outside of the ordered phase regions CoPt has the disordered fcc structure with lattice

parameter $a = 3.772 \text{ \AA}$ [19]. The ordered fct phase has a slight tetragonality with $a = 3.803 \text{ \AA}$ and $c = 3.701 \text{ \AA}$ [20], giving a c/a ratio of 0.973.

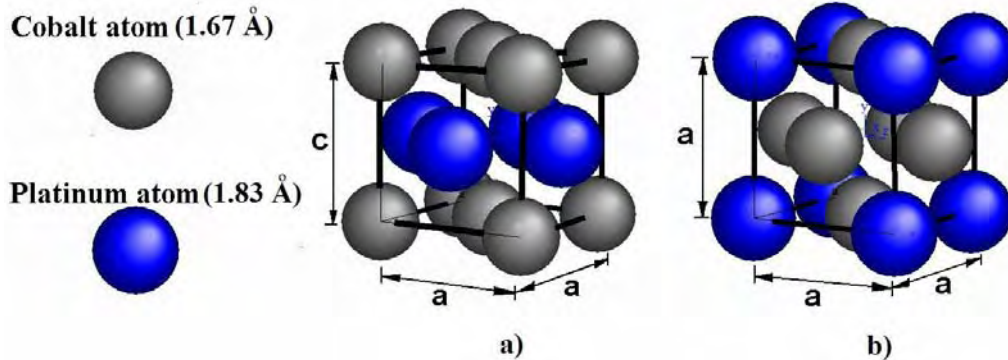


Figure 2.8: Unit cells of a) fct-CoPt type, and b) fcc-CoPt₃ type superstructures.

2.2.4 CoPt phase stability diagram

Simple superlattices in cubic binary alloys of the type AB and AB₃ can be formed. Equiatomic CoPt can exhibit fct and fcc structures. Figure 2.8 shows the unit cells for equiatomic ordered fct-CoPt (Figure 2.8 a). Platinum atoms locate at the corners and one base center of the tetragonal unit cell, whereas cobalt atoms are located in the other two face centers of the same tetragonal cell. The lattice parameter 'c' is usually smaller than 'a'. For CoPt₃ type (Figure 2.8 b), Pt atoms locate in all the corners and Co in all the face centers of the unit cube. Outside of the ordered phase regions CoPt has the disordered fcc structure with lattice parameter $a = 3.772 \text{ \AA}$ [21]. The ordered fct phase has a slight tetragonality with $a = 3.803 \text{ \AA}$ and $c = 3.701 \text{ \AA}$ [22], giving a c/a ratio of 0.973.

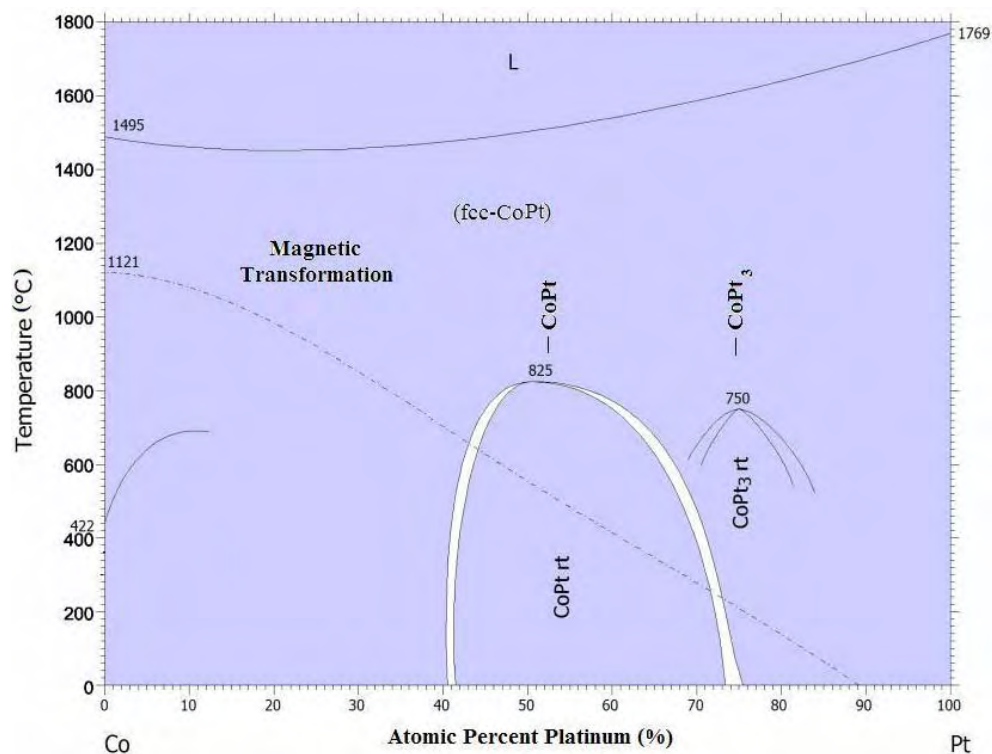


Figure 2.9: Phase diagram of Co-Pt system [12].

2.3 The polyol process

2.3.1 Introduction

The polyol process is based on the use of the reducing capability and de-hydrating characteristic of environmentally benign polyols to form well-crystallized nanoparticles without the problems from oxidation encountered in aqueous media. This process is an easy-to-scale and inexpensive process for preparing thin films and monodisperse metal powders of micrometer and sub micrometer sizes. Various fine metallic powders can be prepared by the reduction of a suitable precursor in liquid polyol. Easily reducible metals such as the noble metals (Ru,

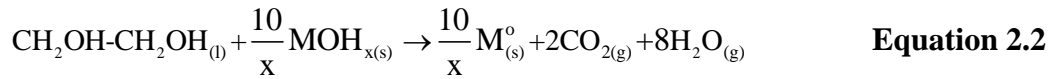
Rh, Pd, Ag, Os, Ir, Pt, Au), even less easily reducible metals (Fe, Co, Ni, Cu, Pb), and polymetallic powders (AgPd, CoNi) can be obtained by precipitation in such organic media (ethylene glycol, propylene glycol, diethylene glycol, triethylene glycol, and tetraethylene glycol, are all members of the polyol family). The ionic solution is stirred and heated up to a given temperature, which can reach the boiling point of the polyol for less reducible metals; conversely, for easily reducible metals (e.g. Pd) the reduction can be carried out at 273 K from a suitable precursor, e.g. Pd(NO₃)₂. The polyol acts simultaneously as the solvent, the reducing agent, and the crystal growth medium for metal particles.

2.3.2 Structural, physical, and chemical properties of polyols

Liquid polyols are nonaqueous solvents because, like water and monoalcohols, they are hydrogen-bonded liquids with a high value of relative permittivity, and therefore they are able to dissolve to some extent ionic inorganic compounds. Moreover, reactions can be carried out in such solvents under atmospheric pressure at temperatures as high as 523 K, i.e., at temperature ranges far above the boiling points of water or monoalcohols such as methanol or ethanol. Polyols are considered mild reducing agents that are able to reduce to the zero-valence state ions of the noble metals, copper, and some more electropositive metals such as cobalt and nickel. Table 2.9 shows some of the properties of various commercially available polyols.

2.3.3 Thermodynamics of the polyol process

Despite the known application of organic polyols as a reducing agent for metal ions in solution, there is a lack of thermodynamic information regarding the equilibrium conditions at the completion of the process. The only available reference that discusses the thermodynamics of the polyol reduction process is by Larcher et al. [22]. There, the thermodynamic approach considers the preparation of metallic powders from oxide and hydroxide precursors in boiling polyols. The same authors assume that the reduction of the precursor into metal comes with a total oxidation of ethylene glycol (EG) into CO₂ and H₂O; this situation would correspond to the maximum reducing power of the polyols. On this basis, the overall reduction reaction of metal hydroxides in boiling EG can be written as:



The Gibbs free energies of formation, ΔG_f , of CO_{2(g)}, M(OH)_{x(s)}, H₂O_(l), and EG_(l) at 473 K can be found from the data in references [23,24]. The ΔG_f for M⁰ is taken to be zero at any temperature.

$$\Delta G_{\text{red}} = 2\Delta G_f(\text{CO}_2) + 8\Delta G_f(\text{H}_2\text{O}) - \frac{10}{x}\Delta G_f(\text{M(OH)}_x) + \Delta G_f(\text{EG}) \quad \text{Equation 2.3}$$

where ΔG_{red} is the variation in the Gibb's free energy for the reduction reaction.

The formation of the metal generally comes with the formation of intermediate reactive phases, such as reduced oxides and/or alkoxides. For example, the formation of Cu from CuO is known to be a multi-step reaction involving the

formation of Cu_2O and Cu-based alkoxide intermediates [25]. The formation of solid intermediates along the path of the reaction will not affect the calculation of ΔG_{red} for the overall reaction since this calculation considers the initial and final states only.

Results of the computation of ΔG_{red} for hydroxides precursors are shown in Figure 2.12. The vertical bars indicate the ranges of the ΔG_{red} values, taking into account the discrepancies in thermodynamic values listed in the literature for the various ΔG_{f} values. The shadowed labels correspond to hydroxides that have not been successfully reduced to metal in EG at boiling point. From this graph, it can be clearly observed that none of the hydroxides with $\Delta G_{\text{red}} > 0$ is reducible. In contrast, all the hydroxides experimentally reduced to metal (not shadowed in Figure 2.10) showed a negative ΔG_{red} .

Based on the above thermodynamic discussion, the formation of metallic cobalt under alkaline conditions will consist of two stages (Figure 2.11). First, a solid intermediate should be formed, probably a metal alkoxide, followed by their dissolution and final reduction by the polyol at higher temperatures. Therefore, any attempt to accelerate the formation of the intermediate products as well as its dissolution would promote the final formation of the metallic phase. Our experimental work has been designed taking in to account these thermodynamic considerations.

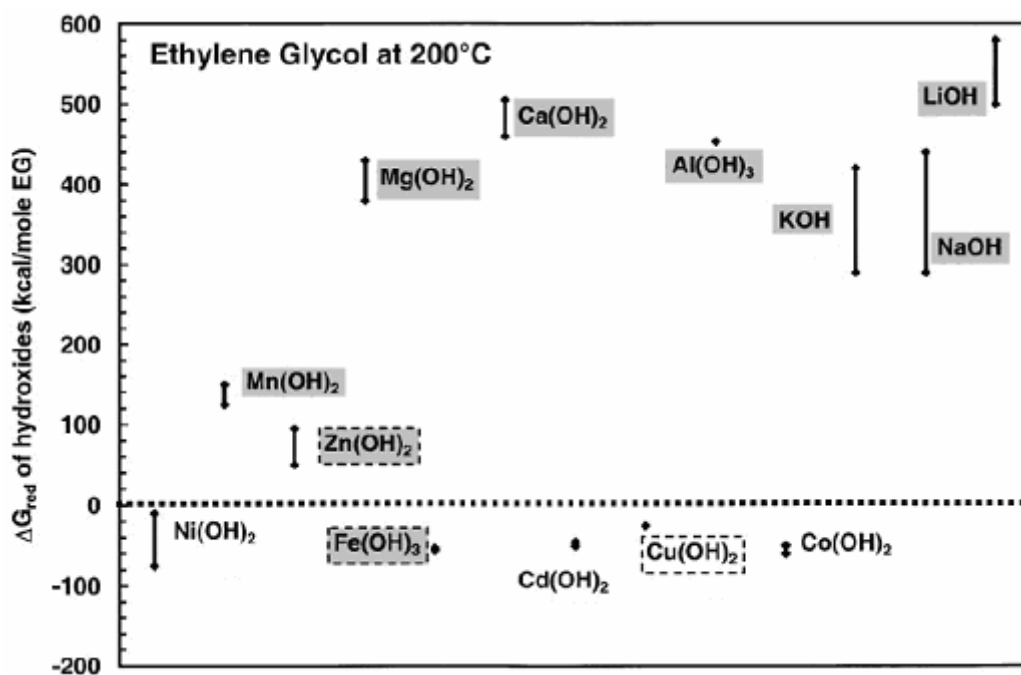


Figure 2.10: Calculated ΔG of reduction (ΔG_{red}) in ethylene glycol at 473 K for various hydroxides assuming a total oxidation of the alcohol and the formation of the metal according to reaction [26]. The shadowed and no shadowed labels indicate experimentally nonreduced and reduced hydroxides, respectively. Dashed frames indicate unstable hydroxides [10].

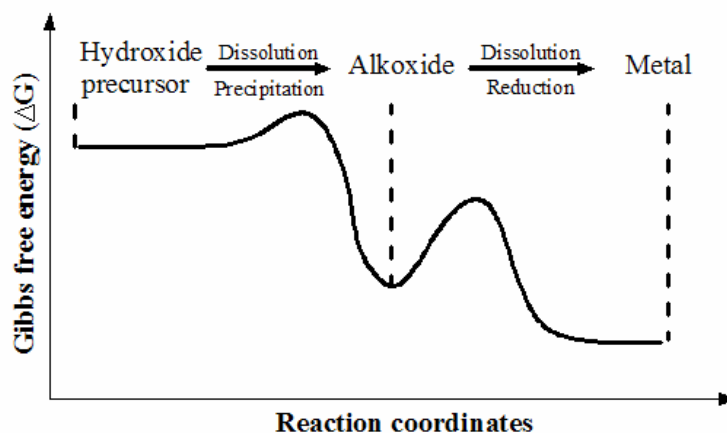


Figure 2.11: Reaction steps and intermediate phases observable during the reaction of various oxides in EG. Adapted from reference [10].

2.3.4 General mechanism of the reduction reaction in polyols

In the polyol process, the metal particles are formed by a reaction involving the following steps: 1) dissolution of the precursor, 2) reduction of dissolved metallic species by the polyol, and 3) homogeneous nucleation and growth of the metal particles in solution. The polyol at first acts as a solvent for the starting compound. Subsequently, the polyol reduces the metal species in the liquid phase, in which nucleation and growth of the metallic phase will take place. In some cases (Co, Ni, Fe), the polyol itself, acting as a protective agent, prevents the coalescence and oxidation of the metal particles [21, 27].

In the reduction of some metals, the reaction mechanism is more complex due to the formation of intermediate solid phases between the starting precursor and the metal powder. Accordingly, one may consider the formation of metallic cobalt from starting hydroxide solutions to proceed in two steps, as described in Table 2.10.

In the case of ethylene glycol the duplicative oxidation of acetaldehyde, previously produced by dehydration of ethylene glycol, should be conducive to the reduction of the metal ions, according to:

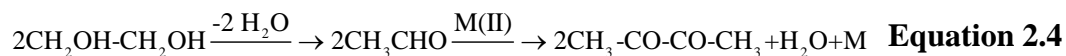


TABLE 2.10: General mechanism of $\text{Co}(\text{OH})_2$ reduction by ethyleneglycol.

<p>FIRST STAGE: Crystallized hydroxide \rightarrow Intermediate Phase</p> <ul style="list-style-type: none">• Progressive dissolution of the starting hydroxide.• Precipitation of the intermediate phase.• Evolution of water by distillation.
<p>SECOND STAGE: Intermediate phase \rightarrow Metal</p> <ul style="list-style-type: none">• Dissolution of the intermediate phase.• Reduction in solution.• Evolution of the volatile products of reaction.• Homogeneous nucleation and growth of metal particles.

Nucleation and Growth Stages in the polyol process.

The mechanisms involved with the formation of metal particles through nucleation and growth from the solution is quite general for all metals obtained by the polyol process (noble metals, Fe, Cu, Co, Ni). It is well known that the precipitation of a solid from a solution proceeds in two steps: nucleation and growth. During nucleation, solid tiny particles form from the supersaturated solution. If these nuclei appear spontaneously, without the promoting effect of impurities, the nucleation is called homogeneous. During the second step, the original nuclei will grow into larger particles. In order to obtain monodisperse particles, a general condition must be fulfilled: nucleation and growth must be two completely separate steps. This condition has been expressed in the LaMer

diagram (Figure 2.12) which describes the formation of monodisperse metals such as Co (II) and Ni (II). The concentration of metallic species in solution increases and reaches the saturation concentration, which is unknown but probably very small. As the reduction reaction proceeds, the solute content further increases until critical supersaturation is reached, leading to rapid, spontaneous nucleation. Many nuclei are formed during a short time and, therefore, the metal concentration is quickly lowered below critical. Particle growth occurs from the original nuclei, as long as the metal is slowly provided by the reduction, eventually yielding solids of equal size. In order to actually obtain such uniform particles, it is also necessary to prevent their coagulation during the growth stage.

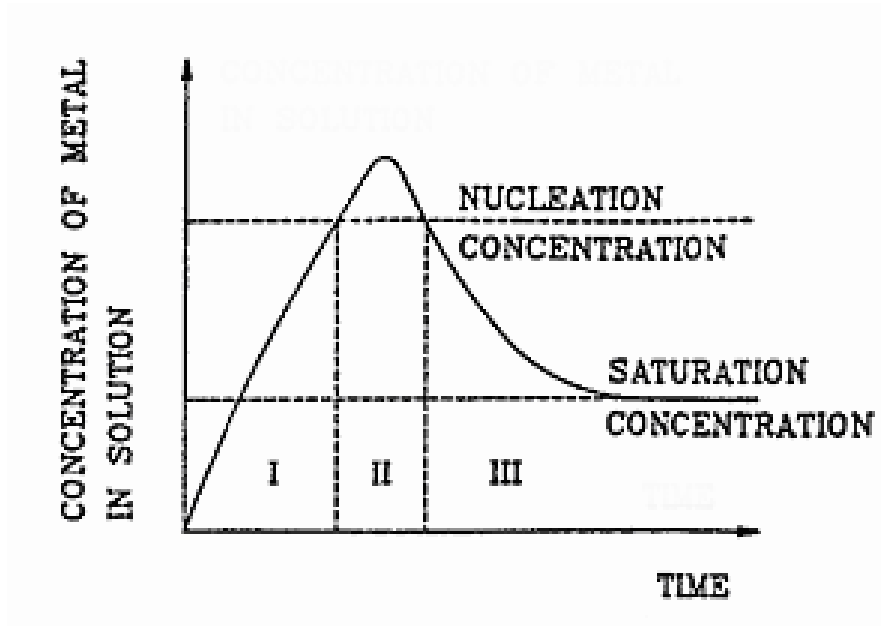


Figure 2.12: LaMer's model for the formation of a monodisperse system: I-precursor formation step; II-nucleation step; III-growth step [28].

2.3.5 Related Works of Cobalt and Cobalt Platinum in Polyols

In order to reduce cobalt to the zero-valence state, Fiévet et al. [21], used cobalt acetate hydrate as the source of cobalt ions. The reduction to a metal can be achieved in ethylene glycol, diethylene glycol, or a mixture of both. In all the syntheses they obtained microcrystalline cobalt particles with homogeneous size (1.75 μm) with mixed hcp and fcc structures [29]. Nassira Chakroune et al. [30], using 1,2 propanediol synthesized Co particles at 423 K for 1 hour, obtained fcc and hcp structures, particles of 100 nm of average diameter with coercivities and remanence /saturation ratios in the ranges of 600-900 Oe and 0.25-0.33, respectively. Regarding the applicability of the polyol process to synthesize metallic nanostructures, Chinnasamy et al. (2003), reported the synthesis and magnetic properties of CoPt nanoparticles. XRD and TEM studies showed that the as-synthesized CoPt nanoparticles had FCC structure and about 5 nm in diameter, respectively. Composition analyses revealed that as-synthesized particles were almost equiatomic $\text{Co}_{50}\text{Pt}_{50}$. Magnetic characterization evidenced the ferromagnetic nature of these nanoparticles at room temperature, which exhibited magnetization and coercivity values as low as 8 emu/g and 380 Oe, respectively. Annealing the CoPt nanoparticles above 550 $^{\circ}\text{C}$ induced ordering and enhanced magnetic properties to values of 3.67 KOe and 7.57 KOe, when the particles were annealed 973 K in H_2/N_2 atmosphere for 60 min [31].

In 2005, Vassilios et al. published a work where CoPt nanoparticles with an average size of 3 nm and narrow distribution were synthesized by chemical reduction of $\text{Co}(\text{CH}_3\text{COO})_2$ and $\text{Pt}(\text{acac})_2$ by polyethyleneglycol-200. The as-prepared nanoparticles exhibited a disordered FCC structure which transformed after thermal treatment at 973 K to an ordered fct structure, with coercivity up to 6 kOe at room temperature (9 kOe at 5K). This was attributed to the high magnetocrystalline anisotropy of the tetragonal structure [32].

2.4 Fundamentals of materials characterization techniques

2.4.1 X-Ray diffractometry

In our work, X-ray diffraction (XRD) was used to determine the crystallographic structure and different phases in the cobalt products. High-angle ($2\theta > 20^\circ$) X-ray diffraction studies are widely used for crystal structure identification and lattice constant determination. X-rays are produced by a beam of fast electrons bombarding a metal target in an evacuated tube. The energetic electrons excite the target atoms, which subsequently emit high frequency electromagnetic radiation as they decay back to their ground states. The emitted x-rays are characteristic for the target material and usually consist of a few strong lines. Cu and Mo are the most widely used target metals. The beam is filtered by using a monochromating crystal, which only allows observation of the $K_{\alpha 1}$ and $K_{\alpha 2}$ X-rays with

wavelengths of 1.5405 Å and 1.544 Å. The intensity ratio for the $K_{\alpha 1}$ and $K_{\alpha 2}$ x-rays is approximately 2:1 and the weighted average of the radiation is 1.5418 Å [33]. The angles where the peaks in the x-ray diffraction spectrum occur obey Bragg's law:

$$n\lambda = 2d_{(hkl)} \sin \theta \quad \text{Equation 2.5}$$

where λ is the wavelength of the x-ray beam, $d_{(hkl)}$ is the spacing between the (hkl) crystallographic plane contributing to the diffraction peak, θ is the angle between the incident beam and the (hkl) crystallographic plane, and 'n' is an integer (Figure 2.13). In an X-ray diffraction study a range of θ is scanned in order to find the Bragg reflection angles and consequently determine the lattice spacing.

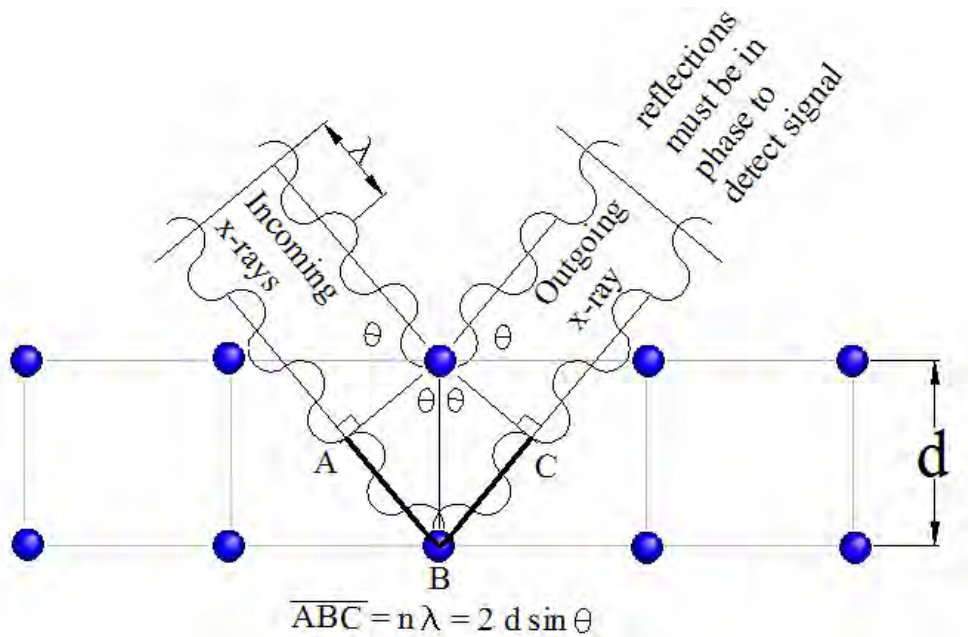


Figure 2.13: Schematic representation of the X-ray diffraction, the incoming x-rays (red) diffract with θ angle (blue) in the lattice of the material and only the waves in face can be detected.

Estimation of average crystallite size. Scherrer equation

Scherrer equation is a very useful tool to estimate the average crystallite size in submicrometric solids. Multiplying both sides of the Bragg's equation by an integer 'm' such that $m \cdot d = t$, the thickness of the crystal, leads to:

$$m \cdot \lambda = m \cdot 2 \cdot d_{(hkl)} \cdot \sin \theta \quad \text{Equation 2.6}$$

$$m \cdot \lambda = 2 \cdot t \cdot \sin \theta \quad \text{Equation 2.7}$$

Equation 2.7 can also be interpreted as the m^{th} order reflection from a set of planes with interplanar distance t . Differentiating both sides of equation 2.7, remembering that ' $m \cdot \lambda$ ' is a constant, gives:

$$0 = 2 \cdot \Delta t \cdot \sin \theta + 2 \cdot t \cdot \cos \theta \cdot \Delta \theta \quad \text{Equation 2.8}$$

$\Delta \theta$ can be positive or negative (only absolute values are of interest). Then:

$$t = \frac{\Delta t \cdot \sin \theta}{2 \cdot \cos \theta \cdot \Delta \theta} \quad \text{Equation 2.9}$$

Since the smallest increment in t is d , using $\Delta t = d$, and substituting $\lambda/2$ for $d \cdot \sin \theta$ (from Bragg's law) we get,

$$t = \frac{\frac{\lambda}{2}}{2 \cdot \cos \theta \cdot \Delta \theta} \quad \text{Equation 2.10}$$

Substituting B for $2 \cdot \Delta \theta$, the angular width,

$$t = \frac{\lambda}{B \cdot \cos \theta} \quad \text{Equation 2.11}$$

which is essentially Scherrer's equation. A more sophisticated analysis of the problem only adds a pre-factor of 0.95 to the right hand side of equation 2.11 and leads to the corrected Scherrer's equation:

$$t = \frac{0.95 \cdot \lambda}{B \cdot \cos \theta} \quad \text{Equation 2.12}$$

In this equation, λ represents the wavelength of the X-ray radiation, B is the width of the diffraction peak at half its maximum intensity (in radians), and θ the maximum scattering angle.

Estimation of the lattice parameters

Interplanar spacing equations for cubic (equation 2.13), tetragonal (equation 2.14), and hexagonal (equation 2.15) systems are related to the lattice parameters and crystallographic planes in the sample as follows [33]:

$$\frac{1}{d^2} = \frac{h^2 + k^2 + l^2}{a^2} \quad \text{Equation 2.13}$$

$$\frac{1}{d^2} = \frac{h^2 + k^2}{a^2} + \frac{l^2}{c^2} \quad \text{Equation 2.14}$$

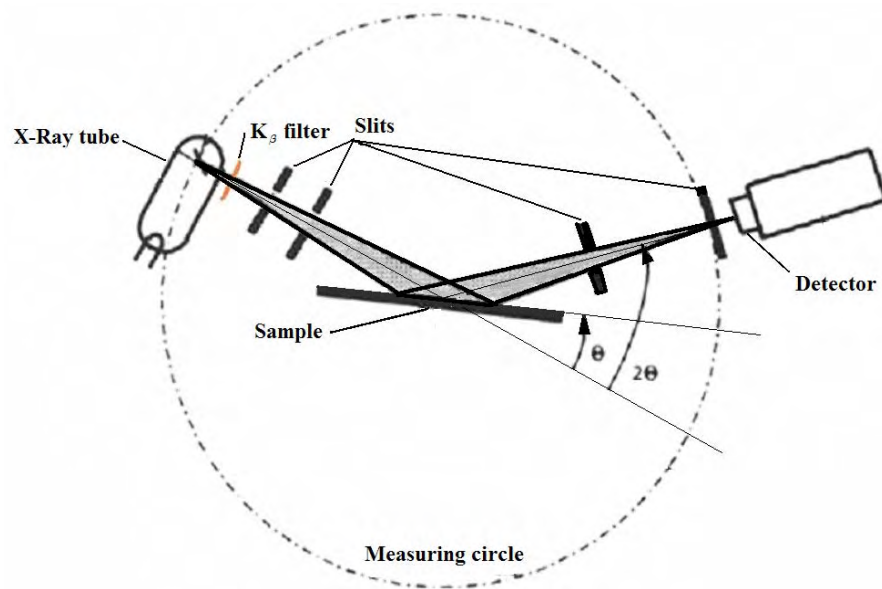
$$\frac{1}{d^2} = \frac{4}{3} \left(\frac{h^2 + hk + k^2}{a^2} \right) + \frac{l^2}{c^2} \quad \text{Equation 2.15}$$

Williamson-Hall analysis can be used to estimate crystallite size and average lattice strain:

$$\beta \cdot \cos(\theta) = 4 \cdot \varepsilon \cdot \sin(\theta) + \frac{\lambda}{t} \quad \text{Equation 2.16}$$

Where β can be approximated as the Full Width at High Maximum in radians [34] of the angle θ , ε is the micro strain, λ is the wave length of the x-Ray, and t is the crystallite size.

a)



b)

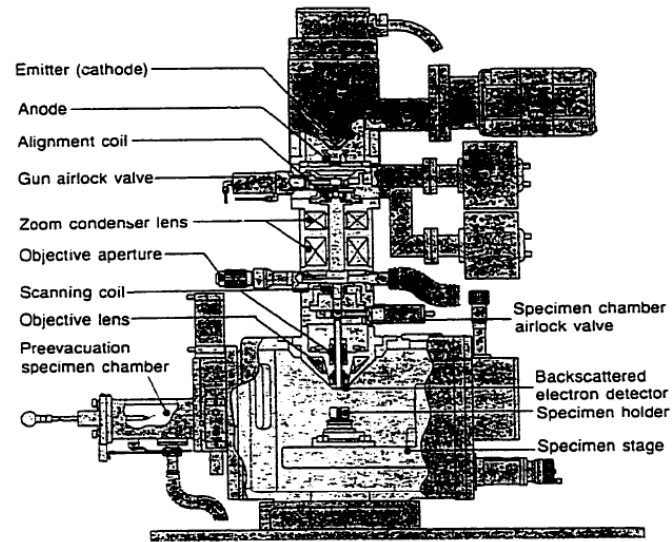


Figure 2.14: (a) Schematic representation of the X-ray diffractometer; (b) Photograph of XRD SIEMENS D5000, available on the materials research laboratory at UPRM.

2.4.2 Scanning Electron Microscopy

Scanning electron microscopy (SEM) was used to obtain information about the size and morphology of the powdered samples. In SEM the lenses do not form an image of the specimen. Instead, the lenses are used to generate a de-magnified, focused spot of electrons that is scanned over the surface of an electrically conductive specimen. As these impinging electrons strike the specimen, they give rise to a variety of signals, including low energy secondary electrons from the uppermost layers of the specimen. Some of the secondary electrons are collected, processed, and eventually translated as a series of pixels (picture elements) on a cathode ray tube or monitor. For each point where the electron beam strikes the specimen and generates secondary electrons, a corresponding pixel is displayed on the viewing monitor. The brightness of the pixel is directly proportional to the number of secondary electrons generated from the specimen surface. Since the electron beam is scanned rapidly over the specimen, the numerous, minute points appear to blend into a continuous image composed of many density levels or shades of gray. The shading is similar to an ordinary black and white photograph in which light and dark tones give the impression of depth. SEM can be used to obtain morphological information with 2 nm resolution.

a)



b)



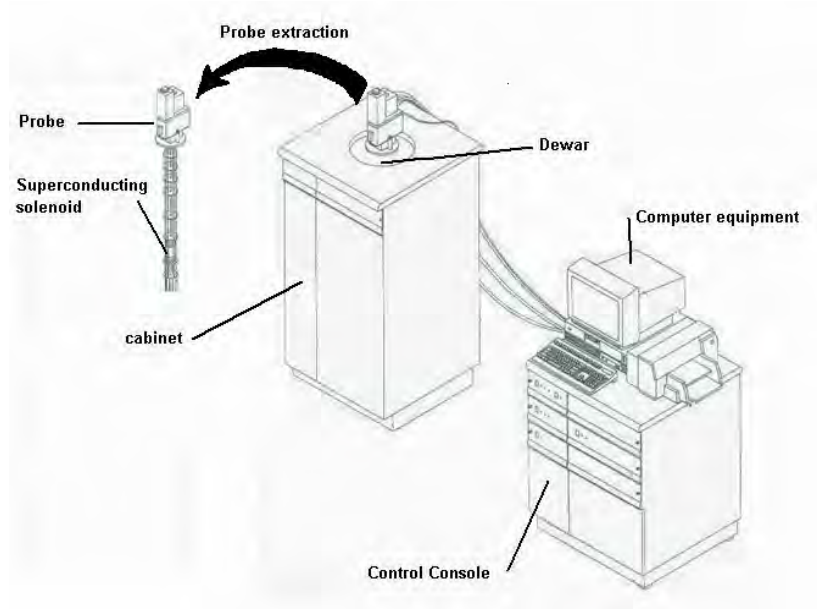
Figure 2.15: (a) Schematic representation of the SEM [34]; (b) Scanning Electron Microscopy (JEOL model JSM-5410 LV available in the Biology microscopy laboratory at UPRM).

2.4.3 *SQUID (Super Quantum Interference Device) Magnetometer*

A Quantum Design XL-7 Magnetic Properties Measurement System (MPMS), with a superconducting quantum interference device (SQUID) detector, provides the ultimate in resolution for magnetic measurements [2]. The SQUID unit can work in the temperature range between 1.9 and 400 K and under a maximum applied field of 7 T. The heart of the MPMS is the superconducting detection coil. The detection coil is located at the midpoint of the superconducting solenoid, which is used to create the applied field. The SQUID sensitivity is usually of the order of 10^{-8} emu with an accuracy of 1%, which is more sensitivity than other magnetometers like Vibrating-sample Magnetometer (VSM), 5×10^{-5} emu. This high sensitive makes the SQUID a perfect choice to measure small magnetic signals.

SQUID measures the magnetic moment by moving the sample through the detection coil. The magnetic moment of the sample creates a flux in the detection coil, which changes with the sample position. The flux is converted to a voltage by the magnetometer and the voltage versus sample position data is further used to extract the magnetic moment. The software package supplied with the MPMS analyzes the voltage versus sample position data and determines a value for the magnetic moment as a result of a fitting procedure between a theoretically expected curve and the experimental data (Figure 2.16).

a)



b)



Figure 2.16: (a) Schematic representation of the SQUID unit; (b) Photograph of Quantum Design MPMSXL available at UPRM.

3 EXPERIMENTAL

3.1 Materials

All chemicals were of chemical grade and used without any further purification. Ethylene Glycol, $\geq 99\%$ was purchased from Aldrich (EG, boiling point 468 K). Triethylene Glycol, $\geq 99\%$ was purchased from Aldrich (TEG, boiling point 551 K). Trimethylene Glycol, 99% (TMEG, boiling point 487 K) was supplied by Alfa Aesar. Tetraethylene Glycol, $\geq 99\%$ was purchased from Aldrich (TREG, boiling point 597 K). As mentioned earlier, the polyols were used as the solvent and reducing agent. Co(II) acetate tetrahydrate 99.995%, $\text{Co}(\text{ac})_2$, and Co(II)-acetylacetonate 97%, $\text{Co}(\text{acac})_2$, salts (Alfa Aesar) were the cobalt precursors. Sodium hydroxide, NaOH, 99.998% (Aldrich) was the source for hydroxyl ions. Hexa-chloroplatinate salt 99.995% (H_2PtCl_6) and Platinum acetylacetonate 99.7%, $\text{Pt}(\text{acac})_2$, both from Aldrich, co-existed in starting solutions when the precipitation of CoPt alloys was attempted. Ethanol, 96% was supplied by Alfa Aesar, and used to wash the precipitated particles.

3.2 Experimental procedure

Polyol solutions of Co and NaOH were placed in a three-neck flask and heated under gentle mechanical stirring ('heating stage'). The amount of NaOH was

determined according to the required $\text{OH}^-/\text{Total Metals}$ mole ratios ('R'). The solution was refluxed for different times under polyol boiling conditions. The time required for the formation of a dark gray, magnetic solid after the reactants reached the selected reaction temperature was defined as the 'reaction time'. The final suspension was quenched in ice and was centrifuged to obtain the powder. The powder was then washed four times with ethanol and finally stored under room temperature conditions. When platinum salts were used, they were added to the cobalt solution from the very beginning. Figure 3.1 shows the experimental set-up used in the polyol synthesis of magnetic precipitates.

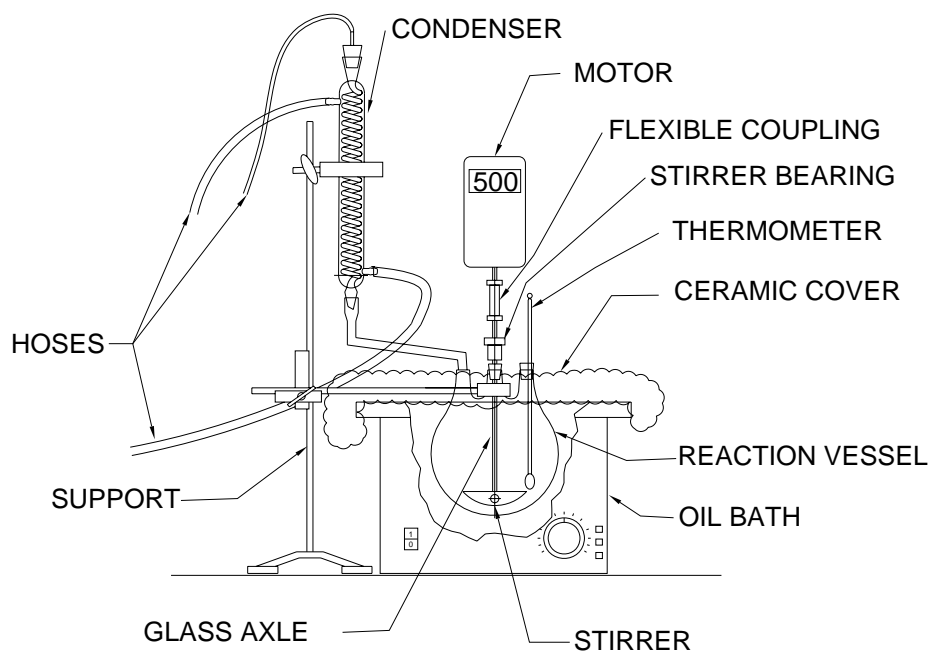


Figure 3.1: Experimental set-up for the synthesis in polyol.

3.3 Characterization techniques

The crystal structure of as-synthesized cobalt nanocrystals was determined by using a SIEMENS D500 X-Ray diffractometer with Cu K α radiation (1.5418 Å). All measurements were carried out at 40 KV and 40 mA and the scanning step and sampling time were 0.02° and 10 seconds, respectively.

Scanning Electron Microscopy (JEOL JSM-5410 LV) was used to determine the morphology and size of the produced particles. The surface of the sample was coated with a thin Au film (2-15 Å) to improve the electron conductivity of the sample, and hence the resolution in the final image. After the vacuum chamber, hosting the sample, was pumped down to 1×10^{-6} torr, the power was turned on at 20KeV. After electron beam centering and focusing, images were obtained at magnifications of 2KX and 20KX.

M-H hysteresis loops were measured at room temperature in a Quantum Design XL-7 MSMP with a SQUID. Samples were placed in a plastic capsule attached to a plastic straw that acted as a holder. The sample holder was then placed in the vacuum chamber. After the chamber was at 300 K, the program was run in DC centering mode.

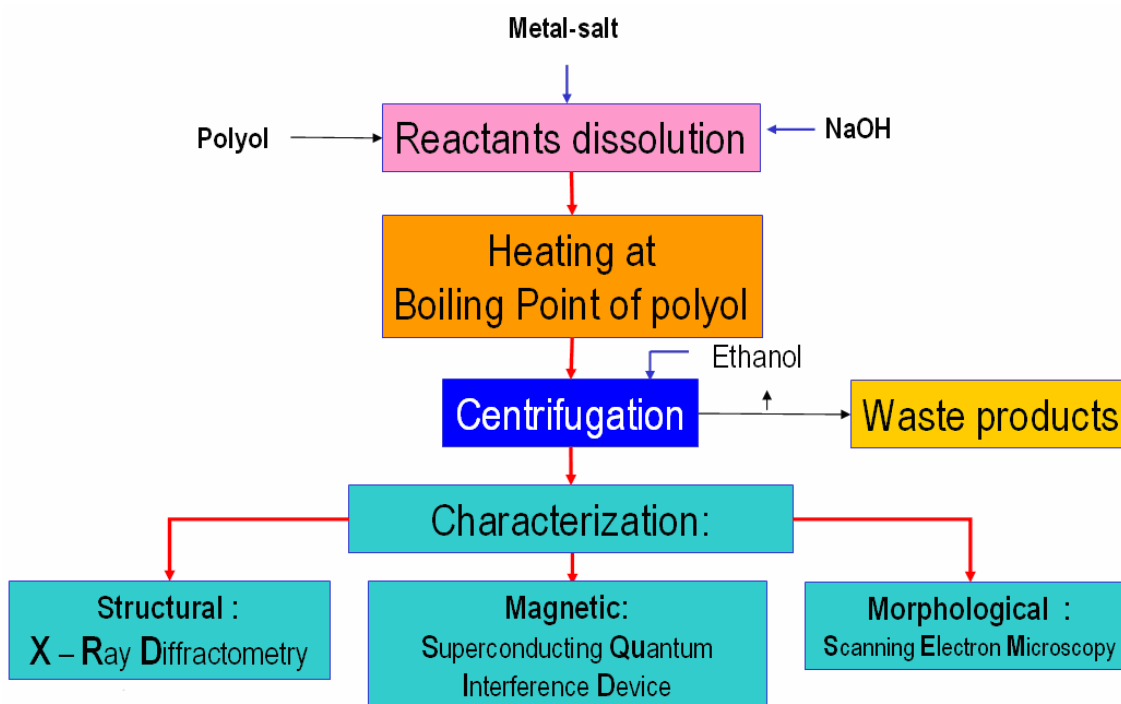


Figure 3.2: Experimental procedure for the synthesis of Co nanoparticles.

4 RESULTS AND DISCUSSION

4.1 Effect of the type of polyol

Ethylene glycol (EG), Triethylene glycol (TEG), Tetra-ethylene glycol (TREG) and Trimethylene glycol (TMEG) were evaluated as reductor media under boiling conditions. It is expected that the higher the boiling point of the polyol, the higher its reduction power. Enhancement in the polyol reduction power could be conducive to the acceleration of the metal forming reaction and hence, to the formation of metastable phases. Available literature suggested that the presence of OH⁻ ions accelerates the formation of metallic cobalt [27], probably due to the enhanced solubility of the intermediate under alkaline conditions. On that basis, we have selected a OH/Co mole ratio of 45 for these experiments.

4.1.1 Structural characterization

Figure 4.1 shows XRD patterns of the samples produced using a 0.01M Co(ac)₂ solution in triethylene glycol (TEG) at 468 ± 5 K and different reaction times. As seen, the conversion of the amorphous intermediate phase (probably metallic hydroxy-alcoxide [29]) into crystalline fcc-Co was strongly dependent on the reaction time. The magnetic product was obtained only after 64 minutes of reaction. Selecting the (111) peak, the average crystallite size was estimated at

12.5 nm and the corresponding lattice parameter was $a = 3.5 \text{ \AA}$, which agrees well with the value for bulk fcc-Co.

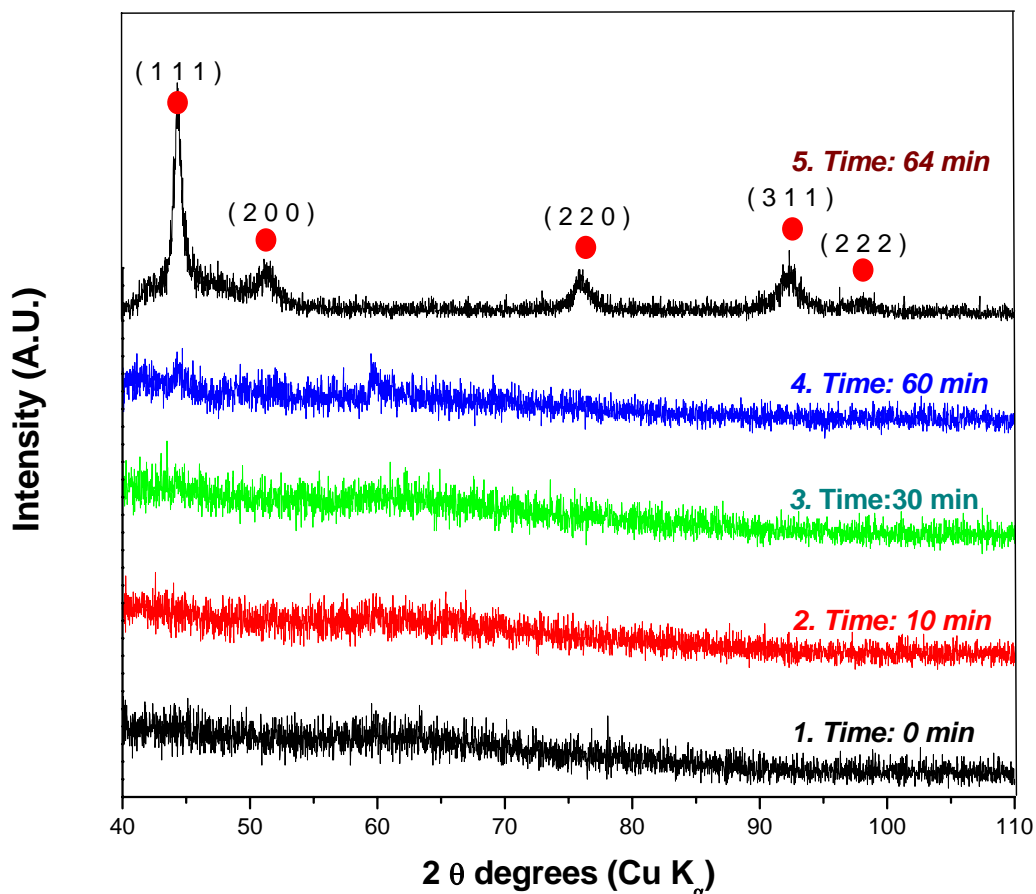


Figure 4.1: XRD patterns of intermediate and cobalt powders synthesized at different reaction times in TEG, from 0.01M Co solution using $\text{Co}(\text{ac})_2$, TEG and ‘R’ = 45. Peaks corresponding to fcc (●) cobalt phase is indicated.

In order to compare the different types of polyols, the synthesis of cobalt was carried out not only in EG but also in TEG, TMEG, and TREG. The reaction time was defined as the time at which the solids exhibited an evident magnetic response in presence of a magnet. Accordingly, the reaction time was 83 minutes

for EG, 64 minutes for TEG and 4 hours for TMEG. No magnetic solid was produced when TREG was used even after 4 hours of reaction. The different times of reaction are explained by the different solubility of the intermediate in each kind of polyol, which would also affect the corresponding reduction and precipitation of cobalt particles. Figure 4.2 summarizes the obtained results. Fcc-Co was the predominant phase when EG was used. Although evident, the presence of hcp-Co was only minor. The lattice parameters for the fcc- and hcp-Co were roughly estimated as $a = 3.5 \text{ \AA}$ for fcc-Co and $a = 2.5 \text{ \AA}$ and $c = 4.0 \text{ \AA}$ for hcp-Co. Both lattice parameters agree with the bulk fcc- ($a = 3.5 \text{ \AA}$) and hcp-Co ($a = 2.5 \text{ \AA}$ and $c = 4.0 \text{ \AA}$) lattice parameters as reported in the PDF # 00-015-0806 and # 00-005-0727, respectively. As shown before, the magnetic solid produced in TEG solutions consisted of exclusively fcc-Co. Taking the (111) peak, the estimated average crystallite size and the lattice parameter were estimated at 13.2 nm and $a = 3.5 \text{ \AA}$, respectively. On the other hand, the solid produced in presence of TMEG was quite different from the ones produced in other evaluated polyols. The solids consisted of a mixture of fcc-, hcp- and metastable ϵ -Co phases. The latter phase is not stable in the bulk and has only been identified in nanocrystalline systems [11]. The noise in the XRD signal, typical of nanocrystalline materials, and the observed overlapping of some of the XRD peaks do not permit a precise estimation of the lattice parameters of the phases detected in this particular sample.

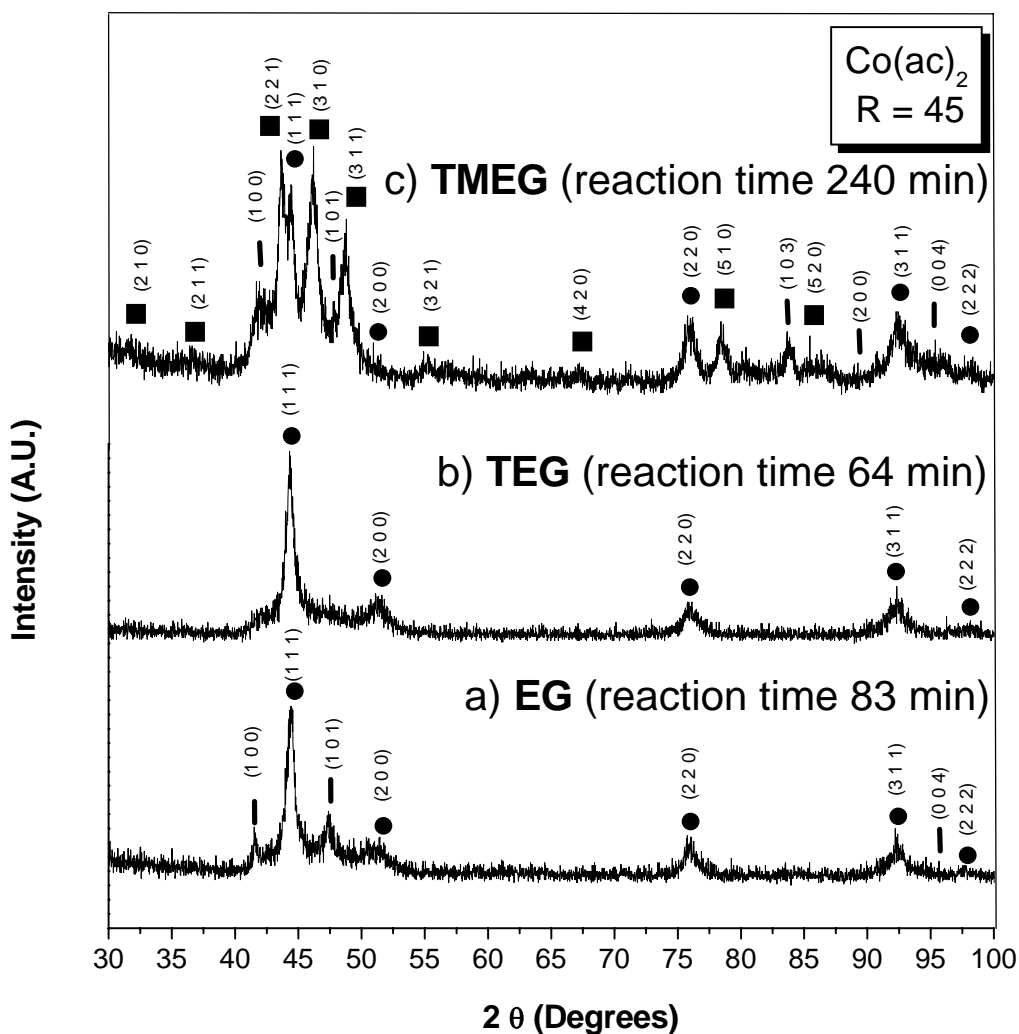


Figure 4.2: XRD patterns of as-synthesized cobalt powders from 0.01M Co solutions using $\text{Co}(\text{ac})_2$ and EG (BP = 468 K), TEG (BP = 551 K) and TMEG (BP = 487 K) at 468 ± 5 K, with ‘R’ = 45 and the suitable reaction time to obtain metallic precipitates. Peaks corresponding to fcc (●), hcp (|) and ϵ (■) cobalt phases are indicated.

4.1.2 Magnetic characterization

The results of the SQUID analyses at 300 K of nanocrystalline cobalt produced in presence of different types of polyol are shown in Figures 4.3-4.5. The synthesis

conditions were the same as described in the previous section. In all the cases the M-H loops were well-saturated. The corresponding saturation magnetization M_s and coercivity H_c values for the solids produced in EG were 263 emu/g and 100 Oe, respectively. The coercivity exhibited by these samples was attributed to the presence of the hcp-Co phase, which was present in a small proportion as shown in Figure 4.2-a. It is well known that metastable fcc-Co phases do not exhibit remarkable ferromagnetism. This expectation was confirmed by the M-H measurements for the solids produced in TEG. The corresponding M_s and H_c values were 115 emu/g and 59 Oe, respectively (Figure 4.5). In turn, the solids produced in TMEG exhibited M_s and H_c values of 107 emu/g and 101 Oe, respectively. Again, the presence of minor amounts of the hcp-Co phase should explain observed magnetic properties.

TABLE 4.1: Reported values of magnetic properties for as synthesized cobalt particles in different polyols using SQUID at 300 K.

Polyol	R	Coercivity (Oe)	Magnetization of remanence (emu/g)	Magnetization of saturation (emu/g)
			Metallic salt $\text{Co}(\text{ac})_2$	
EG	40	100	11.5	263
TEG	40	59	3.4	115
TMEG	45	101	5	107

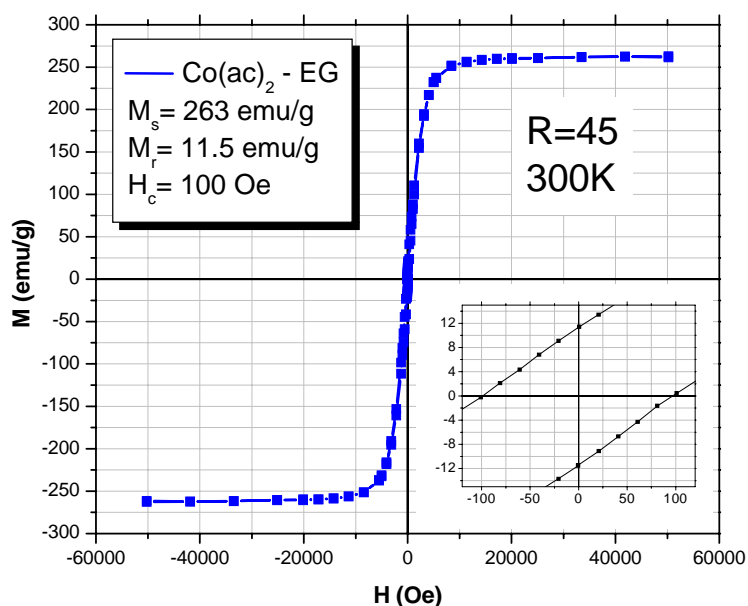


Figure 4.3: M-H loops for Co powders as-synthesized from 0.01M Co solution using $\text{Co}(\text{ac})_2$, EG at 468 ± 5 K, 'R' = 45 and 64 minutes of reaction time. The insert show the M-H loop around the origin.

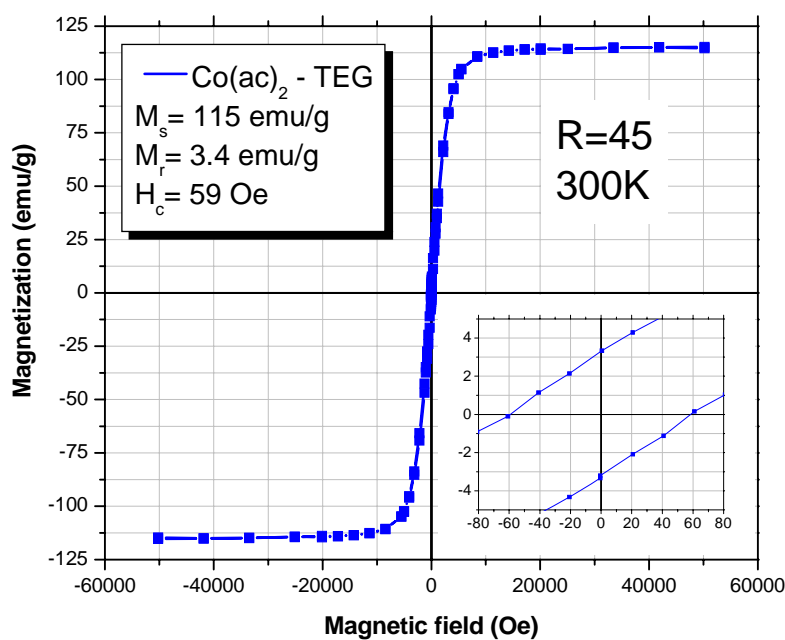


Figure 4.4: M-H loops for Co powders as-synthesized from 0.01M Co solution using $\text{Co}(\text{ac})_2$, TEG at 468 ± 5 K, 'R' = 45 and 83 minutes of reaction time. The insert show the M-H loop around the origin.

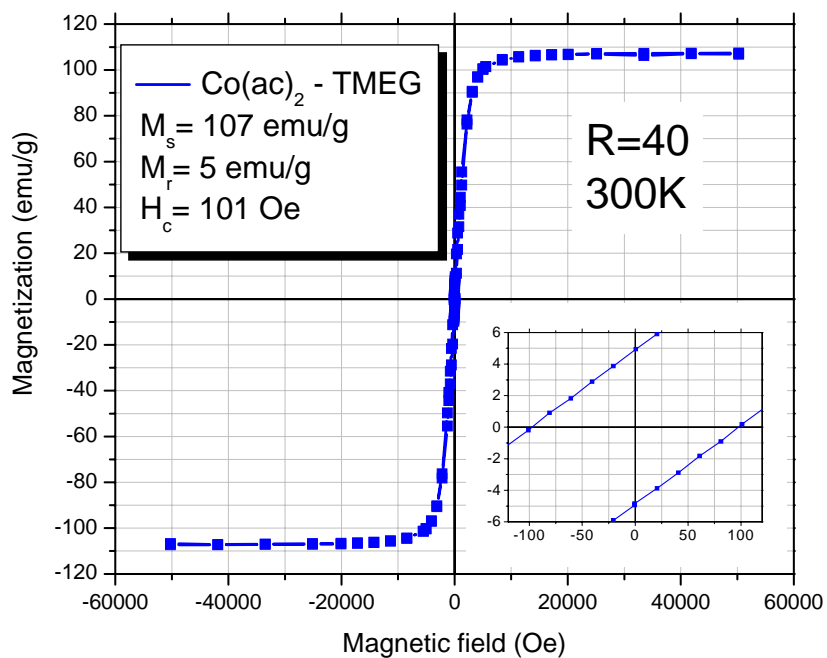


Figure 4.5: M-H loops for Co powders as-synthesized from 0.01M Co solution using Co(ac)₂, TMEG at 487 ± 5 K, 'R' = 45 and 240 minutes of reaction time. The insert show the M-H loop around the origin.

Our results are in good agreement with those reported by Perales *et al.* [27] where predominant fcc-Co was the most stable phase under similar conditions of synthesis in EG. However, the mentioned work did not study the solids produced in TEG or TREG. In our case the formation of metastable compounds, such as ϵ -Co, in TMEG can be attributed to the stronger reduction conditions we may have achieved by using a high-boiling point polyol as TMEG (BP = 487 K). Therefore, TMEG was selected for the rest of our work.

4.1.3 Morphological analyses

Figures 4.6 to 4.8 show SEM images of cobalt particles synthesized using $\text{Co}(\text{ac})_2$ as precursor and EG, TEG or TMEG as the reducing reagent. As evident, the morphological features were strongly dependent on the kind of polyol. The solids produced in EG and TEG consisted of strongly aggregated sub-micron particles without defined shape. On the contrary, fairly smooth spherical particles were produced in TMEG. Particle size ranged from 1 to 5 μm in diameter. Furthermore, a more careful analysis of the SEM images revealed that each particle consists of tiny individuals, which are strongly aggregated, evidencing the polycrystallinity in the samples.

SYNTHESIS IN EG

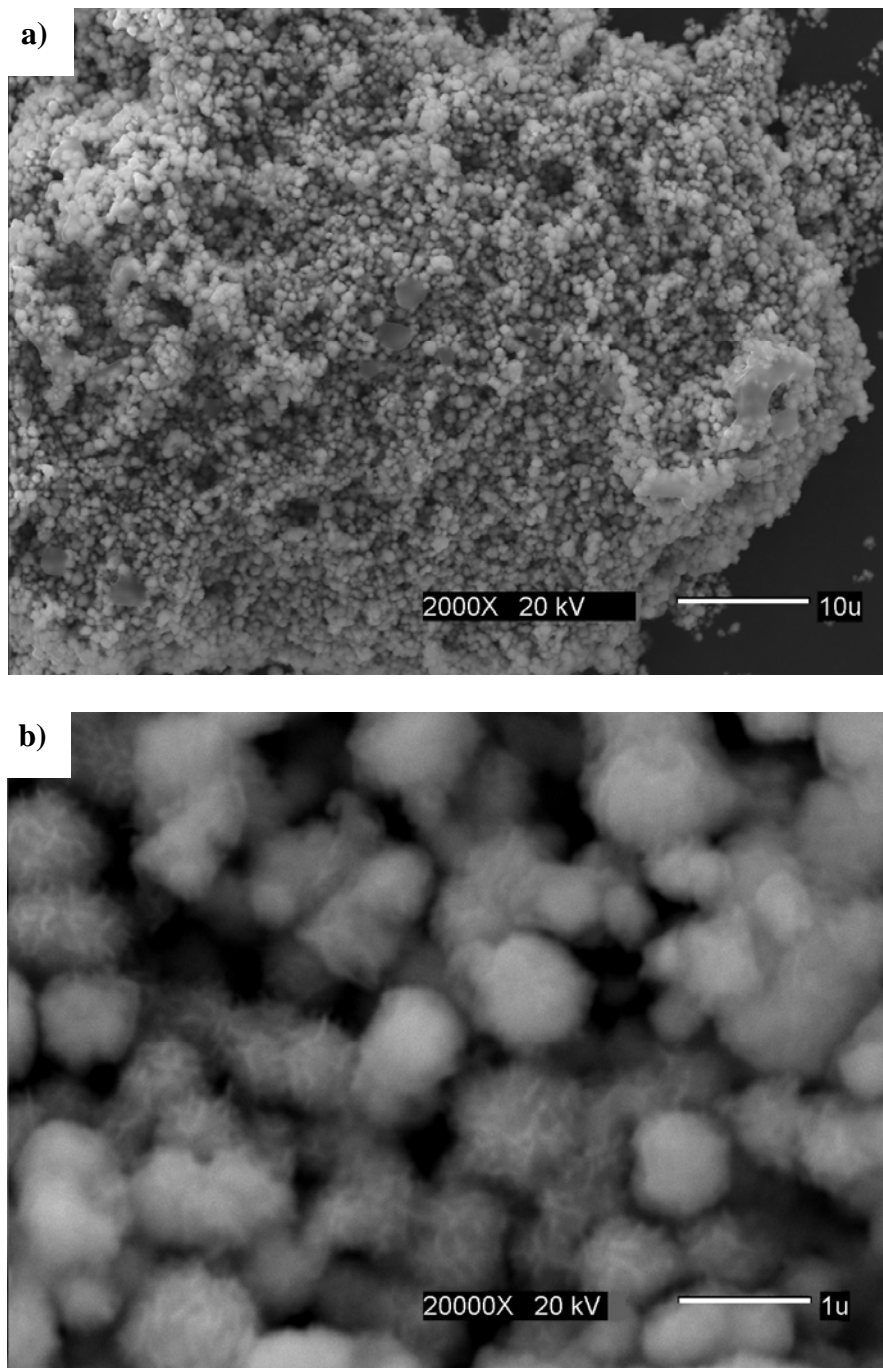


Figure 4.6: SEM images of cobalt particles synthesized from 0.01M Co solution using $\text{Co}(\text{ac})_2$ as metal salt, EG at 468 ± 5 K, 'R' = 45 and 64 min. of reaction time. The scale bar in a) represents 10 μm and in the detail b) represents 1 μm .

SYNTHESIS IN TEG

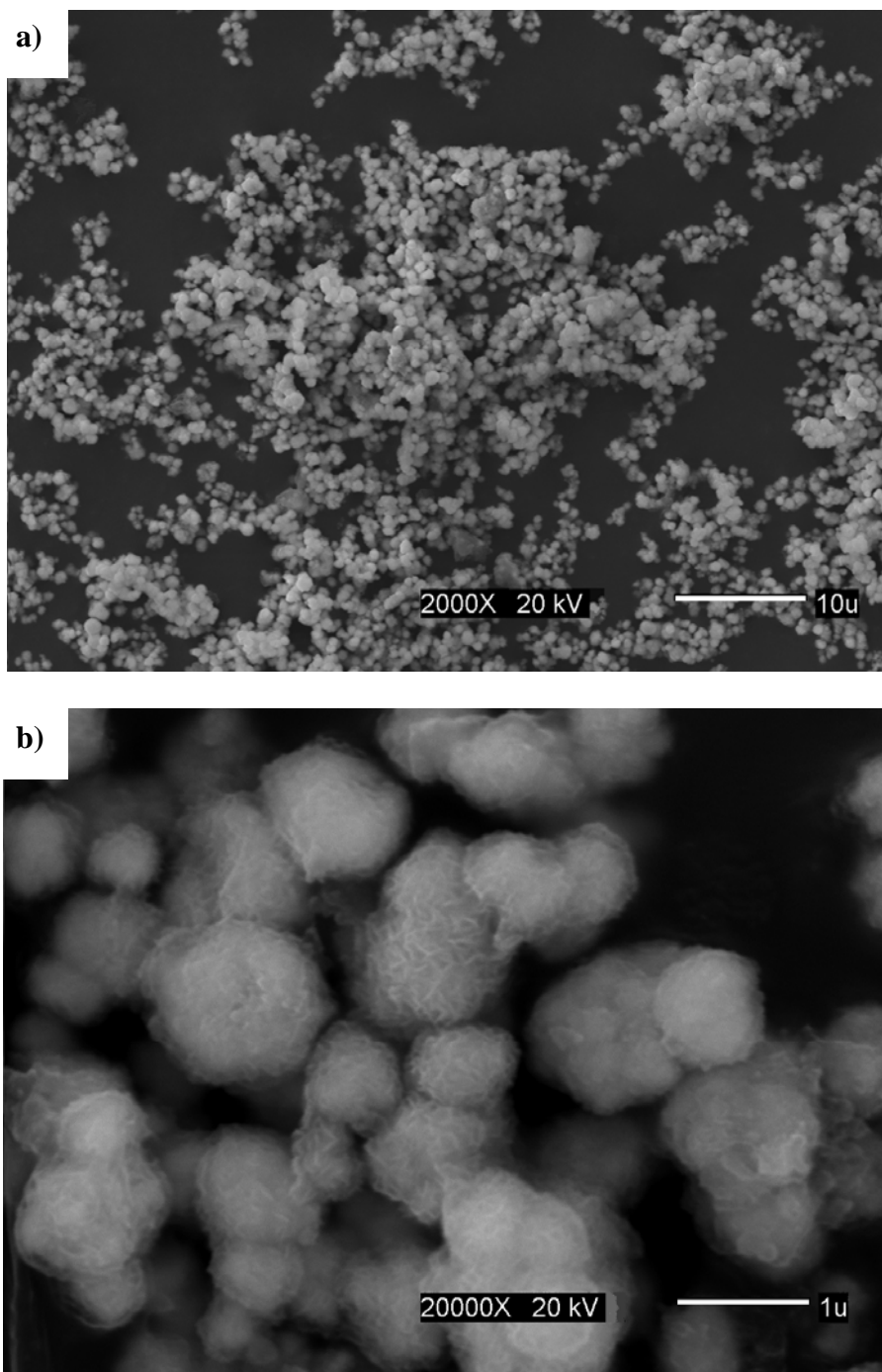


Figure 4.7: SEM images of cobalt particles synthesized from 0.01M Co solution using $\text{Co}(\text{ac})_2$ as metal salt, TMEG at 468 ± 5 K, 'R' = 30 and 83 min. of reaction time. The scale bar in a) represents $10 \mu\text{m}$ and in the detail b) represents $1 \mu\text{m}$.

SYNTHESIS IN TMEG

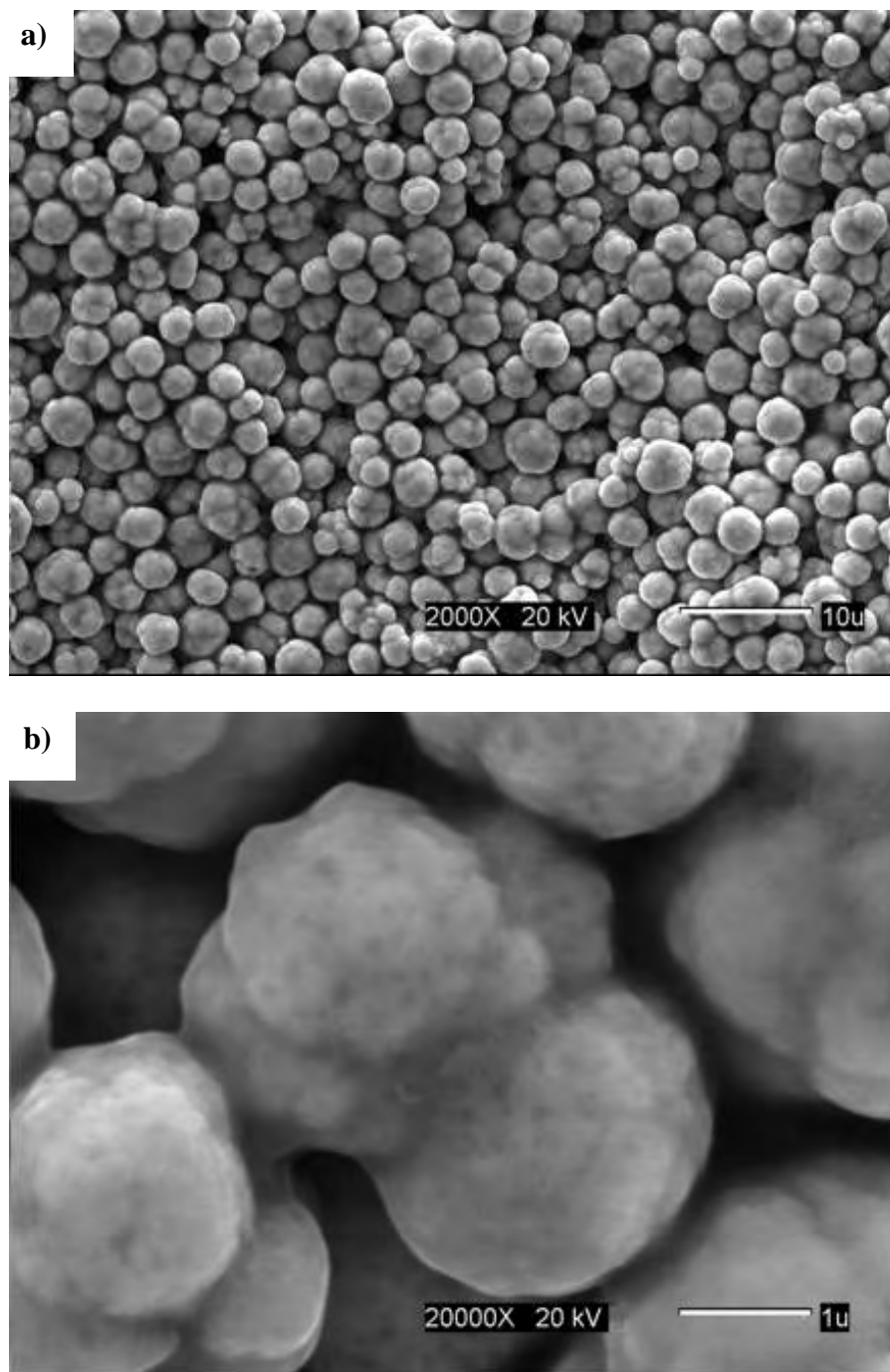


Figure 4.8: SEM images of cobalt particles synthesized from 0.01M Co solution using $\text{Co}(\text{ac})_2$ as metal salt, TMEG at 487 ± 5 K, 'R' = 40 and 240 min of reaction time. The scale bar in a) represents 10 μm and in the detail b) represents 1 μm .

4.2 Effect of the OH⁻/Co mole ratio and type of cobalt source

As stated in the above paragraph, TMEG was selected as the solvent and reducing agent for the rest of our research. A reaction time of 4 hours was considered long enough to achieve the complete transformation of the intermediate into metallic cobalt. Based on the verified catalytic effect of OH⁻ ions, the effect of the OH⁻/Co mole ratio on the rate of the metal forming reaction and phase stability was investigated. Moreover, the probable differences in the nature of the intermediate compound was studied by using two different cobalt salts (acetate and acetylacetonate salts) as precursors.

4.2.1 Structural characterization

Figure 4.9 shows the XRD patterns corresponding to the precipitates obtained after 4 hours of reaction. In absence of OH⁻ ions, i. e. 'R'= 0, only hydroxi-alcooxide-like intermediate was formed (Cobalt oxide hydroxide-CoOOH-hcp- PDF # 26 1107; Beta D mannitol-C₆H₁₄O₆-orthorhombic- PDF # 22 1797; Hexa-aquacobalt dihydrogen 1,2,4,5 benzenetetracarboxylate-C₁₀H₁₆CoO₁₄-monoclinic- PDF # 45 1707; sodium methylate-CH₃NaO-tetragonal- PDF # 19 1876) when both Co precursor salts were used. However, as the sharpness and intensities of the XRD peaks suggest, the intermediate obtained from Co(ac)₂ seems to be more crystalline than the one precipitated from Co(acac)₂ solutions.

Metallic cobalt was formed only for 'R' values of 30 and above. The presence of OH⁻ ions may have accelerated the dissolution of the intermediates to give dissolved cobalt species, which were finally reduced into the metallic state. This catalytic role of OH⁻ ions in the formation of metallic cobalt was also reported in related works from our group [27]. Moreover, the less crystalline nature of the intermediate produced at R=0 from Co(acac)₂ solutions can be related to a high solubility. It is well-known that amorphous solids exhibit larger solubility than the crystalline ones. Figure 4.11 also evidenced that the addition of OH⁻ ions also affected the stability of metallic cobalt phases. Fcc-Co was the predominant phase at 'R' = 30 when Co(ac)₂ was used. The average crystallite size was estimated at 7.7 nm using Scherrer's equation. The corresponding lattice parameter was $a = 3.523 \text{ \AA}$. This value is smaller than the reported for the bulk ($a = 3.545 \text{ \AA}$, PDF # 15 0806 [9]). The observed difference can be explained by the presence of micro-strains in the fcc-Co unit cell. The use of the Williamson Hall analysis to estimate the micro-strain in the lattice was not used because of the noise in the XRD patterns. On the other hand, metastable ϵ -Co co-existed with fcc-Co and hcp-Co when the solids were synthesized from Co(acac)₂ solutions. The lattice parameter a for the fcc-Co phase was 3.540 \AA , which is in good agreement with the bulk value. The lattice parameter a for the ϵ -Co was estimated at 6.230 \AA . This value was higher than the lattice parameter reported by Dmitry *et al.* for ϵ -Co (6.097 \AA) synthesized by the thermal decomposition of metal carbonyls [10]. A more

detailed discussion regarding the observed discrepancies in the lattice dimensions will be included in the following sections.

As figure 4.12 shows, ϵ -Co co-existed with hcp- and fcc-Co, when $\text{Co}(\text{ac})_2$ and $\text{Co}(\text{acac})_2$ were used as precursor salts at $R=40$. In the case of $\text{Co}(\text{ac})_2$ the fcc-Co structure has a lattice parameter of $a = 3.535 \text{ \AA}$ that is smaller than at reported by the PDF [9] (3.545 \AA). The noise in the XRD signals difficult a precise estimation of the lattice parameters for the hcp-Co phase. The corresponding lattice parameter for ϵ -Co was 6.209 \AA . On the other hand, metastable ϵ -Co co-existed with hcp-Co when $\text{Co}(\text{acac})_2$ was the precursor salt. The lattice parameter of the ϵ -Co phase was estimated at $a = 6.209 \text{ \AA}$, which is good agreement with our previous calculation.

Figure 4.13 shows the XRD patterns for the solids produced from precursors $\text{Co}(\text{ac})_2$ and $\text{Co}(\text{acac})_2$ at $R = 50$. In both cases, the solids consisted of a mixture of ϵ - and hcp-Co phases; however, the fcc-Co structure was identified only in the sample produced from the acetate precursor. The use of $\text{Co}(\text{acac})_2$ could have accelerated the kinetics of the intermediate dissolution-cobalt reduction reactions and hence, the formation of metastable hcp- and ϵ -Co nanostructures.

The corresponding fcc-Co lattice parameter was roughly estimated at 3.576 \AA . The lattice parameters for the hcp-Co and the ϵ -Co phases produced from starting $\text{Co}(\text{acac})_2$ solutions were estimated at $a = 2.456 \text{ \AA}$ and $c = 4.368 \text{ \AA}$ and $a = 6.180 \text{ \AA}$, respectively. The corresponding average crystallite size, estimated by using Scherrer's equation, was around 11-15 nm for the hcp- and ϵ -Co phases.

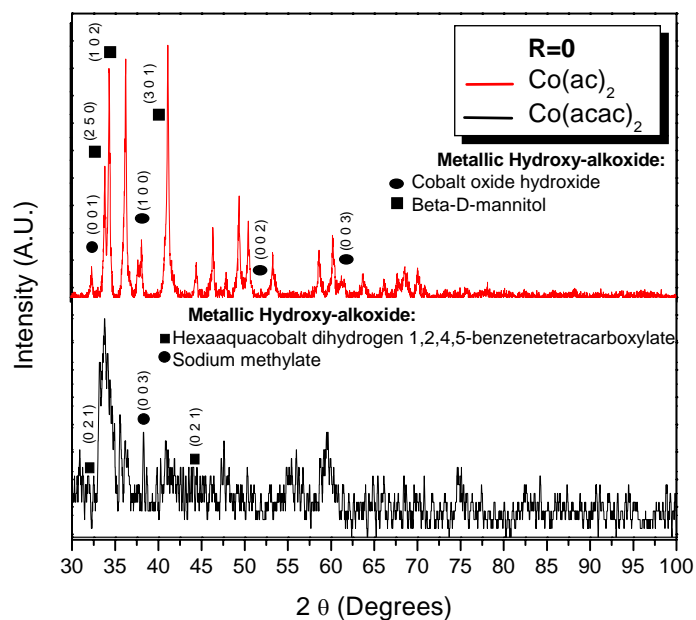


Figure 4.9: XRD patterns of as-synthesized intermediate compound (like hydroxy-alkoxide) of cobalt powders from 0.01M Co solutions using $\text{Co}(\text{ac})_2$ and $\text{Co}(\text{acac})_2$ salt precursors in TMEG at 487 ± 5 K.

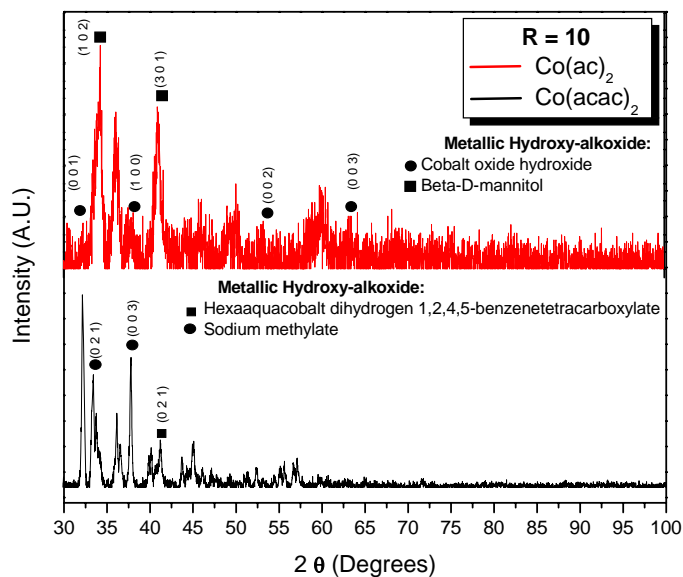


Figure 4.10: XRD patterns of as-synthesized intermediate compound (like hydroxy-alkoxide) of cobalt powders from 0.01M Co solutions using $\text{Co}(\text{ac})_2$ and $\text{Co}(\text{acac})_2$ salt precursors in TMEG at 487 ± 5 K.

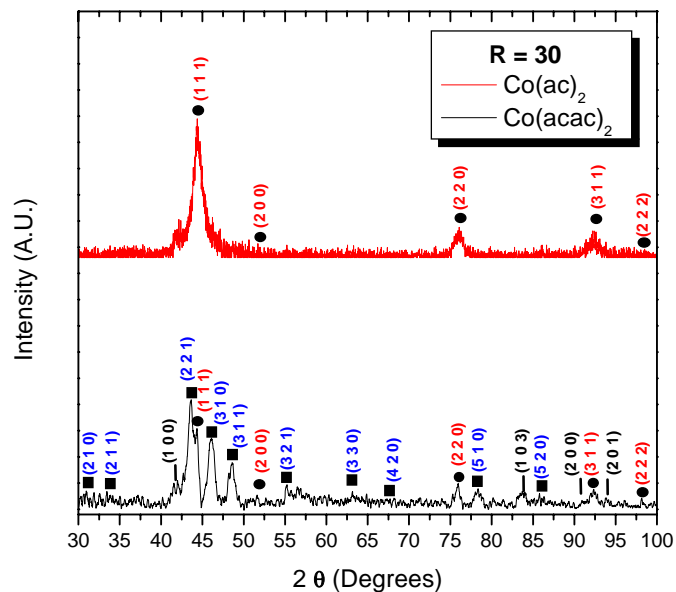


Figure 4.11: XRD patterns of as-synthesized cobalt powders from 0.01M Co solutions using Co(ac)₂ and Co(acac)₂ precursors, TMEG at 487±5 K. Peaks corresponding to fcc (●), hcp (|) and ε (■) cobalt phases are indicated.

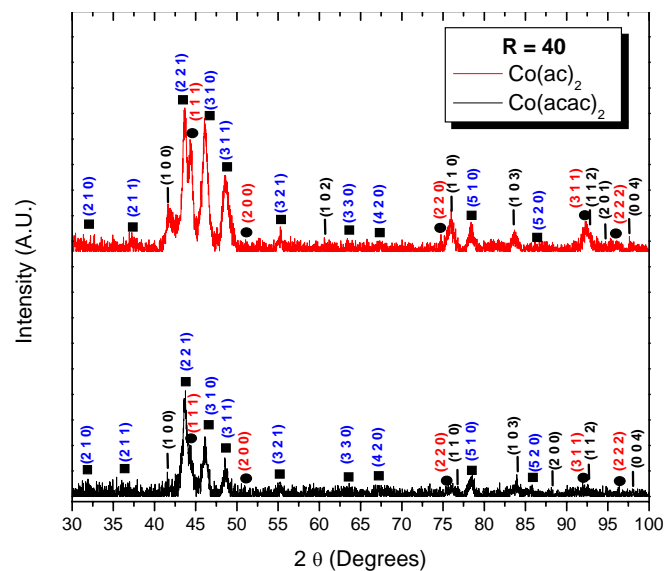


Figure 4.12: XRD patterns of as-synthesized cobalt powders from 0.01M Co solutions using Co(ac)₂ and Co(acac)₂ precursors, TMEG at 487±5 K. Peaks corresponding to fcc (●), hcp (|) and ε (■) cobalt phases are indicated.

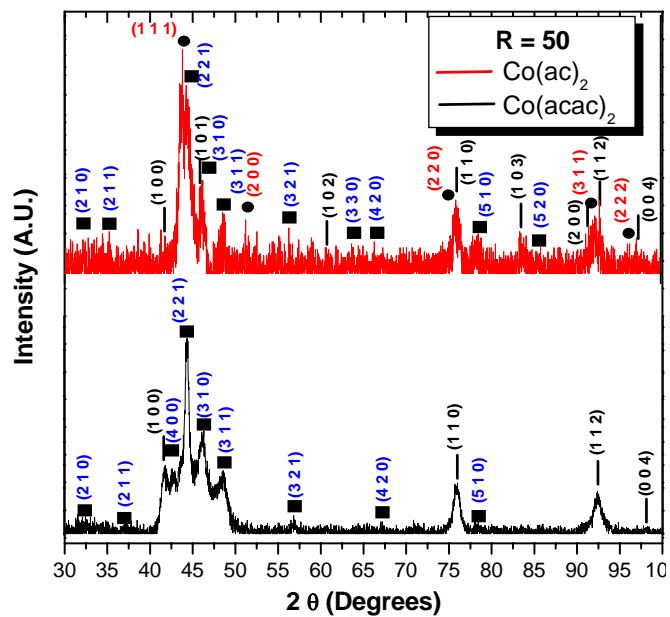


Figure 4.13: XRD patterns of as-synthesized cobalt powders from 0.01M Co solutions using $\text{Co}(\text{ac})_2$ and $\text{Co}(\text{acac})_2$ precursors, TMEG at 487 ± 5 K. Peaks corresponding to fcc (●), hcp (|) and ϵ (■) cobalt phases are indicated.

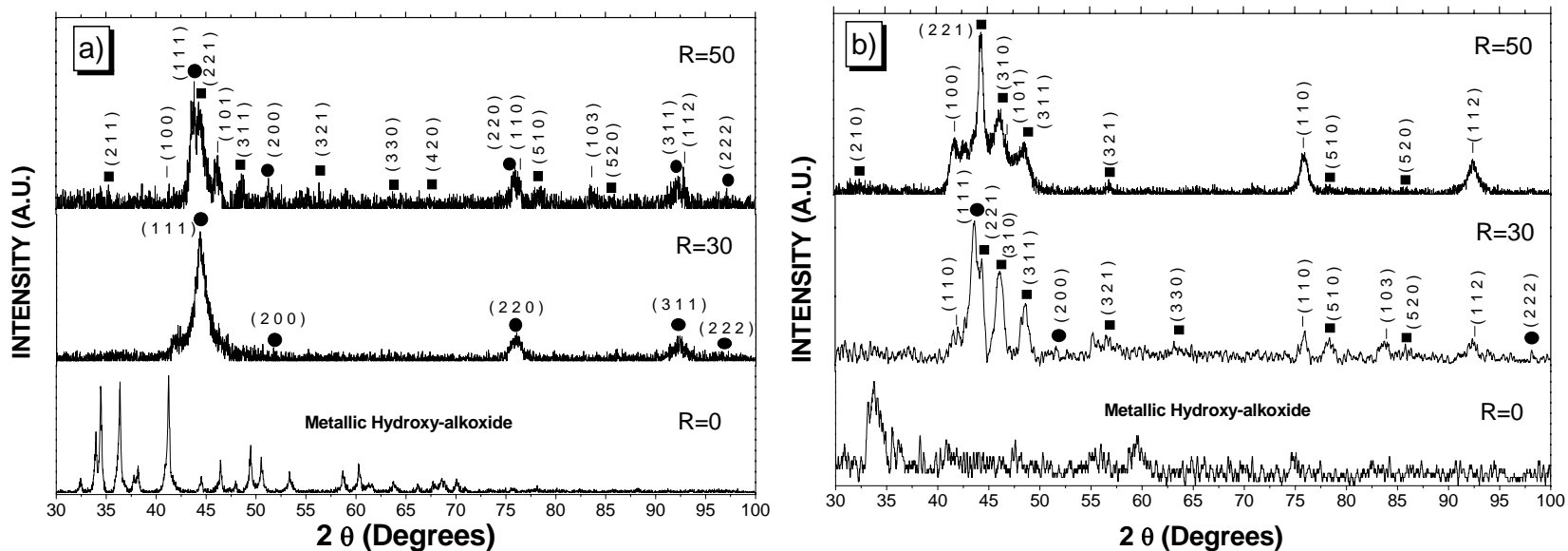


Figure 4.14: Comparative results. XRD patterns of as-synthesized cobalt powders from 0.01M Co solutions using: a) $\text{Co}(\text{ac})_2$, and b) $\text{Co}(\text{acac})_2$ precursors and 4 h of reaction time. Peaks corresponding to fcc (●), hcp (▲) and ϵ (■) cobalt phases are indicated. Peaks corresponding to the sample produced at ‘R’= 0 correspond to a family of hydroxide-alkoxide compounds.

4.2.2 Morphological analyses

Figures 4.15 to 4.19 show the SEM images of the cobalt precipitates obtained at different 'R' values and using $\text{Co}(\text{ac})_2$ as precursor. As evident, the morphological features are quite different depending on the synthesis conditions. The solids produced at 'R' = 0 consisted of monosize bi-pyramidal particles (Figure 4.15). According to XRD information, these monodisperse particles should correspond to the non-magnetic hydro-alcoide intermediates. These particles loose their original morphology under alkaline conditions. As the SEM image of Figure 4.16 suggests, the partial dissolution of the intermediate took place when the solids were produced at R=10. Extremely high alkaline conditions achieved at R=10 would have accelerated the dissolution process. When particles of metallic cobalt were identified in the reaction products (Figures 4.17-18), they were sub-micrometric individuals (1-5 μm in diameter) and exhibited an irregular surface. Figure 4.19 shows strongly aggregated sub-micrometric individuals, forming particles with irregular shape, produced at R = 50.

A different morphological pathway was evidenced when $\text{Co}(\text{acac})_2$ was used as the precursor. As shown in figures 4.20 and 4.21, the intermediate produced at 'R' = 0 and 10 consisted of extremely tiny particles in the sub-micrometric range. The bi-pyramidal shape exhibited for the solids produced from $\text{Co}(\text{ac})_2$ solutions was not observed in this case. This morphological feature, i.e., quite small particle size of the intermediate phase, could support our earlier statement regarding the enhanced solubility of the less crystalline and smaller intermediate particles and

its role on the subsequent formation of metastable cobalt phases. Figure 4.22 shows the strongly aggregated micrometric particles (1-3 μm in diameter) formed at 'R' = 30. Similar features were observed in the solids produced at R= 50 (Figure 4.23). Highly monodisperse spherical particles were produced under extremely high alkaline conditions (R = 50).

Generally speaking, cobalt particles produced from $\text{Co}(\text{ac})_2$ precursor were bigger than the ones produced by using $\text{Co}(\text{acac})_2$. The smaller particle size in the samples is attributed to a faster nucleation rate, promoted by the enhanced dissolution of the intermediate under alkaline conditions. Although somehow monodisperse, the particles produced from $\text{Co}(\text{ac})_2$ solutions exhibit a rough and irregular surface, which contrasts with the smooth surface in those particles produced from $\text{Co}(\text{acac})_2$ precursor.

Evidently, the different nature (morphology, solubility at high temperatures and under alkaline conditions) of the intermediate phase produced from different cobalt precursors, should be involved with these morphological features. The monodispersity in Co particles synthesized at 'R' = 50 can be attributed to the adsorption of negative acetylacetonate species, which would prevent excessive growth and aggregation between particles by providing them with a net negative surface charge and the establishment of electrostatic repulsive interactions. The adsorption of negative OH^- ions, which should have also contributed to the negative surface charge, can also be involved with the observed monodispersity [27]. Besides, a higher concentration of OH^- ions should have also accelerated

both the dissolution of the intermediate phase and reduction reaction, and hence, promoted a higher nucleation rate. SEM images also evidenced that all the cobalt particles are in the micrometer size range. Since the average crystallite size estimated from XRD data was in the range of 8 to 20 nm, all produced particles can be considered as polycrystalline. Careful observation of the SEM image, will verify that each particle consists of tiny individuals, i.e. the crystallites, strongly aggregated. These crystallites should have been irreversibly aggregated in order to decrease the total surface energy of the system. Apparently, the electrostatic repulsive interactions generated by the adsorbed species would have not been strong enough to prevent nanocrystal aggregation. The use of surfactants or an excess of stronger complexing agents (e. g., acetate and acetylacetonate species) could help the inhibition of particle aggregation.

FROM COBALT ACETATE

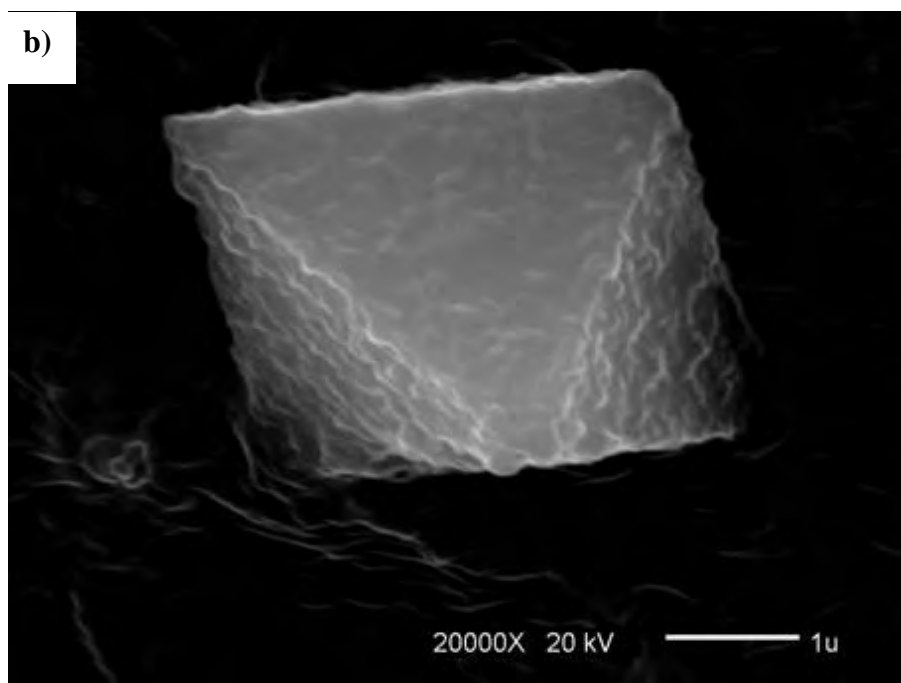
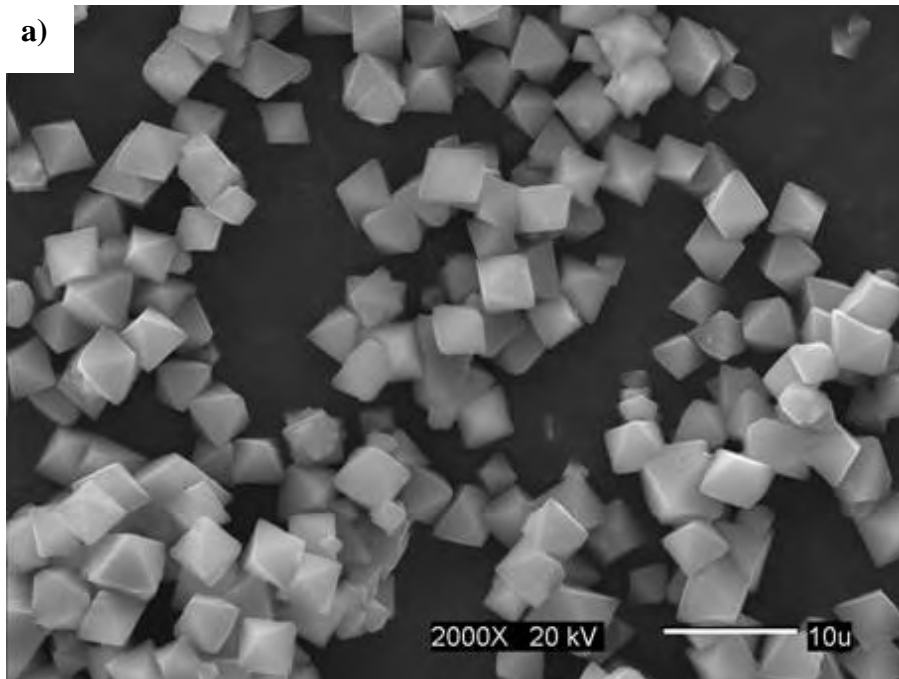


Figure 4.15: SEM images of bi-pyramidal intermediate (hydroxi-alcoxides) synthesized from 0.01M Co solution using $\text{Co}(\text{ac})_2$ as salt, TMEG at 487 ± 5 K, 'R' = 0 and 4 h of reaction time.

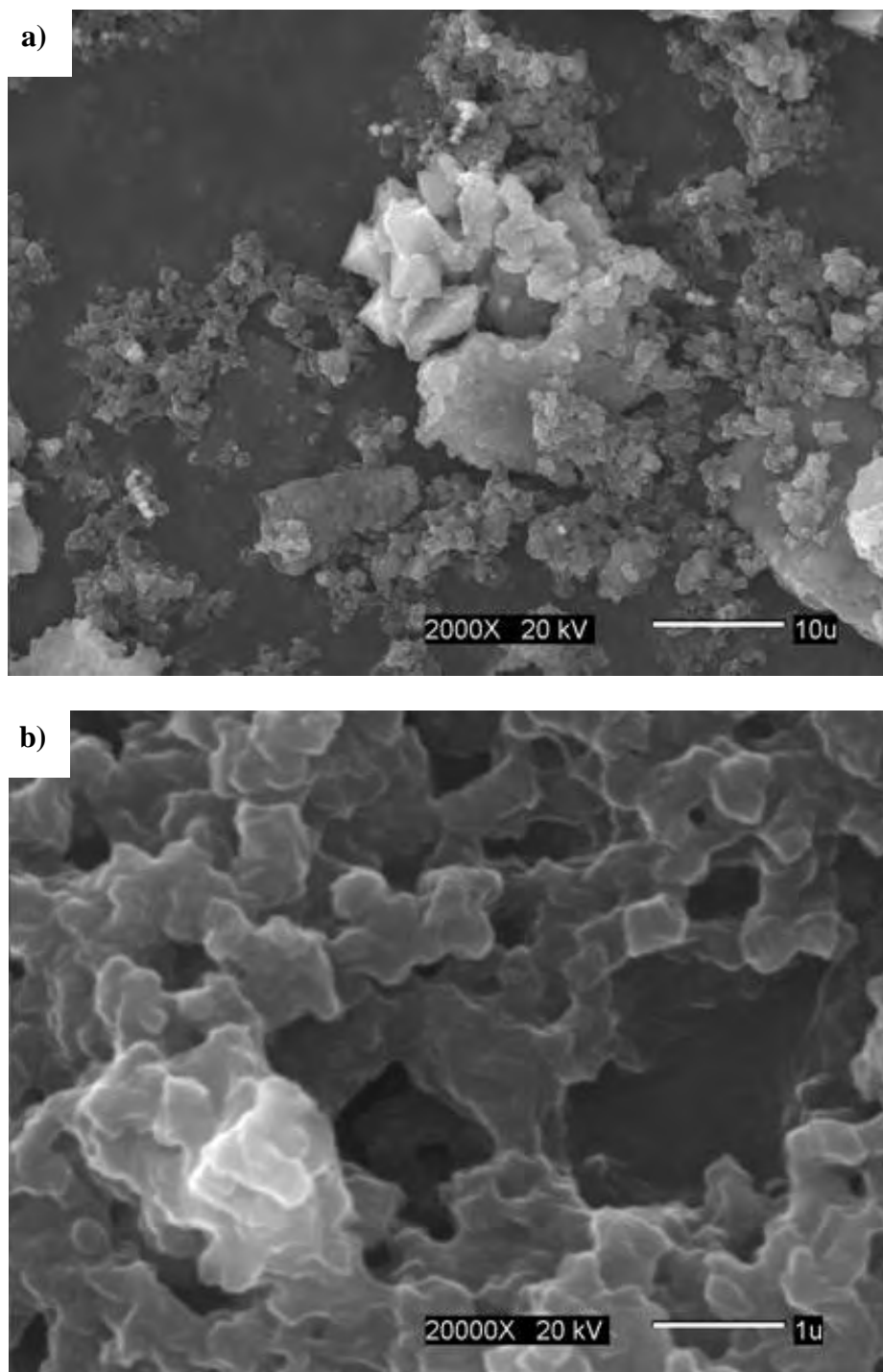


Figure 4.16: SEM images of dissolved intermediate synthesized from 0.01M Co solution using $\text{Co}(\text{ac})_2$ as salt, TMEG at 487 ± 5 K, 'R' = 10 and 4 h of reaction time.

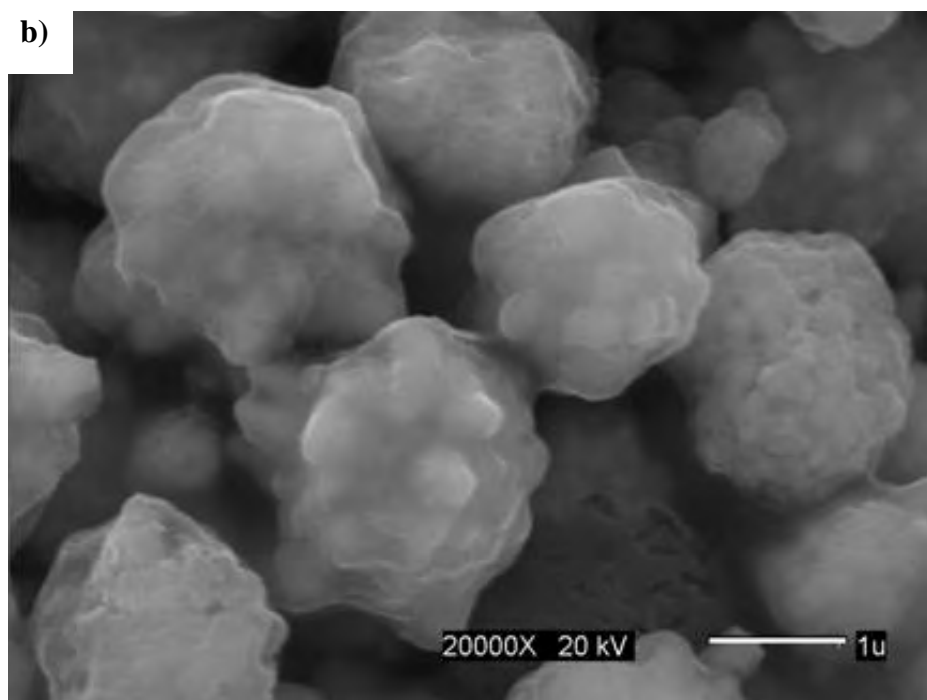
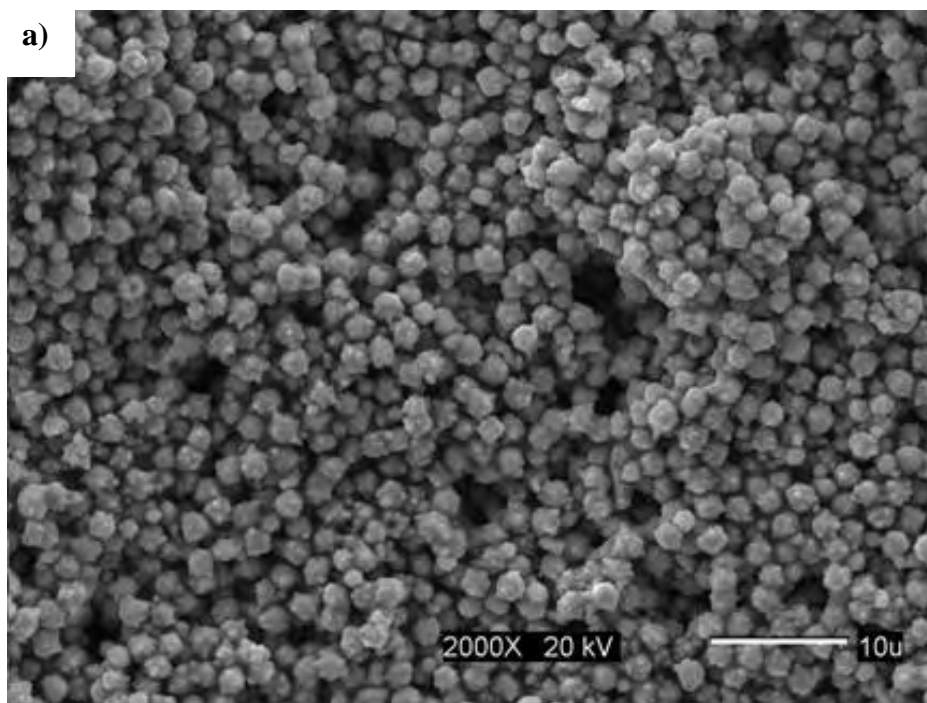


Figure 4.17: SEM images of cobalt particles synthesized from 0.01M Co solution using $\text{Co}(\text{ac})_2$ as metal salt, TMEG at 487 ± 5 K, 'R' = 30 and 4 h of reaction time.

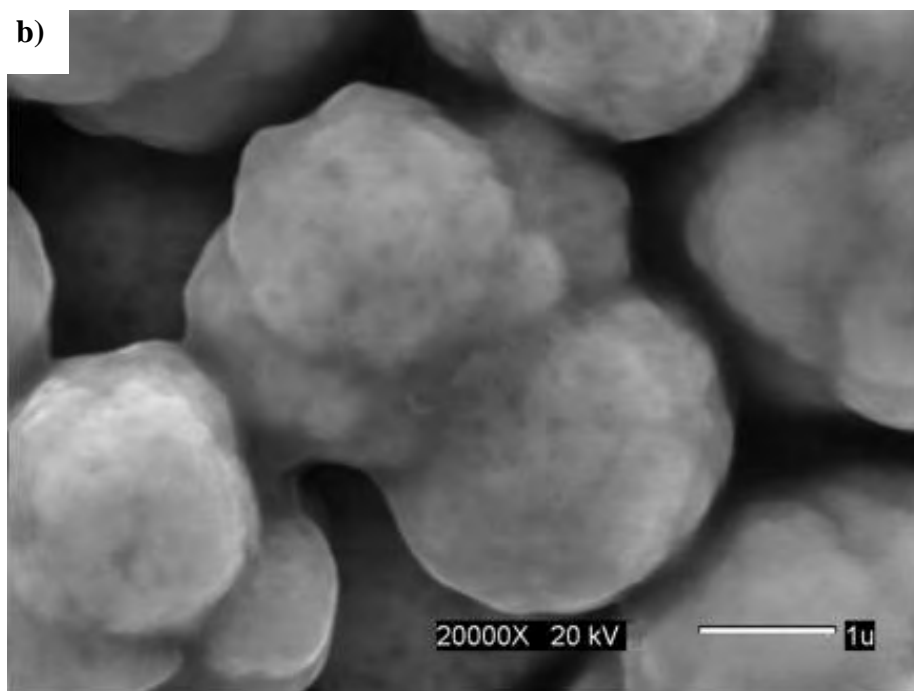
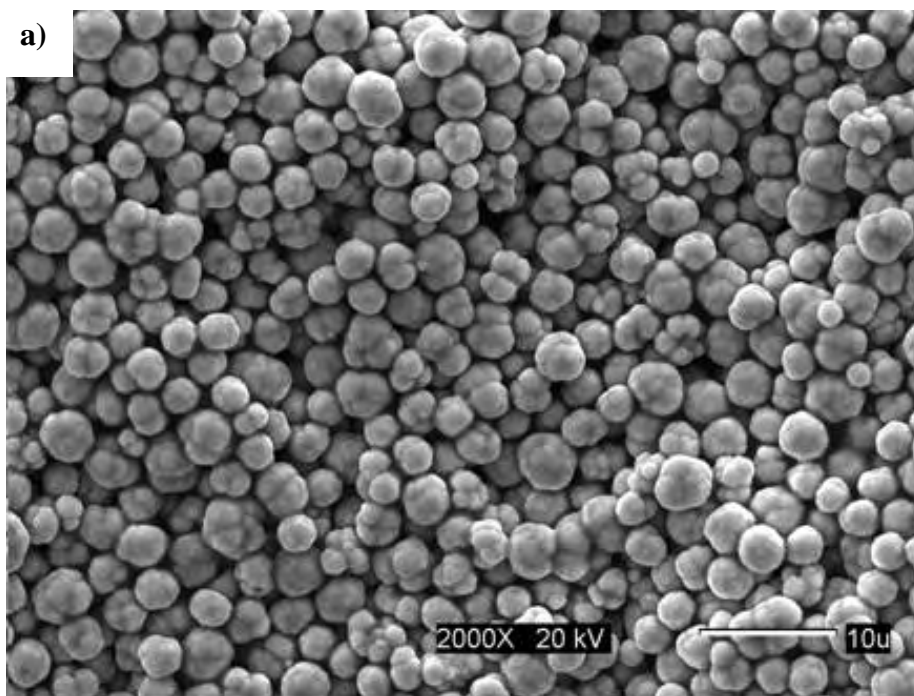


Figure 4.18: SEM images of cobalt particles synthesized from 0.01M Co solution using $\text{Co}(\text{ac})_2$ as metal salt, TMEG at 487 ± 5 K, 'R' = 40 and 4 h of reaction time.

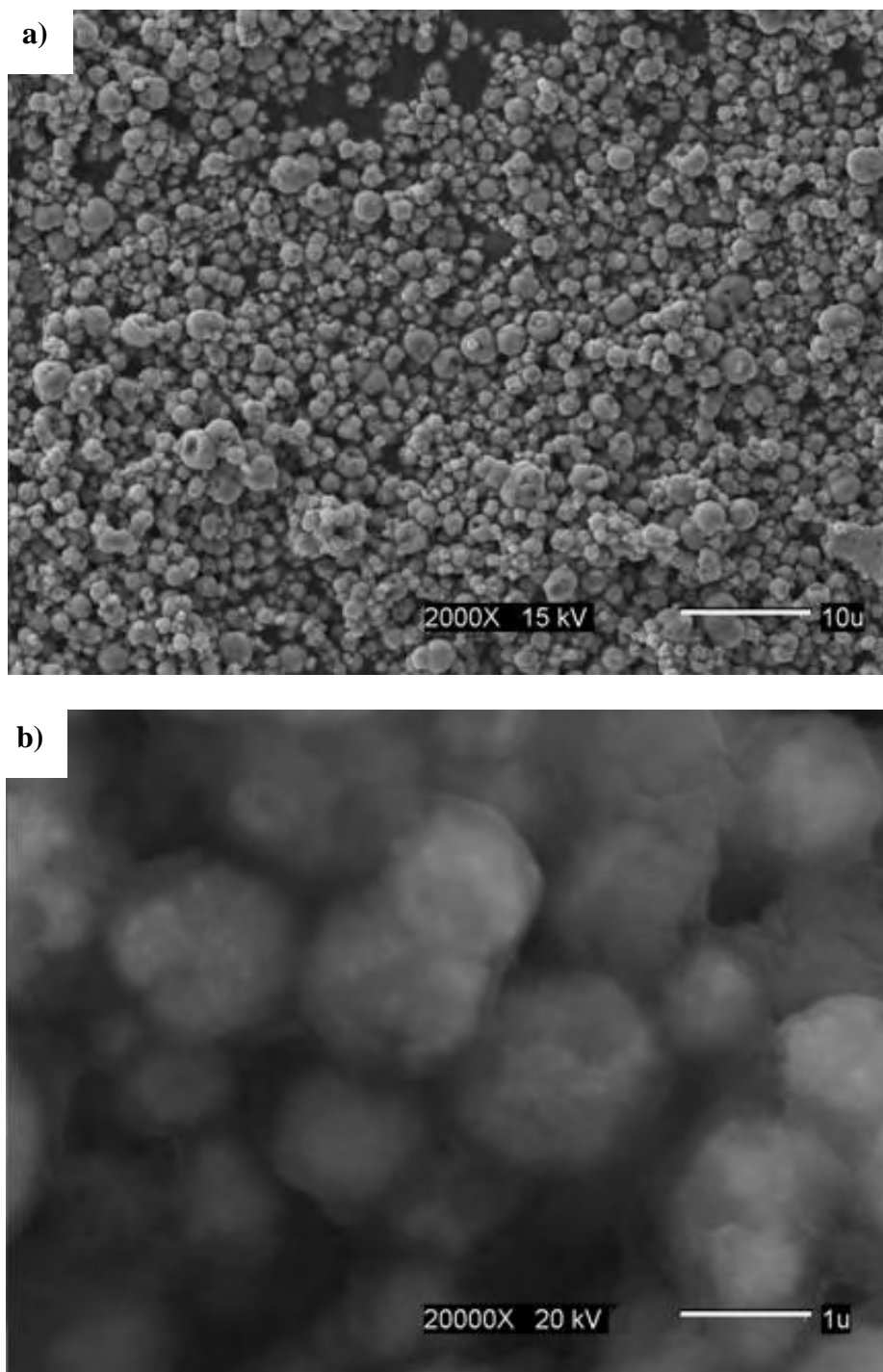


Figure 4.19: SEM images of cobalt particles synthesized from 0.01M Co solution using $\text{Co}(\text{ac})_2$ as salt, TMEG at 487 ± 5 K, 'R' = 50 and 4 h of reaction time.

FROM COBALT ACETYLACETONATE

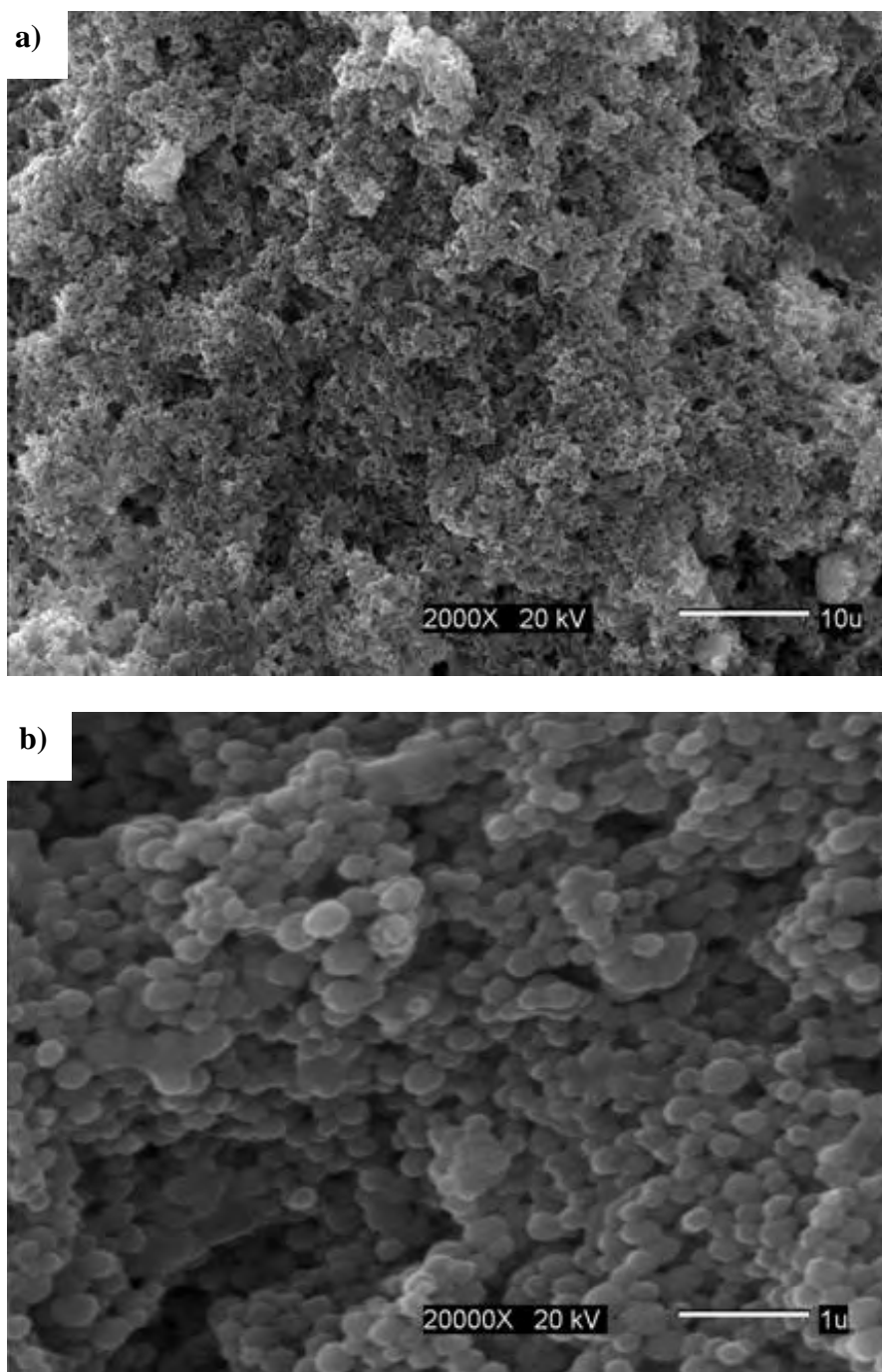


Figure 4.20: SEM images of dissolved intermediate synthesized from 0.01M Co solution using $\text{Co}(\text{acac})_2$ as salt, TMEG at 487 ± 5 K, 'R' = 0 and 4 h of reaction time.

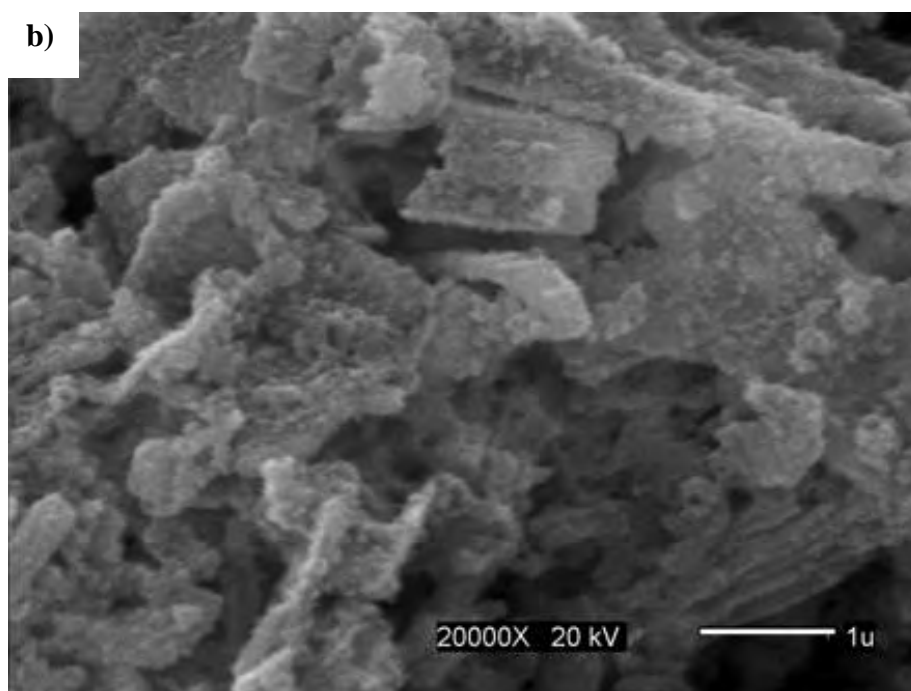
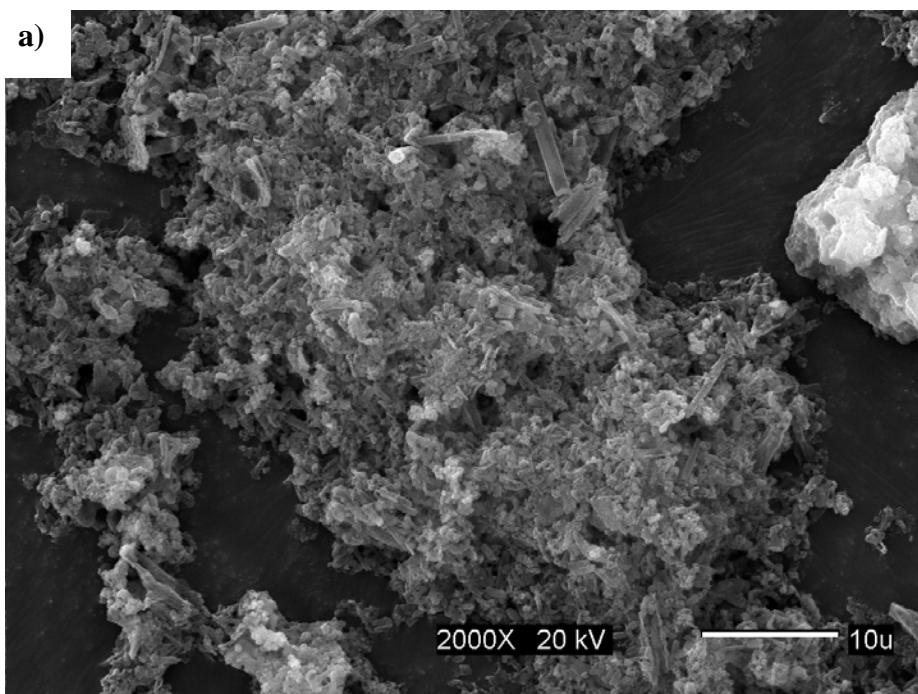


Figure 4.21: SEM images of dissolved intermediate synthesized from 0.01M Co solution using $\text{Co}(\text{acac})_2$ as salt, TMEG at 487 ± 5 K, 'R' = 10 and 4 h of reaction time.

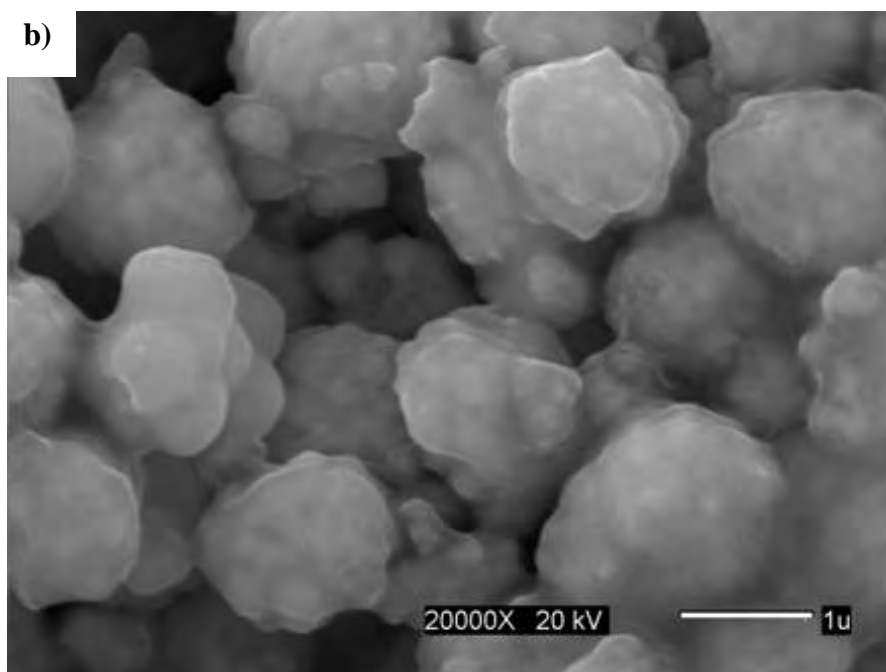
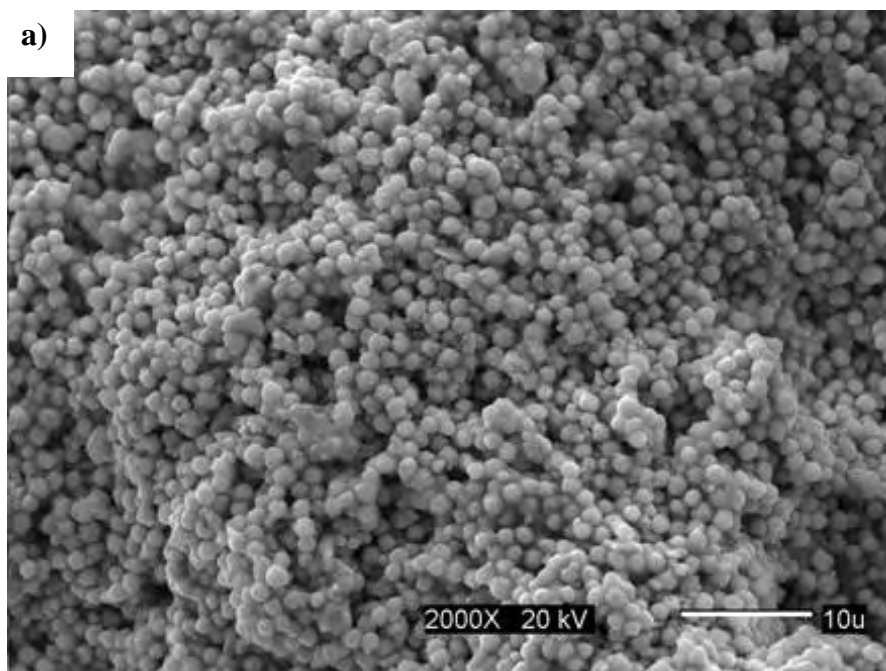


Figure 4.22: SEM images of cobalt particles synthesized from 0.01M Co solution using $\text{Co}(\text{acac})_2$ as metal salt, TMEG at 487 ± 5 K, 'R' = 30 and 4 h of reaction time.

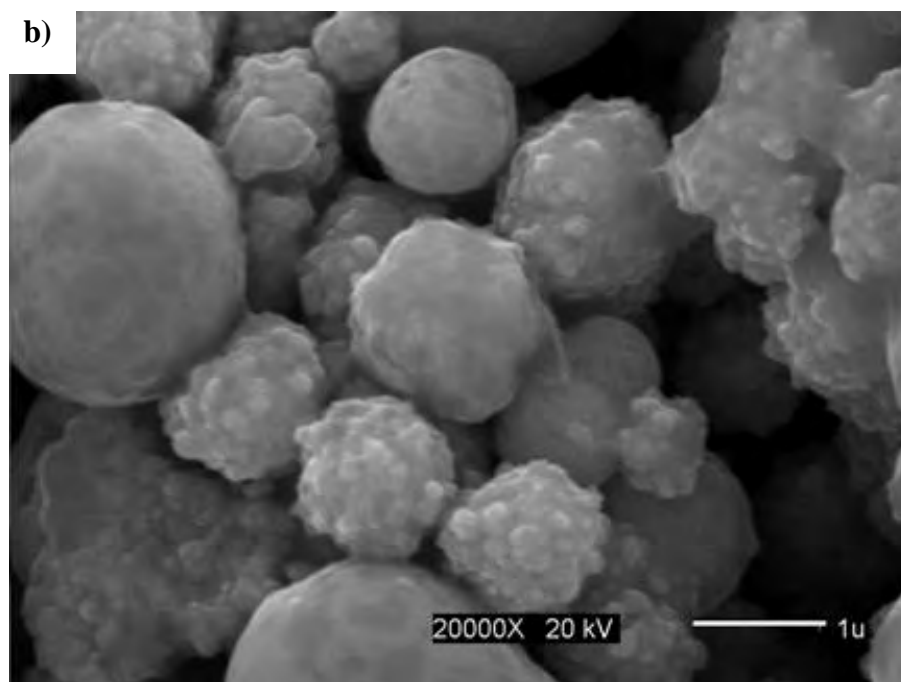
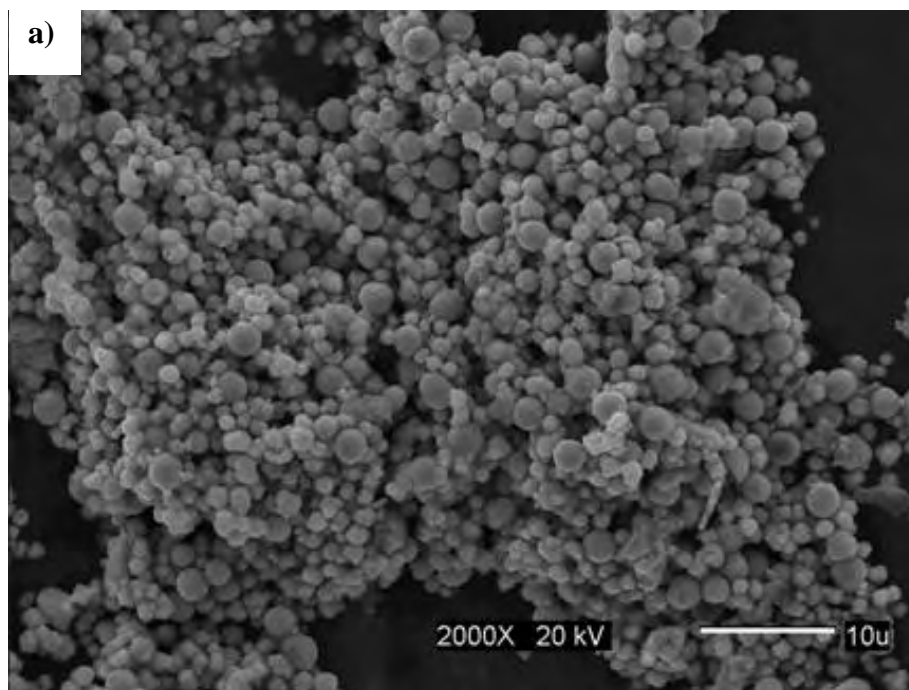


Figure 4.23: SEM images of cobalt particles synthesized from 0.01M Co solution using $\text{Co}(\text{acac})_2$ as metal salt, TMEG at 487 ± 5 K, 'R' = 40 and 4 h of reaction time.

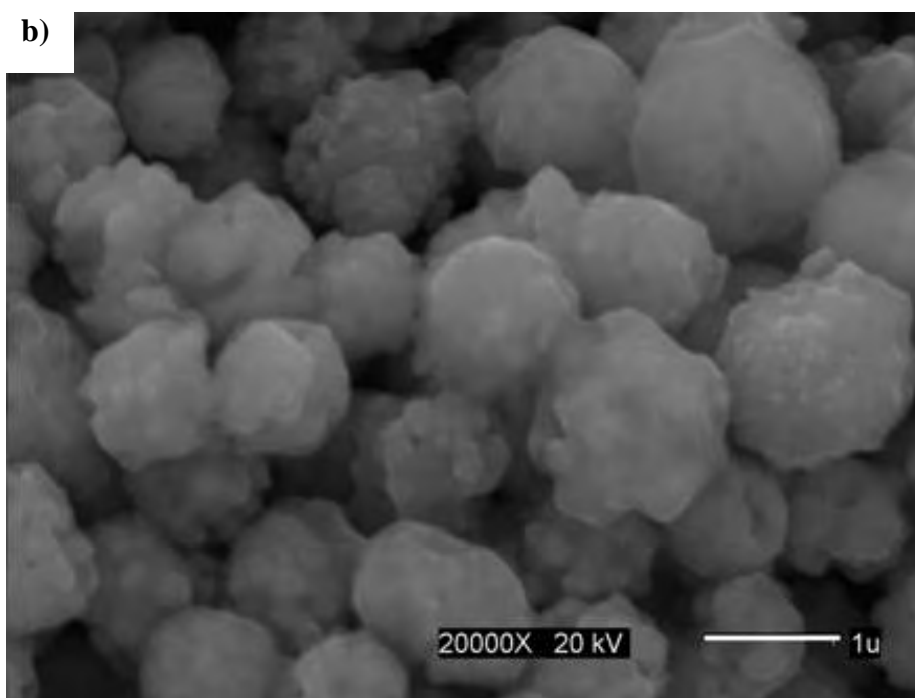
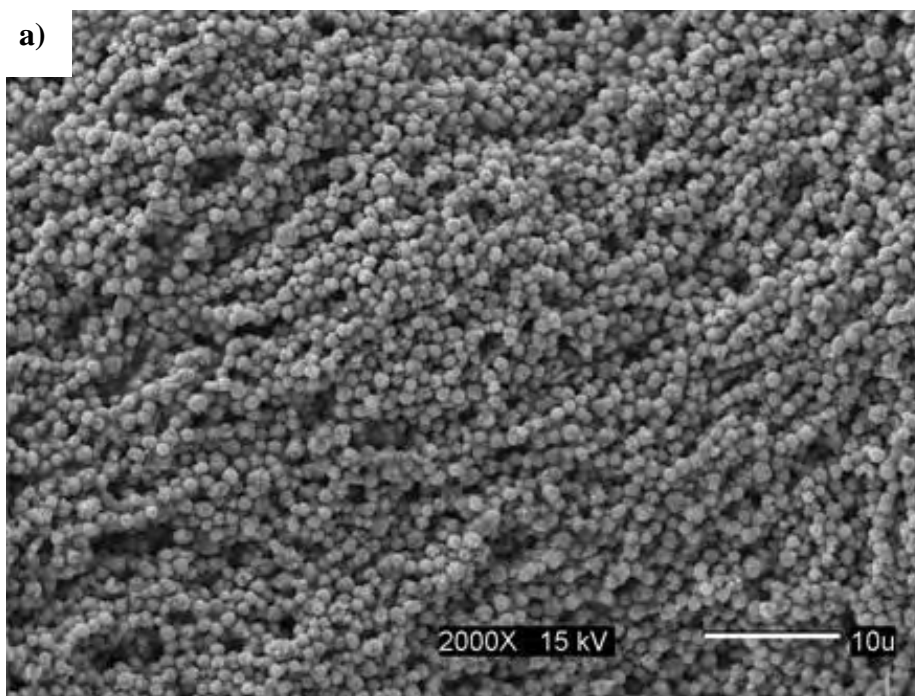


Figure 4.24: SEM images of cobalt particles synthesized from 0.01M Co solution using $\text{Co}(\text{acac})_2$ as metal salt, TMEG at 487 ± 5 K, 'R' = 50 and 4 h of reaction time.

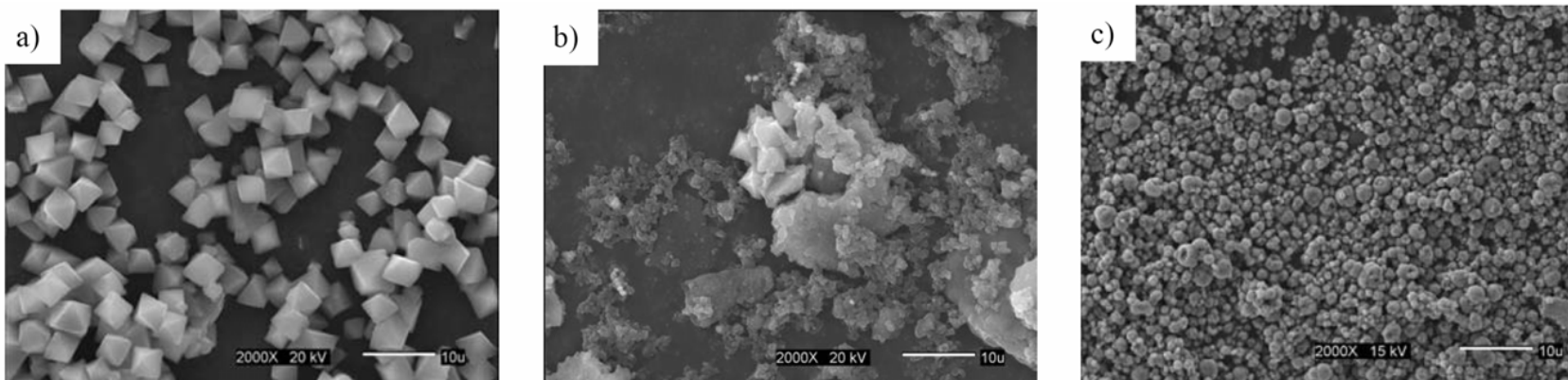


Figure 4.25: SEM images of cobalt particles synthesized in TMEG at 487 ± 5 K with different 'R' values and using $\text{Co}(\text{ac})_2$ as source of cobalt ions: a) 'R' = 0; b) 'R' = 10 and c) 'R' = 50. The scale bar represents 10 μm .

97

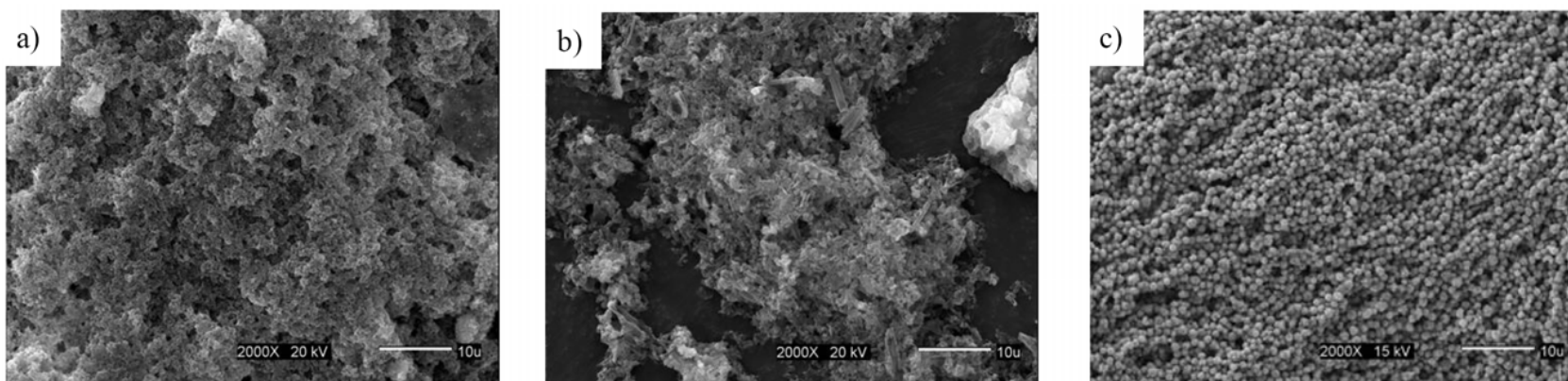


Figure 4.26: SEM images of cobalt particles synthesized in TMEG at 487 ± 5 K with different conditions using $\text{Co}(\text{acac})_2$ as source of cobalt ions: a) 'R' = 0; b) 'R' = 10 and c) 'R' = 50. The scale bar represents 10 μm .

4.2.3 Magnetic characterization

Figures 4.27-29 shows the saturated M-H hysteresis loops for the cobalt solids produced at 'R' of 30, 40 and 50 and using $\text{Co}(\text{ac})_2$ or $\text{Co}(\text{acac})_2$ as precursor salts. All measurements were carried out at room temperature. The corresponding results are summarized in Table 4.2. The coercivity values varied between 101 Oe and 158 Oe for the samples produced from $\text{Co}(\text{ac})_2$ solutions. Higher coercivity values, in the range 200 Oe-225 Oe, were measured for the samples synthesized by using the $\text{Co}(\text{acac})_2$ salt. The higher coercivities obtained in the latter samples is attributed to the presence of the hcp-Co phase, which was present in a larger proportion when the $\text{Co}(\text{acac})_2$ was used as the precursor salt. In turn, lower coercivity values were attained for the samples where the soft magnetic fcc-Co phase was the predominant one. The corresponding saturation magnetization values, M_s , ranged between 83-110 emu/g and 80-90 emu/g for the samples synthesized from the acetate and the acetylacetonate precursor salts, respectively. On the above basis, the strong effect of both is clear, the OH^-/Co mole ratio and the type of cobalt precursor on the stability of the cobalt phases and, consequently on the corresponding magnetic properties. For the first factor, it is evident the catalytic effect of the OH^- ions on the metal-forming reaction. The formation of well-crystallized cobalt phases was promoted by higher 'R' values. The OH^- ions could have accelerated the dissolution of the intermediate, which in turn accelerated the formation of the metallic phase. Based on the obtained information, the dissolution of the intermediate under alkaline conditions was faster when a less crystalline intermediate was formed. The

acceleration of the metal-forming reaction should also account for the formation of metastable hcp- and ϵ -Co structures.

Accordingly, the following part of our research work was focused on the evaluation of different options to accelerate the metal formation even more. For this purpose, the effect of the concentration of Co ions, keeping constant the total volume of reaction, and the use of Pt ions as nucleating and/or alloying components, have been evaluated. CoPt alloy is a good candidate for data storage applications as shown in the Table 2.5.

TABLE 4.2: Reported values of magnetic properties for cobalt particles as synthesized using SQUID at 300 K.

R	Coercivity (Oe)		Magnetization of remanence (emu/g)		Magnetization of saturation (emu/g)	
	Metallic salt		Metallic salt		Metallic salt	
	Co(ac) ₂	Co(acac) ₂	Co(ac) ₂	Co(acac) ₂	Co(ac) ₂	Co(acac) ₂
30	150	225	6	13	110	80
40	101	200	5	10	107	90
50	168	211	6	8	83	84

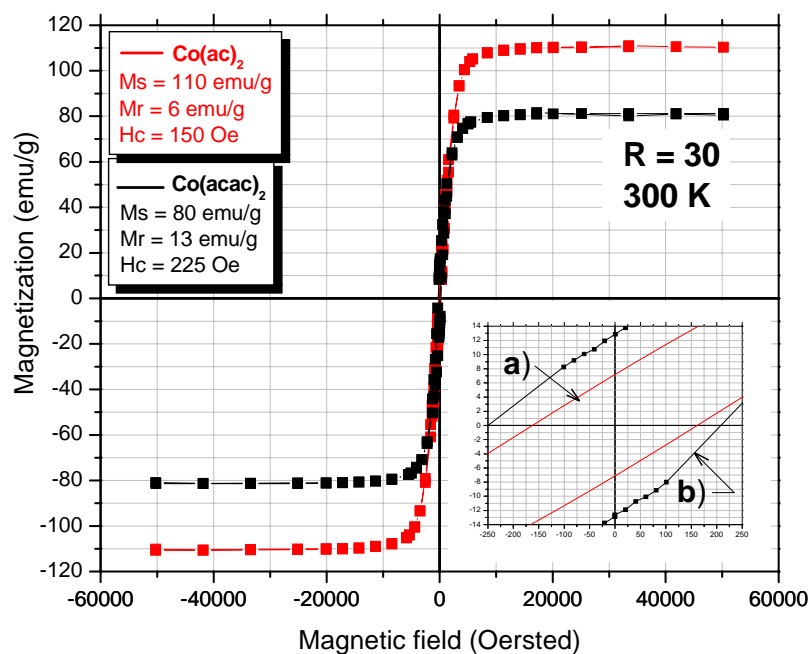


Figure 4.27: M-H loops for Co powders synthesized from 0.01M Co(ac)₂, 'a', or 0.01M Co(acac)₂, 'b', solutions. The insert show the M-H loop around the origin.

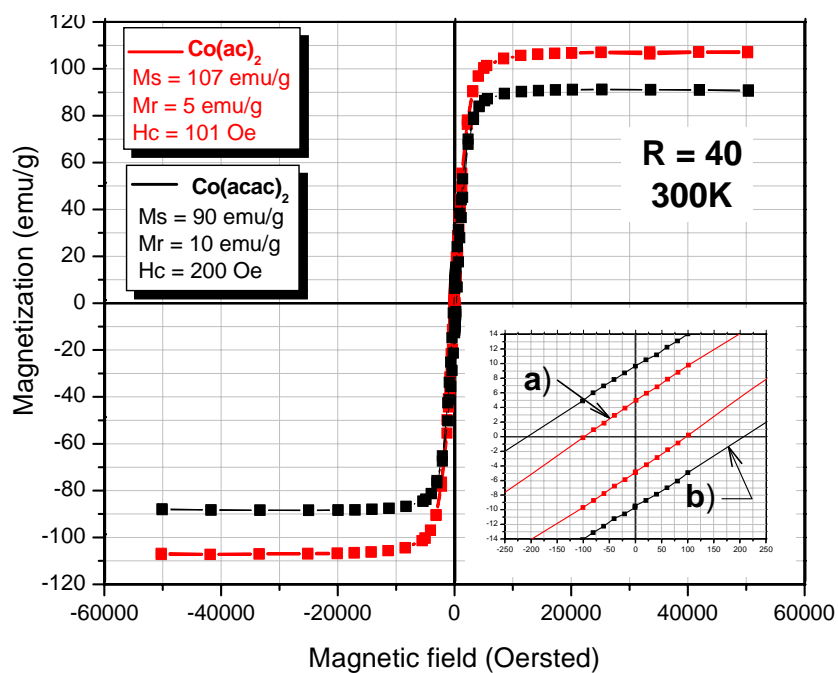


Figure 4.28: M-H loops for Co powders synthesized from 0.01M Co(ac)₂, 'a', or 0.01M Co(acac)₂, 'b', solutions. The insert show the M-H loop around the origin.

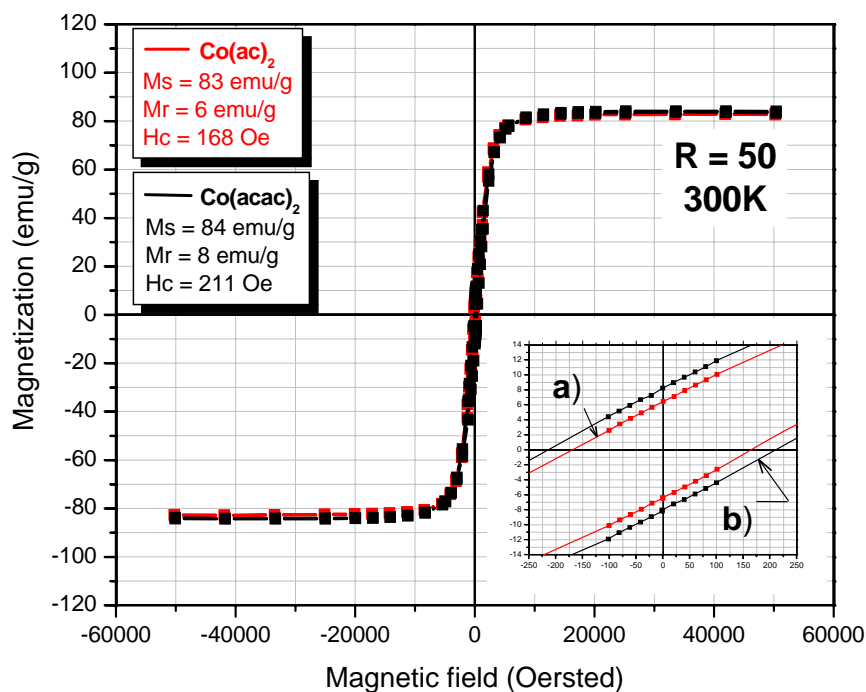


Figure 4.29: M-H loops for Co powders synthesized from 0.01M $\text{Co}(\text{ac})_2$, 'a', or 0.01M $\text{Co}(\text{acac})_2$, 'b', solutions. The insert show the M-H loop around the origin.

4.3 Effect of the concentration of Co ions

In order to evaluate the possibility of accelerating the reduction reaction by increasing the ratio of reducing agent to cobalt ions, reduction tests were carried out at different Co concentrations in TMEG at a constant reaction volume of 320 ml and 4 hours of reaction.

4.3.1 Structural characterization

XRD patterns of Figure 4.30 correspond to the solids synthesized at 0.005 M Co, $R = 50$ and using $\text{Co}(\text{ac})_2$ or $\text{Co}(\text{acac})_2$ as precursor salts. As seen, a mixture of fcc-, hcp- and ϵ -Co phases were observed when $\text{Co}(\text{ac})_2$ was used. The estimated lattice parameter for the

fcc-Co structure, $a=3.581 \text{ \AA}$, is larger than the value reported in reference [9], $a=3.545 \text{ \AA}$. The discrepancy could be attributed to the lack of precision in estimating the diffraction angles from the noisy signal of the corresponding XRD pattern. Although to a lesser extent, the presence of cobalt oxides was also detected. These oxides could have been formed due to atmospheric oxidation during the prolonged XRD measurement times (close to 12 hours). On the other hand, only metastable ϵ -Co was obtained from starting $\text{Co}(\text{acac})_2$ solutions. The well defined and sharp XRD peaks of the ϵ -Co phase suggest its high crystallinity. Similar metallic and oxide phases were detected when the reduction experiments were carried out at a Co concentration as low as 0.0025M. To our current knowledge, the formation of the epsilon-Co phase in TMEG is reported here for the first time. The corresponding lattice parameter for ϵ -Co was $a = 6.219 \text{ \AA}$. This value is slightly higher than the lattice parameter of $a = 6.097 \text{ \AA}$, reported by Dmitry et al. [10].

Figure 4.31 shows the XRD patterns for the solids synthesized from 0.0025 M Co solutions. The co-existence of hcp- and fcc-Co phases were observed when the solids were synthesized from $\text{Co}(\text{ac})_2$ solutions. Unlike the solid produced at 0.005M, the ϵ -Co phase was not the predominant one. It is apparent that the fcc-Co phase was present in a major proportion than the hcp-Co. The predominance of the hcp-Co phase could have been caused by the enhanced rate of the reduction reaction, promoted by the larger availability of the reducing agent, the TMEG, when lower concentration of cobalt ions were considered. The acceleration in the formation of the cobalt phases would have inhibited the stability of the ϵ -Co, favoring instead the formation of hcp-Co. The hexagonal Co-phase is also considered metastable for nanocrystalline systems [11]. The

noise in the XRD signal avoids the precise calculations of the corresponding lattice parameters. On the other hand, only well defined and sharp XRD peaks corresponding to metastable ϵ -Co were observed when the solids were synthesized from starting 0.005 M and 0.0025 M Co(acac)₂ solutions.

Since all samples were obtained after quenching of the reactant solution in an ice-bath, we wanted to know the effect of micro strains generated by residual stress on the structure of the ϵ -Co solids. For this reason, the XRD data corresponding to ϵ -Co produced from 0.005 M and 0.0025 M Co(acac)₂ solutions were treated by the Williamson-Hall's (W-H) approach [35]. The details and fundamentals of this approach have been presented in section 2.4 of this thesis. The corresponding data are shown in Tables 4.3 and 4.4 and Figures 4.32-33. For comparison purposes, the average crystallite size estimated by Scherrer's equation was also included. The average crystallite size for the ϵ -Co produced from 0.005M Co solutions (Figure 4.30 b) was estimated at 13.4 nm using the Scherrer's equation. This value was 16.6 nm when the W-H analysis was used. The corresponding strain was estimated at 0.1%. This strain could have been caused by the residual stresses in the crystal generated by the ice-quenching of the solids at the end of the reaction time. The corresponding lattice parameter was $a = 6.226 \text{ \AA}$, which is somehow larger than the lattice parameter reported by Dmitry and Bawendi [10], $a = 6.097 \text{ \AA}$, for ϵ -Co synthesized by the thermal decomposition of carbonyl species. This discrepancy could be due to the establishment of a uniform strain in the quenched crystals. This uniform strain may have provoked the increase in the interplanar distance and hence, the increase in the unit cell dimensions. The average crystallite size for the solids

produced from 0.0025 M Co solutions was estimated at 14.2 nm and 16.4 nm by using the Scherrer's and the W-H approaches, respectively. The corresponding strain was 0.05%. The average crystallite size computed using the W-H approach is larger than the value estimated by the Scherrer's equation. It was expected, since the Scherrer's equation does not take into account the effect of generated micro-strain on the broadening of XRD peaks.

On the above basis, the synthesis of metastable ϵ -Co became possible through a careful control of the synthesis conditions. The presence of OH⁻ ions, the type of cobalt precursor salt and the abrupt cooling of the solids (quenching) were the most important factors conducive to the development of this nanocrystalline structure.

TABLE 4.3: Comparison of the lattice parameter and crystallite size of as-synthesized ϵ -Co powders from 0.005 M Co solutions using $\text{Co}(\text{acac})_2$ precursor, TMEG at 487 ± 5 K.

Williamson Hall						Scherrer's equation	Bragg's law		ϵ -Co reported by Dmitry et al. [33] using Bragg's law			
Peak			2 θ (Degrees)	FWHM = B (Degrees)	B*cos(θ)	sin(θ)	t (nm)	d (Å)	a (Å)	2 θ (Degrees)	d (Å)	a (Å)
h	k	l										
2	2	1	43.65	0.6982	0.0113	0.3718	12.95	2.0735	6.221	44.57	2.0329	6.099
3	1	0	46.06	0.5982	0.0096	0.3912	15.24	1.9707	6.232	47.14	1.9279	6.096
3	1	1	48.51	0.7306	0.0116	0.4108	12.60	1.8765	6.224	49.59	1.8382	6.097
3	2	1	55.12	0.6826	0.0106	0.4627	13.87	1.6662	6.234	Non reported		
5	1	0	78.40	0.8691	0.0118	0.6320	12.46	1.2197	6.219	80.30	1.1956	6.096
							13.42*		6.226*			6.097*

* Average

TABLE 4.4: Comparison of the lattice parameter and crystallite size of as-synthesized ϵ -Co powders from 0.0025 M Co solutions using $\text{Co}(\text{acac})_2$ precursor, TMEG at 487 ± 5 K.

Williamson Hall						Scherrer's equation	Bragg law		ϵ -Co reported by Dmitry et al. [33] using Bragg's law			
Peak			2 θ (Degrees)	FWHM = B (Degrees)	B*cos(θ)	sin(θ)	t (nm)	d (Å)	a (Å)	2 θ (Degrees)	d (Å)	a (Å)
h	k	l										
2	2	1	43.66	0.6284	0.0102	0.3719	14.39	2.0730	6.219	44.57	2.0329	6.099
3	1	0	46.12	0.6558	0.0105	0.3917	13.91	1.9682	6.224	47.14	1.9279	6.096
3	1	1	48.58	0.6278	0.0100	0.4114	14.67	1.8740	6.215	49.59	1.8382	6.097
3	2	1	55.28	0.6480	0.0100	0.4639	14.62	1.6618	6.218	Non reported		
5	1	0	78.42	0.7942	0.0107	0.6322	13.64	1.2195	6.218	80.30	1.1956	6.096
							14.24*		6.219*			6.097*

* Average

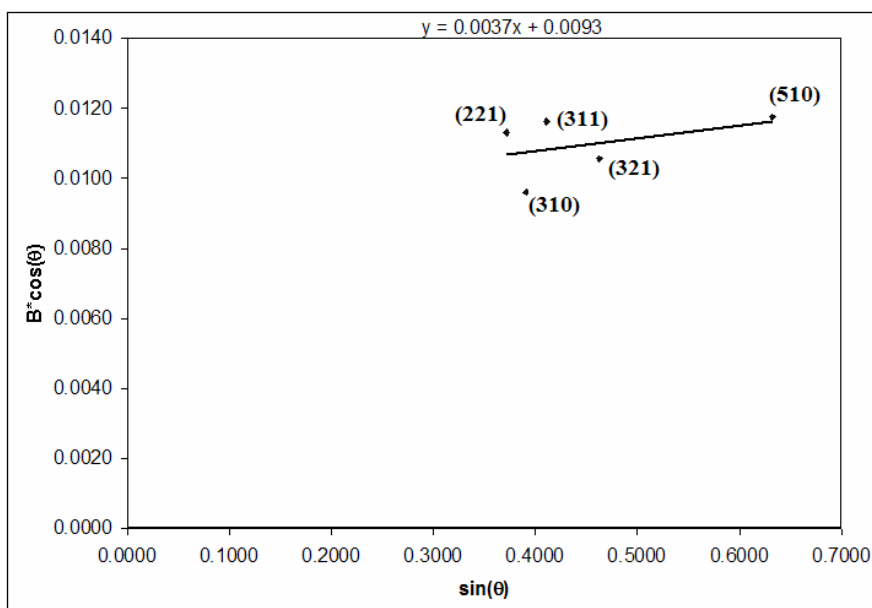


Figure 4.32: Williamson Hall's plot for ϵ -Co sample for 0.005 M Co particles synthesized from $\text{Co}(\text{acac})_2$, TMEG at 487 ± 5 K. The reaction time was 4 hours and 'R' of 50.

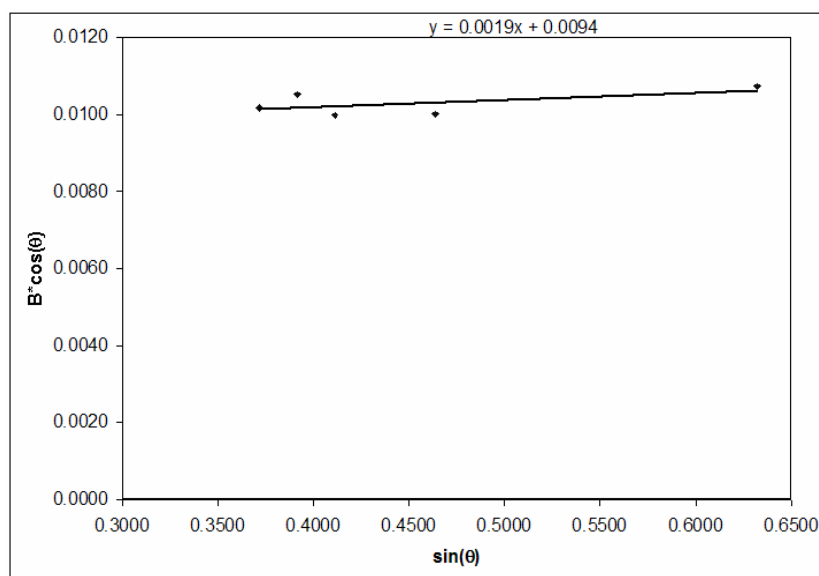


Figure 4.33: Williamson Hall's plot for ϵ -Co sample for 0.0025 M Co particles synthesized from $\text{Co}(\text{acac})_2$, TMEG at 487 ± 5 K. The reaction time was 4 hours and 'R' of 50.

4.3.2 Magnetic characterization

Figure 4.34 shows the corresponding M-H measurements at room-temperature for metastable ϵ -cobalt precipitates synthesized from 0.0025M $\text{Co}(\text{acac})_2$ solutions in TMEG and $R = 50$. In Figure 4.35, the coercivity (H_c) value was 80 Oe, which is below the 211 Oe observed for the ϵ -fcc/hcp-Co mixture produced from 0.01M Co solutions (Section 4.2.3). The low coercivity of ϵ -Co could be expected for a soft magnetic material [37] whereas, the presence of hcp-Co would have accounted for the higher coercivity in the sample produced at 0.01M Co. In turn, the M_s values for the solids produced at 0.01M Co and 0.0025M Co were 84 and 97 emu/g, respectively. The difference in magnetization is attributed to the predominance of the soft magnetic ϵ -Co phase in the sample produced at the lowest Co concentration.

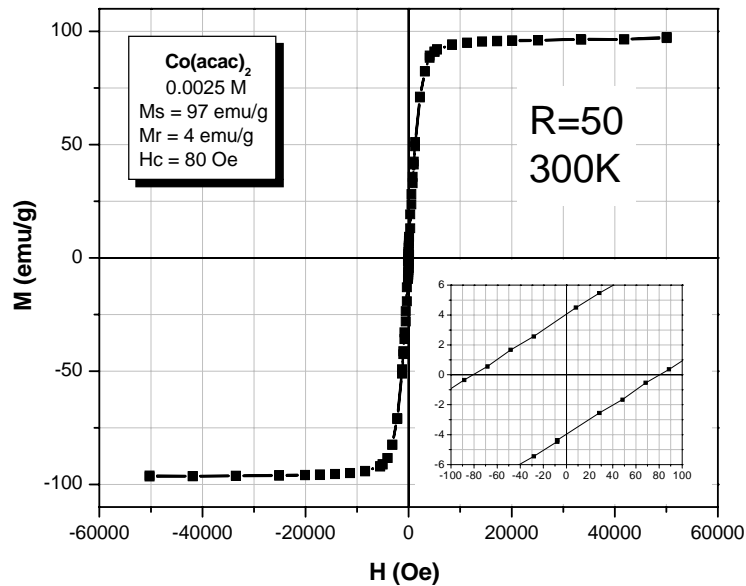


Figure 4.34: M-H loop for ϵ -Co powder synthesized from 0.0025 M $\text{Co}(\text{acac})_2$ in TMEG at 487 ± 5 K. The insert show the M-H loop around the origin.

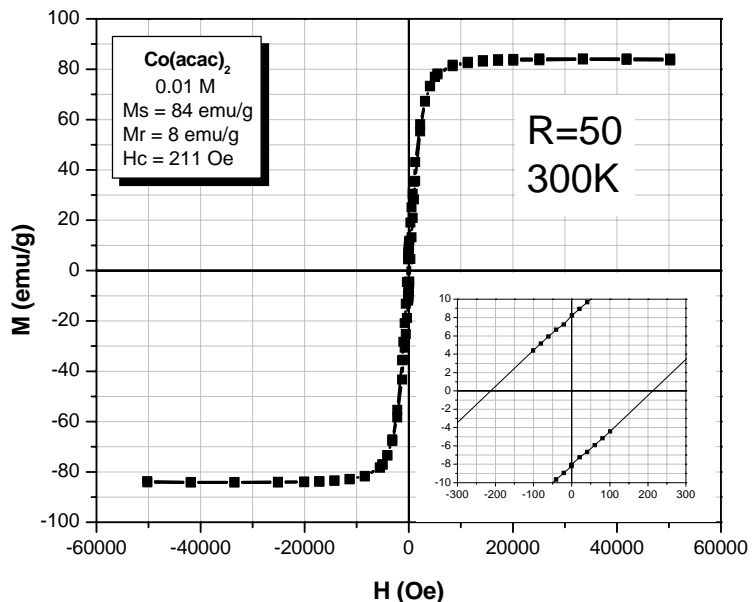


Figure 4.35: M-H loop for ϵ -Co powder synthesized from 0.01 M $\text{Co}(\text{acac})_2$ in TMEG at 487 ± 5 K. The insert show the M-H loop around the origin.

4.4 Effect of the Co-existence of Pt ions in starting solutions

So far, our work has demonstrated that it is possible to stabilize metastable Co structures such as hcp- or ϵ -Co at room temperature. Accordingly, the following experiments were designed in order to evaluate the effect of co-existing Pt ions not only as pre-nucleating agents, which would accelerate the formation of the magnetic phase, but also as alloying elements to explore the possibility of forming CoPt nanostructures. Accordingly, two sources of platinum ions were used. Nucleation rate would be enhanced by using highly

reducible hexa-chloro-platinate salt. On the contrary, the probable formation of CoPt alloys could become viable by using less-reducible Pt salts such as acetylacetonate.

4.4.1 Hexachloro-platinate as source of platinum ions

i) Structural characterization

The promoting effect of Pt ions on the formation of cobalt precipitates in EG has been verified experimentally [38-36]. Accordingly, precipitation tests were undertaken by varying the Pt/Co mole ratio in starting solutions between 0.15 and 1.0 but in the presence of TMEG. The OH/Co mole ratio was 50 in all these experiments. Also in our system, the presence of Pt ions accelerated the cobalt formation dramatically; the magnetic phase was detected after one minute of reaction, instead of the 4 hours required in its absence. The co-existence of ϵ - with hcp-Co (Figure 4.36), was suggested by the results of the XRD analyses of samples produced at $R = 50$, 10 minutes of reaction and a mole ratio Pt/Co of 0.15. The excess of Pt, i.e., Pt ions that were reduced at the earlier reaction times, was present as fcc-Pt. The most remarkable result was the presence of (110), (111), and (112) XRD peaks that correspond to ferromagnetic ordered fct-CoPt phase. To the best of our knowledge, this is the first report describing the direct formation –i.e., with no need for any thermal treatment- of fct-CoPt alloy at such low temperature as 487 K, after an extremely short reaction time, and with no need of annealing. Apparently, the reduction of cobalt was so accelerated that part of it could be alloyed with Pt during the solid formation process. The lattice parameters for hcp-Co and fct-

CoPt were estimated as $a = 2.46 \text{ \AA}$ and $c = 4.03 \text{ \AA}$ and $a = 3.748 \text{ \AA}$ and $c = 3.753 \text{ \AA}$, respectively.

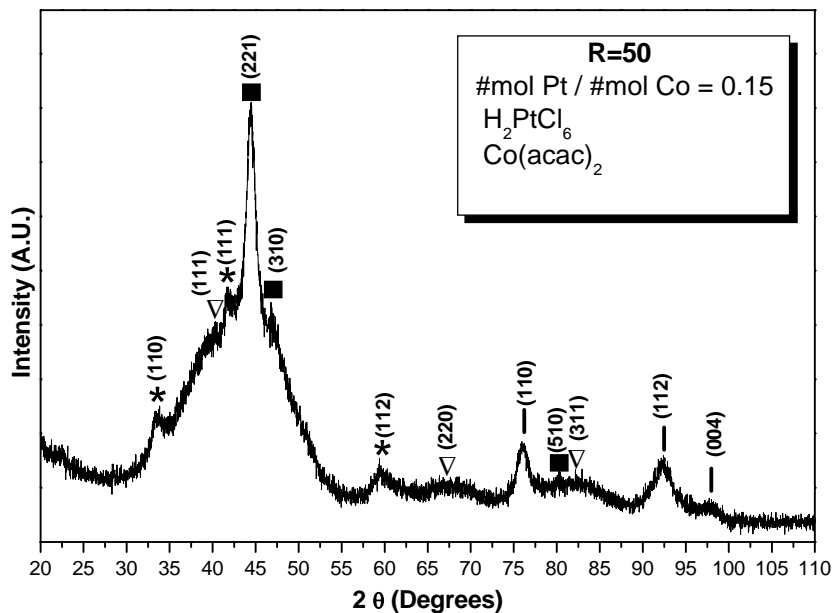


Figure 4.36: XRD pattern of as-synthesized Co particles at 'R'= 50, a Pt/Co mole ratio of 0.15 in TMEG at $487 \pm 5 \text{ K}$. XRD analysis revealed the coexistence of hcp (|), ϵ (■); fcc-Pt (▽) and ordered fct-CoPt (*).

In order to explore the possibility of accelerating the reduction reaction further, and enhance the amount of the fct-CoPt phase, additional tests were carried out at Pt/Co mole ratio values as high as 0.25 and 1.0. The XRD patterns corresponding to solids precipitated after 10 minutes of reaction are shown in Figures 4.36 y 4.37. Produced solids were not as magnetic as the one produced at a Pt/Co mole ratio of 0.15. The XRD analyses evidenced that only Pt ions were reduced. No peaks corresponding to isolated Co or CoPt phases were detected. Produced Pt nanoparticles exhibited an average crystallite size of 1.5 nm and lattice parameter of $a = 3.913 \text{ \AA}$, which is good agreement with the data given at PDF # 04 0802 [13].

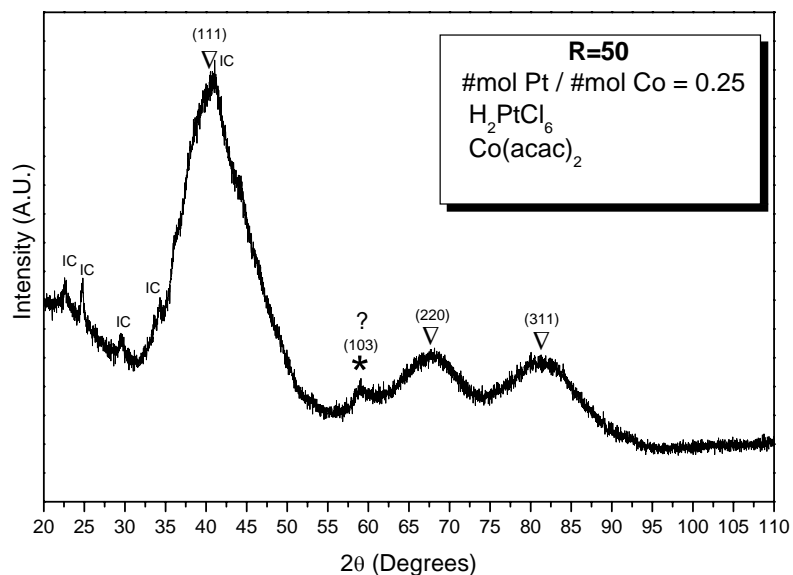


Figure 4.37 XRD pattern of as-synthesized Co particles at ‘R’= 50, a Pt/Co mole ratio of 0.25 in TMEG at 487 ± 5 K. XRD analysis revealed the coexistence of fcc-Pt (∇) and ordered fct-CoPt (*). Sharp peaks are from the residual intermediate compound (IC).

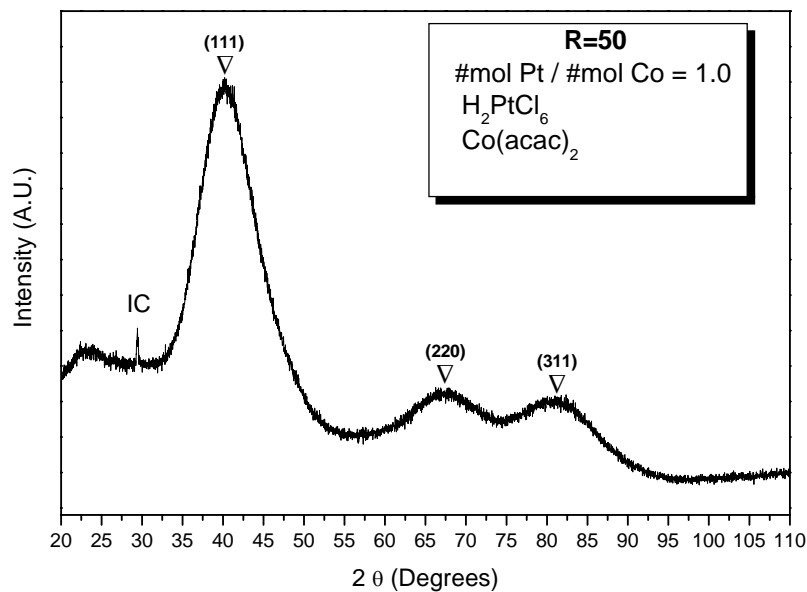


Figure 4.38: XRD pattern of as-synthesized Co particles at ‘R’= 50, a Pt/Co mole ratio of 1.0 in TMEG at 487 ± 5 K. XRD analysis revealed only fcc-Pt (∇). Sharp peaks are from the residual intermediate compound (IC).

ii) Morphological analyses

As Figure 4.39 shows, the metallic precipitates produced at a Pt/Co mole ratio of 0.15 consisted of tiny particles in the sub-micrometric range. The extremely small size of the precipitates is attributed to the enhancement of the nucleation rate by the presence of pre-existent platinum nuclei generated under kinetically enhanced precipitation conditions. The solids produced at higher Pt/Co mole ratios (Figures 4.40-41) consisted of tiny and irregular sub-micrometric particles of elemental Pt, as suggested by XRD analyses. The large and irregular islands, particularly visible in Figure 4.41, can be attributed to a residual intermediate that was not fully converted into the metallic phase.

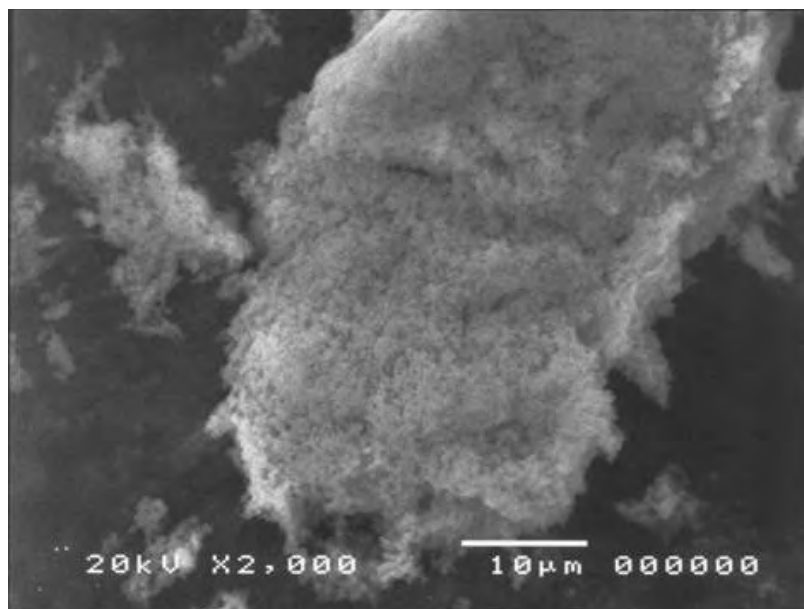


Figure 4.39: SEM image of cobalt, platinum and cobalt platinum particles as-synthesized at 'R'= 50, 0.0025 M Co(acac)₂, a Pt/Co mole ratio of 0.15 in TMEG at 487±5 K.

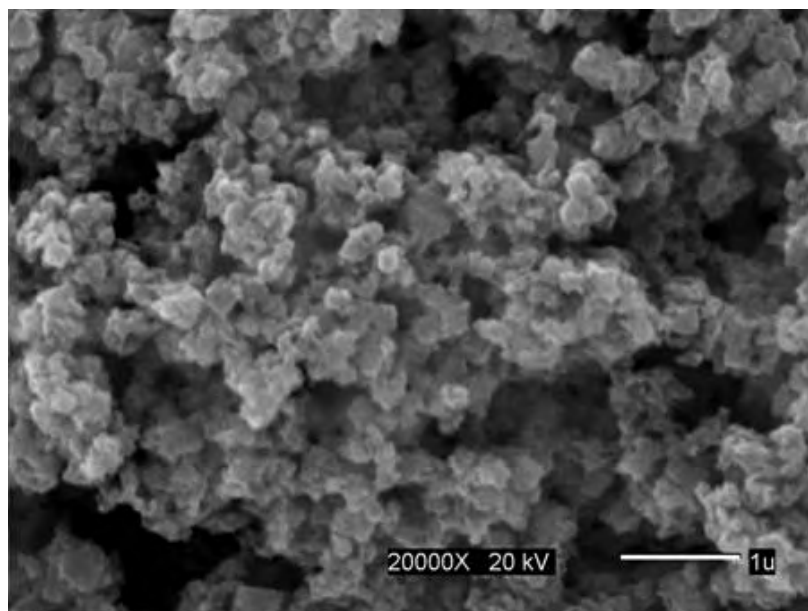


Figure 4.40: SEM image of platinum and cobalt platinum particles as-synthesized at 'R' = 50, 0.0015 M Co(acac)₂, a Pt/Co mole ratio of 0.25 in TMEG at 487±5 K.

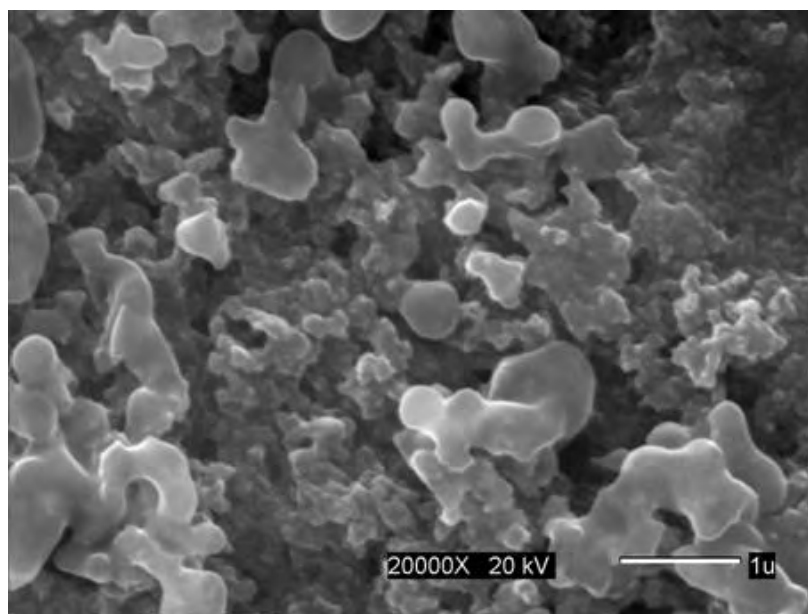


Figure 4.41: SEM image of platinum particles as-synthesized at 'R' = 50, 0.0005 M Co(acac)₂, a Pt/Co mole ratio of 1.0 in TMEG at 487±5 K.

iii) Magnetic characterization

Figure 4.42, 4.43 and 4.44 show the M-H hysteresis loops for the solids produced at Pt/Co mole ratios of 0.15, 0.25 and 1.0. The initial Co concentration was 0.0025 M and $R = 50$. The reaction time was 10 minutes. The M_s values varied from 71 to 10 emu/g when the Pt/Co mole ratio was increased from 0.15 to 0.25. The corresponding coercivity values ranged between 248 and 188 Oe. The decrease in M_s and H_c values with a rising Pt/Co mole ratio is attributed to the increase in the amount of diamagnetic Pt that was reduced independently from the cobalt ions. The highest H_c value of 248 Oe can be explained by the co-existence of hcp-Co phase and the fct-CoPt structure [38-36]. These phases were identified in our XRD analyses. It is interesting to note that the M-H loop for the solid produced at a Pt/Co ratio of 0.25 was not saturated. This can be explained by the presence of superparamagnetic particles of Co and/or CoPt phases. The M-H loop for the solids produced at a Pt/Co mole ratio of 1.0 is shown in Figure 4.44. Although the variation in the magnetization with applied magnetic field is typical of a diamagnetic material, this could be due to sample holder background; the development of a loop at small magnetic fields may suggest the co-existence of a ferromagnetic phase. The corresponding coercivity was as high as 217 Oe. Nevertheless, the moderate coercivity may suggest the formation of high-coercivity CoPt phase at an amount so low to be detected by XRD analyses.

Although the viability in forming an alloy of CoPt has been demonstrated, the excess of Pt ions would precipitate as diamagnetic and isolated elemental Pt. Then, to improve the

conditions to form the CoPt alloy, the early reduction of Pt ions should be somehow inhibited. For this purpose, less reducible Pt-acetylacetonate was tested as the source of Pt ions. The stability of the acetylacetonate complex is higher than the chloride one. Therefore, the release of Pt ions from the acetylacetonate compound will be limited. The limited availability of the Pt ions could promote the simultaneous precipitation with Co ions, and hence, favoring the formation of the CoPt alloy.

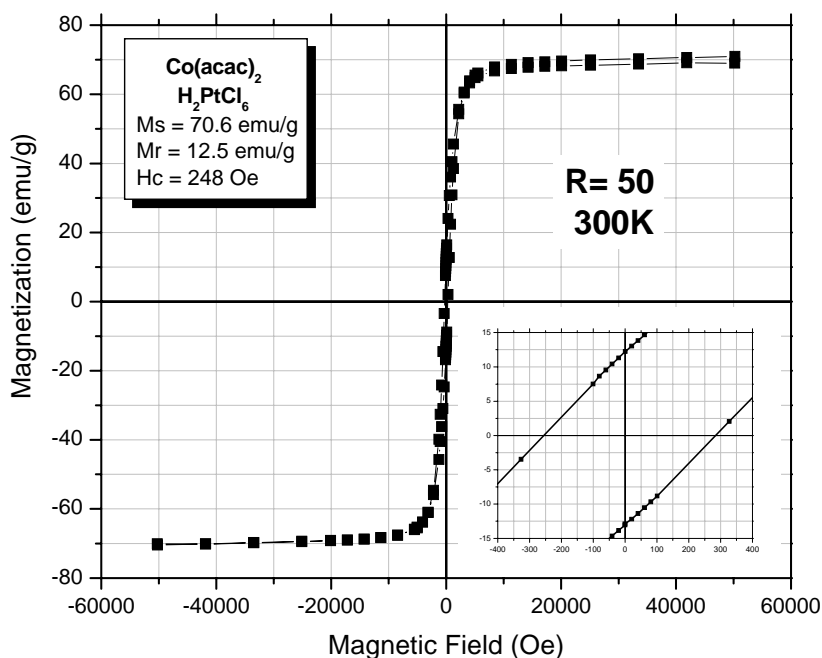


Figure 4.42: M-H loop for cobalt, platinum and cobalt platinum particles synthesized at 0.0025 M $\text{Co}(\text{acac})_2$ and a Pt/Co mole ratio of 0.15 in TMEG at 487 ± 5 K. The insert show the M-H loop around the origin.

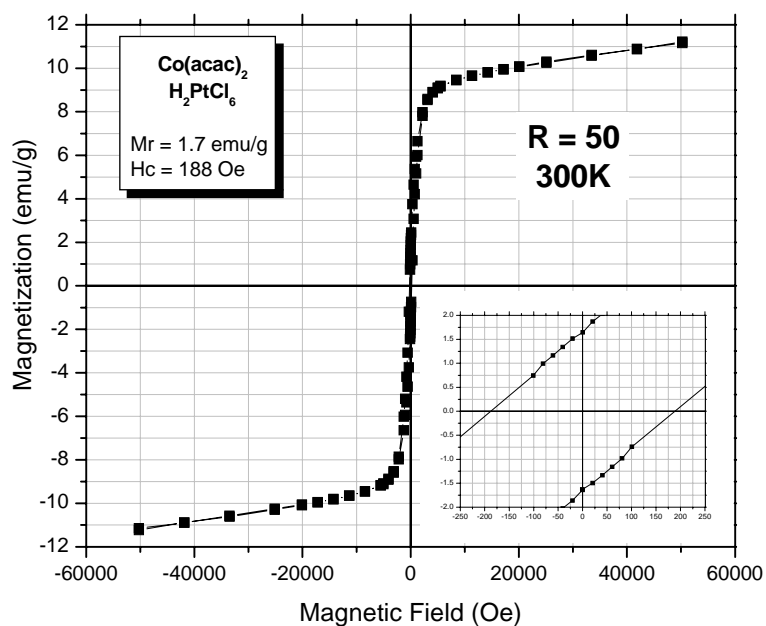


Figure 4.43: M-H loop for cobalt, platinum and cobalt platinum particles synthesized at 0.0015 M $\text{Co}(\text{acac})_2$ and a Pt/Co mole ratio of 0.25 in TMEG at 487 ± 5 K. The insert show the M-H loop around the origin.

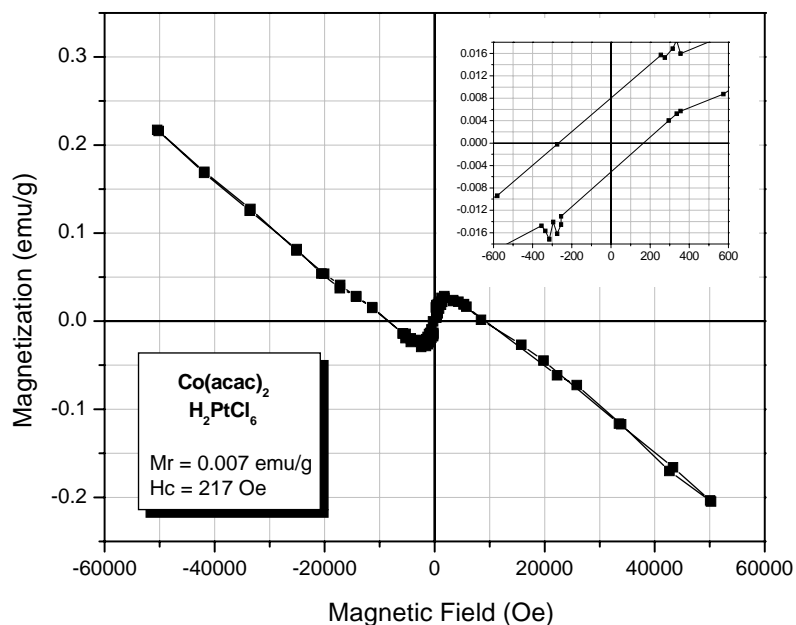


Figure 4.44: M-H loop for cobalt, platinum and cobalt platinum particles synthesized at 0.0005 M $\text{Co}(\text{acac})_2$ and a Pt/Co mole ratio of 1.0 in TMEG at 487 ± 5 K. The insert show the M-H loop around the origin.

4.4.2 Platinum acetyl-acetonate as source of platinum ions

i) Structural characterization

In the following experiments, Pt-acetylacetonate was evaluated as the source of Pt ions. Other synthesis conditions were determined based on our previous work. Accordingly, the concentration of the Co TMEG solution was 0.0025M and $R = 50$. The Pt/Co mole ratios were 0.15 and 1.0. Samples were withdrawn after 10 minutes, 1 hour, and 4 hours of reaction. Figure 4.45 shows the XRD pattern for the solid produced at a Pt/Co mole ratio 0.15 and after a reaction time as short as 10 minutes. Only XRD peaks corresponding to the fct-CoPt phase were observed. Moreover, the peak broadening suggests the nanocrystalline nature of the solids. The lattice parameters using (111) and (200) peaks were $a = 3.777 \text{ \AA}$ and $c = 3.571 \text{ \AA}$, which are smaller than their bulk values ($a = 3.803 \text{ \AA}$ and $c = 3.701 \text{ \AA}$, PDF # 43 1358). The superposition of the peaks as shown in the Figure 4.46 did permit the use of Williamson Hall analyses that could have provided information about micro-strains provoked by residual stresses during crystal formation and growth. The presence of micro-strains can explain minor shifts in the angular positions of the XRD peaks, and hence, the observed discrepancies between the lattice dimensions of the nanocrystals and the bulk. The crystallite size using Scherrer's equation was 2.81 nm. This value is below the superparamagnetic limit for $\text{Co}_{50}\text{Pt}_{50}$, which is 4nm [39]. Fct-CoPt has been obtained from fcc-CoPt only after thermal treatment involving annealing for 50 hours at 953 K [40], after 0.5 hours at 973 K [18], or from fcc-CoPt nanoparticles after one hour of heating under reducing conditions at 823 K

[31]. To our current knowledge, the direct formation of nanocrystalline fct-CoPt phase is reported here for the first time. Evidently, an elemental analysis (EDX, EDS or EPMA) will provide additional information on the chemical composition of the alloy.

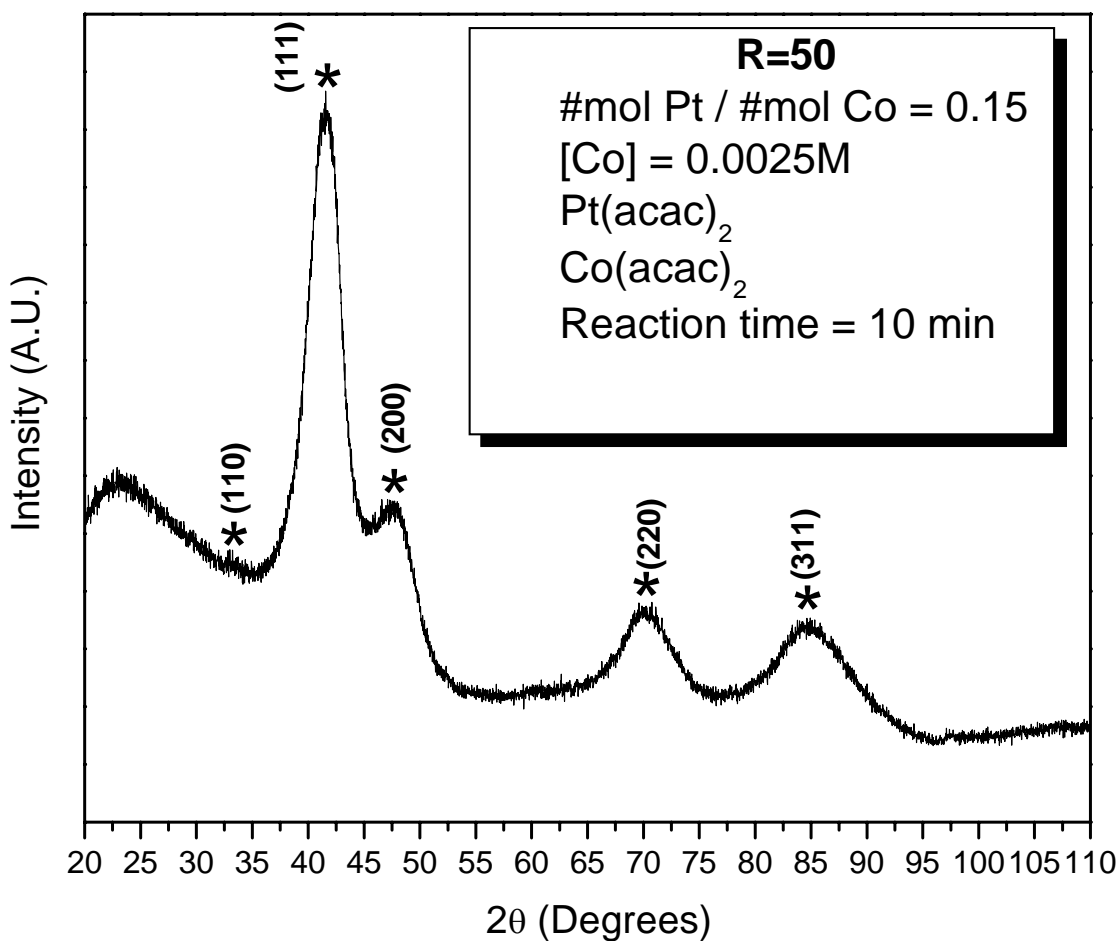


Figure 4.45: XRD pattern of as-synthesized CoPt particles in TMEG at 487 ± 5 K with 'R' = 50 and a Pt/Co mole ratio of 0.15. XRD analysis revealed only nanocrystalline fct-CoPt (*).

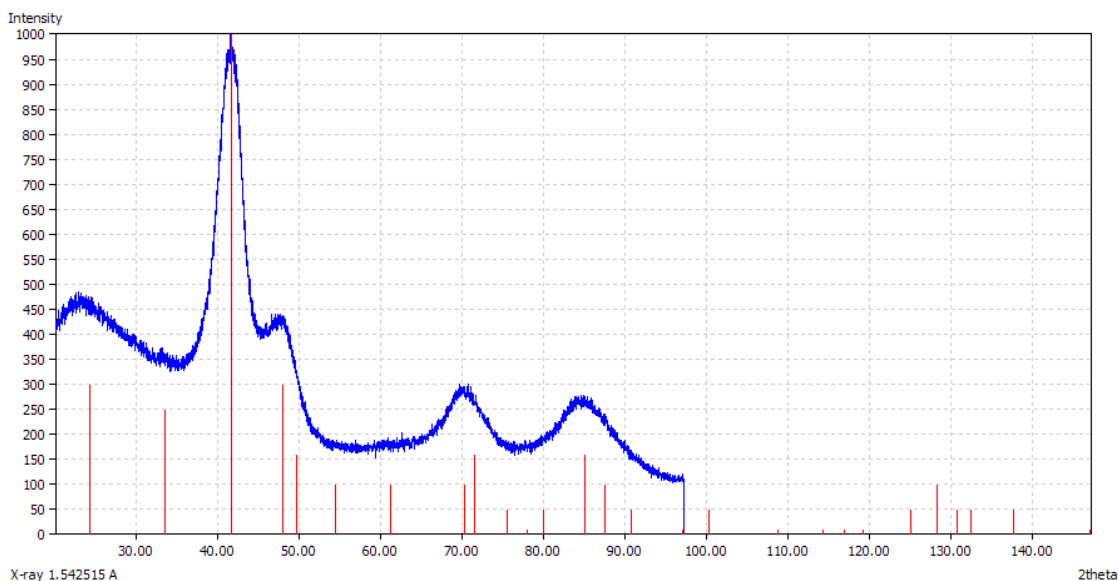


Figure 4.46: XRD pattern match with PDF # 29 0498 using the software phase identification from powder diffraction MATCH v 1.7 of as-synthesized CoPt particles in TMEG at 487 ± 5 K with 'R' = 50 and a Pt/Co mole ratio of 0.15. XRD analysis revealed only nanocrystalline fct-CoPt.

Figure 4.47 shows XRD patterns of the solids produced at a Pt/Co mole ratio of 1 and 10 minutes of reaction. As seen, the fct-CoPt phase was formed again, but co-existing with elemental Platinum. The sharpening of the Pt peaks suggests a high crystallinity whereas the broad fct-CoPt peaks may suggest the formation of nanocrystalline precipitates. The average cubic Pt-lattice parameter was 3.928 \AA , which agrees well with the value of 3.923 \AA reported for the bulk (PDF # 04 0802).

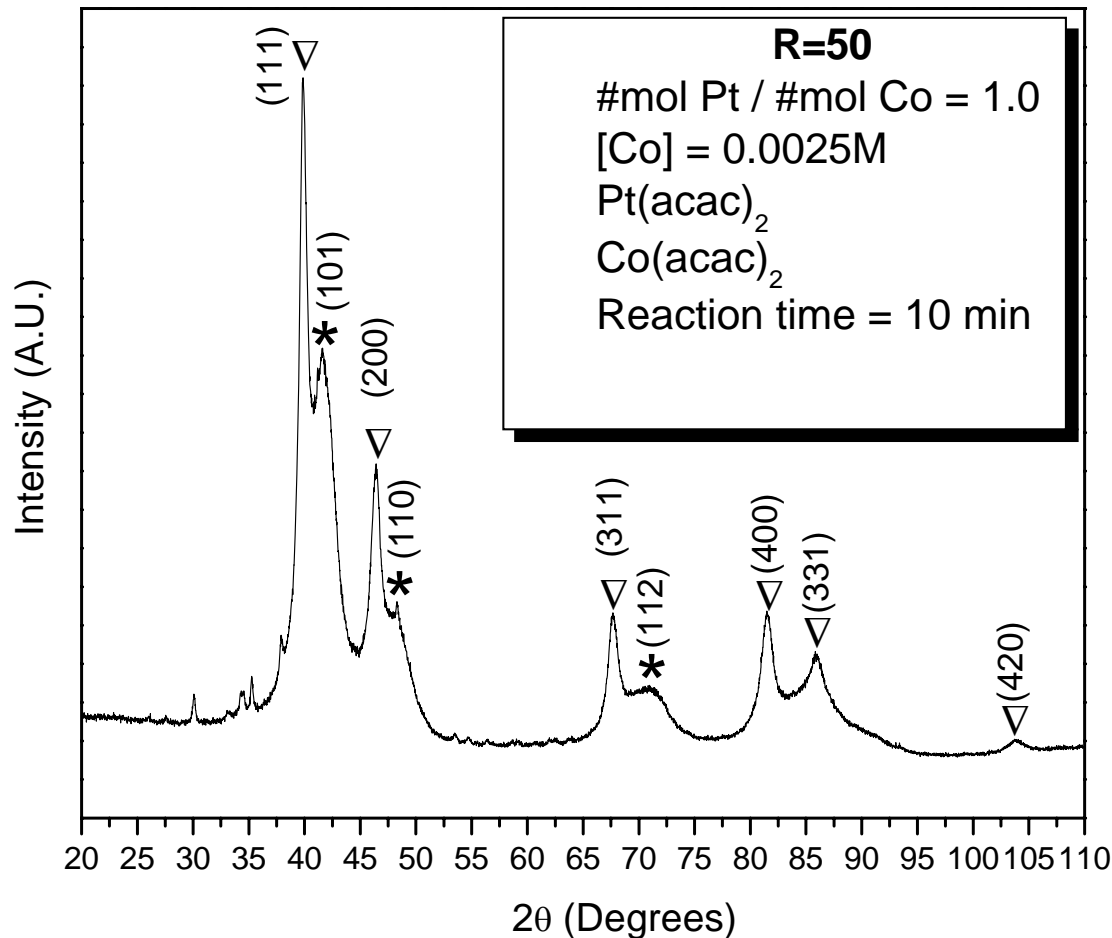


Figure 4.47: XRD pattern of as-synthesized Pt and CoPt particles at ‘R’= 50 and a Pt/Co mole ratio of 1.0 in TMEG at 487 ± 5 K. XRD analysis revealed the coexistence of fcc-Pt (∇) and ordered fct-CoPt (*). Non-assigned small peaks are attributed to residual intermediate (IC).

In order to obtain additional information about the formation of the metallic phases as a function of reaction time, samples produced after 1 hour and 4 hours of reaction were analyzed by XRD. Figure 4.48 summarizes the obtained results. As seen, there is much change in the stability of the fct-Co phase when the synthesis considered a Pt/Co mole ratio of 0.15. The peaks were somehow sharper when the reaction time was increased.

This may indicate further growth of the crystal after prolonged times. The lattice parameters for the fct-CoPt produced after 1 hour of reaction were estimated at $a = 3.770 \text{ \AA}$ and $c = 3.616 \text{ \AA}$, which are in reasonable agreement with the bulk values (PDF # 43 1358). The lattice parameters were $a = 3.663 \text{ \AA}$ and $c = 3.751 \text{ \AA}$ for the solids produced after 4 hours of reaction. As mentioned above, the presence of micro-strains can explain the minor shifts in the XRD peaks, and hence, the observed discrepancies between the lattice dimensions of the nanocrystals and the bulk. Since most of the XRD peaks are overlapped in the nanocrystalline solids, the W-H analysis can not be applied in this case. The XRD patterns for the solids produced at a Pt/Co mole ratio of 1.0 and different reaction times are shown in Figure 4.49. Only elemental Pt and fct-CoPt phases were identified. Minor peaks of the intermediate compound were observed in the sample produced after 10 minutes of reaction. It suggests the intermediate compound was not fully converted into the metal phases at this reaction time. The absence of those minor peaks after prolonged reaction times support this statement. The most remarkable feature could be the sharpening in the XRD peaks of Pt, which suggest crystal growth under prolonged reaction times.

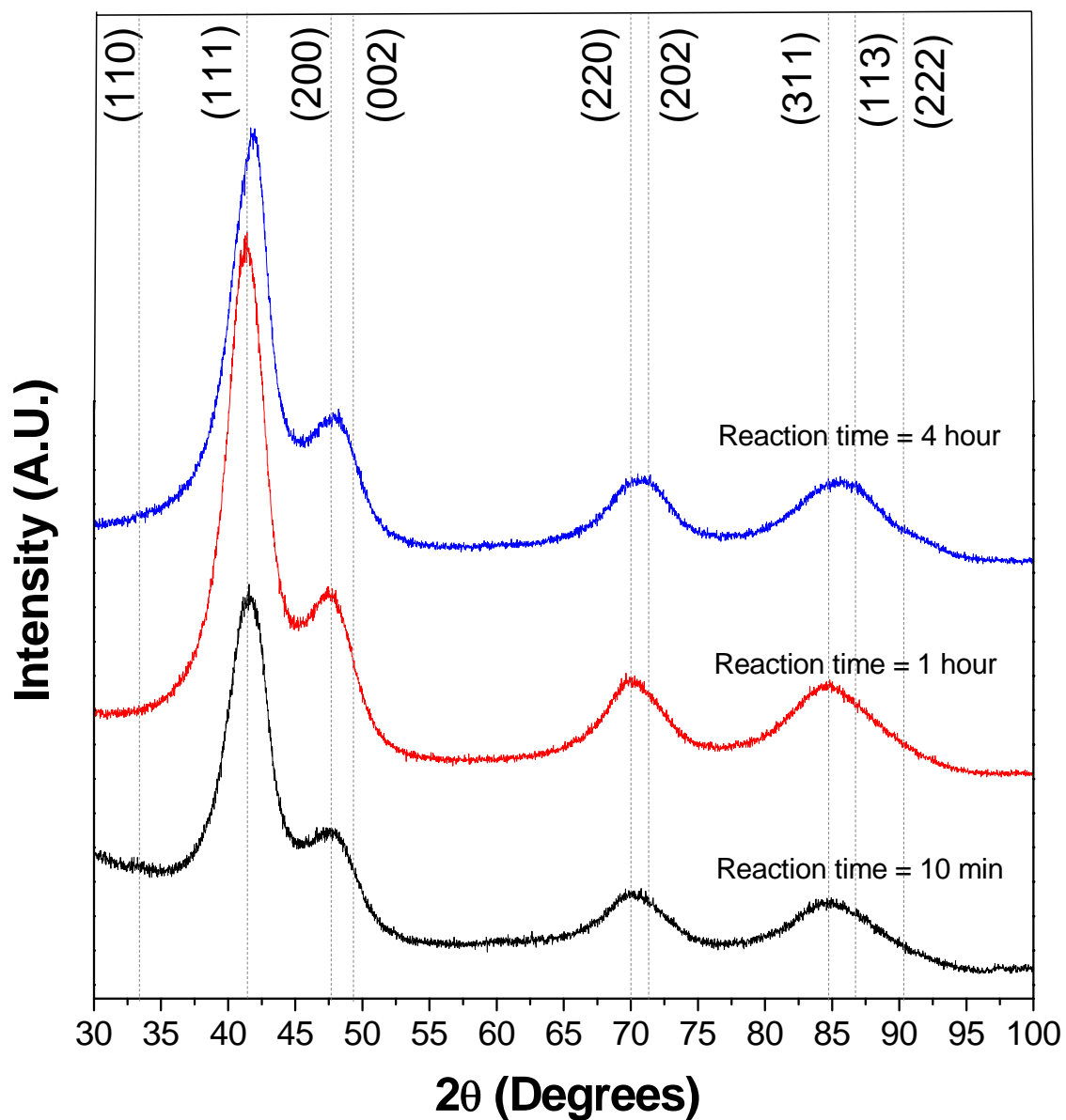


Figure 4.48: XRD patterns at different reaction times of as-synthesized CoPt particles at 'R' = 50, a Pt/Co mole ratio of 0.15 in TMEG at 487 ± 5 K. XRD analysis for 10 min, 1 h and 4 h of reaction time revealed only nanocrystalline fct-CoPt (*).

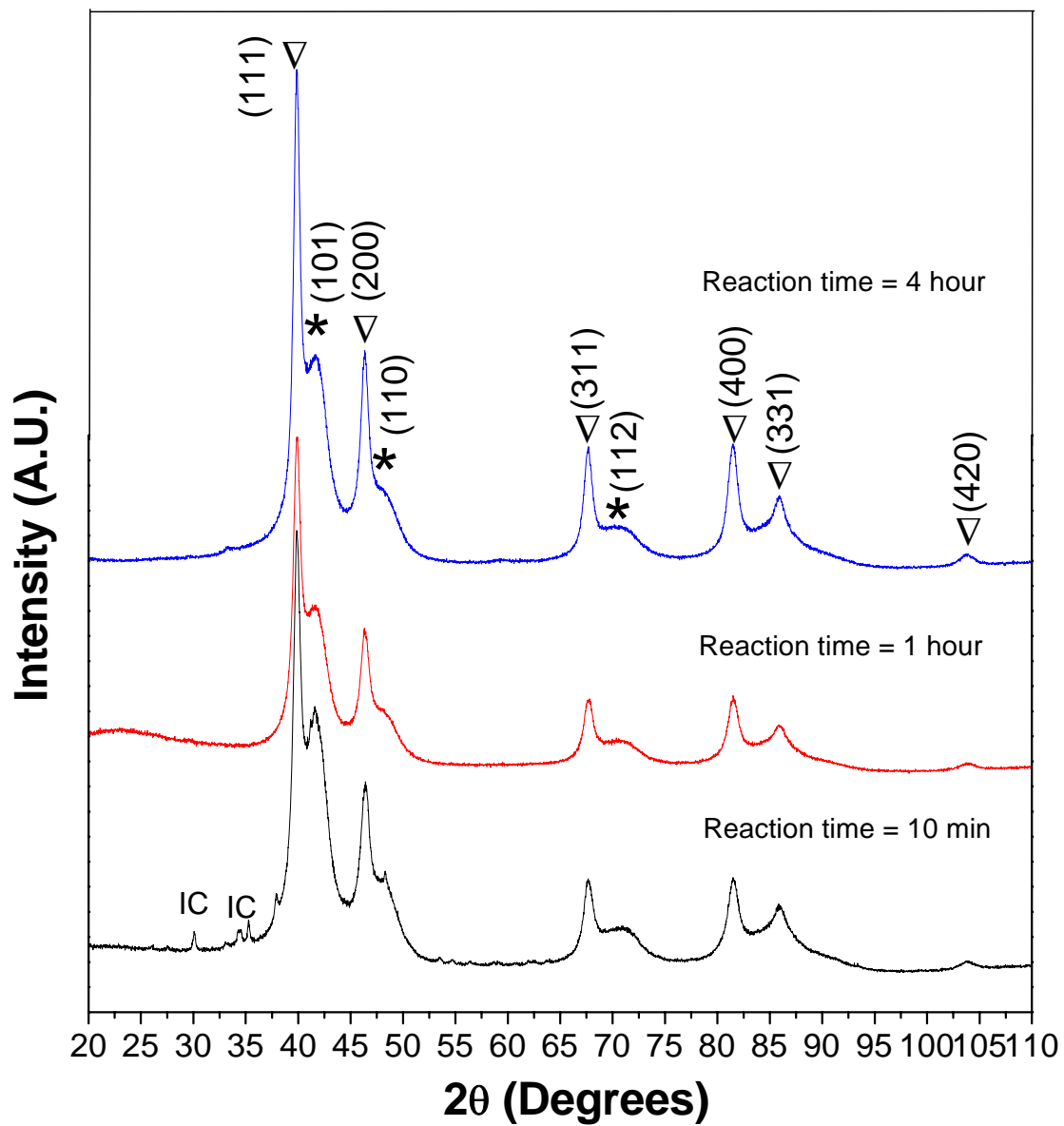


Figure 4.49: XRD patterns at different reaction times of as-synthesized Pt and CoPt nanocrystalline particles at ‘R’= 50, a Pt/Co mole ratio of 1.0 in TMEG at 487 ± 5 K. XRD analysis revealed the coexistence of fcc-Pt (▽) and ordered fct-CoPt (*). Shape picks are from the residual intermediate compound (IC) that disappear in the others patterns.

ii) Magnetic characterization

Figure 4.50 shows the results of the room-temperature M-H measurement for the solids produced at $R = 50$, $[\text{Co}] = 0.0025\text{M}$, $\text{Pt/Co} = 0.15$ for 10 minutes and 1 hour of reaction. The corresponding H_c values were 6 Oe and 2 Oe, respectively. Both samples show non saturated hysteresis loops, typical of superparamagnetic particles. This consideration is supported by the XRD data that showed an average crystallite size of 1.5 nm, which is below the superparamagnetic limit of 4nm for fct-CoPt nanocrystals. This factor would also explain the minimum coercivities observed in these two samples. Further thermal treatment or the synthesis at higher temperatures could be conducive to larger crystallite sizes in these materials.

Figure 4.51 shows the M-H loops for the solids produced at a Pt/Co mole ratio of 1.0 after 10 minutes and 1 hour of reaction. The H_c values varied between 23 and 53 Oe, respectively. Once again, these samples are not magnetically saturated. The presence of superparamagnetic particles should then be considered also in this case. The rise in the maximum magnetization after 1 hour of reaction can be consequence of the completion of the reduction reaction after fully conversion of the intermediate into the metallic phase. Although small, the coercivity of the sample produced after one hour of reaction (53 Oe) at $\text{Pt/Co} = 1.0$ was higher than the coercivity for the sample produced at a lower Co/Pt mole ratio (0.15), despite the larger fraction of elemental Pt. It can be due to the presence of larger crystals of the ferromagnetic fct-CoPt phase.

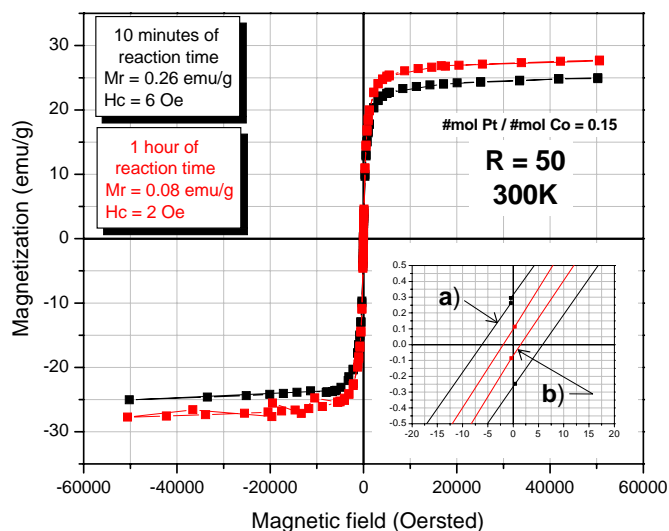


Figure 4.50: M-H loop for cobalt platinum particles synthesized at 0.0025 M $\text{Co}(\text{acac})_2$, a Pt/Co mole ratio of 0.15 in TMEG for a) 10 minutes and b) 1 hour of reaction time in TMEG at 487 ± 5 K. The insert show the M-H loop around the origin.

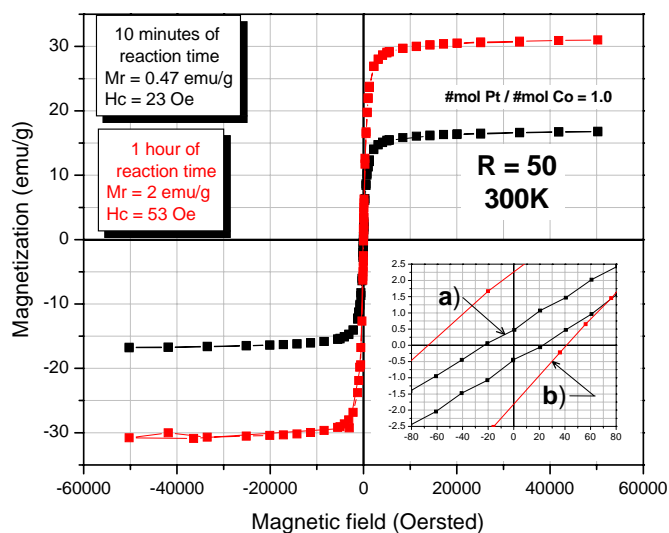


Figure 4.51: M-H loop for cobalt platinum particles synthesized at 0.0025 M $\text{Co}(\text{acac})_2$ and a Pt/Co mole ratio of 1.0 in TMEG for a) 10 minutes and b) 1 hour of reaction time in TMEG at 487 ± 5 K. The insert show the M-H loop around the origin.

5 CONCLUDING REMARKS

We have verified that a suitable control of the synthesis conditions could lead to metastable phases in the Co and Co-Pt nanocrystalline systems; basically, the stability conditions of cobalt phases were found to be strongly dependent on the rate of the metal forming reaction and cooling conditions. The control of the reaction kinetics was achieved through a suitable selection of the solution chemistry in the Polyol-Co (II) system; the presence of hydroxyl ions, the type of cobalt precursor salt and the co-existence of Pt ions (in the Co-Pt system) not only accelerated the formation of the magnetic phase but also affected the stability conditions of the metallic precipitate, and hence of the corresponding magnetic properties. The co-existence of Pt ions in starting solutions not only promoted the nucleation rate and accelerated the cobalt reduction but also induced the formation of ordered fct-CoPt nanocrystals at low temperature (487 K). Quenching of solutions at the end of the reaction time should have also played an important role in producing the identified metastable phases.

Depending on the OH/Co mole ratio, 'R', and the type of cobalt precursor salt, hexagonal close packed (hcp), face centered cubic (fcc), and metastable pseudo-cubic epsilon cobalt (ϵ -Co) phases were formed in tri-methylene glycol (TMEG) under boiling conditions. To the best of our knowledge, the direct formation of nanocrystalline ϵ -Co, a pseudo-cubic modification, in TMEG is reported here for the first time. The hcp- and fcc-Co phases were also presented depending on the synthesis conditions, although in minor proportions. The ϵ -Co phase was the predominant one for the following set of

experimental conditions: 'R' = 50, cobalt acetylacetonate as precursor salt, 0.0025M Co, 487K and 4 hours of reaction. The corresponding lattice parameter was 'a' = 6.219 Å, which is in good agreement with reported values in the literature. The average crystallite size, estimated by the Williamson-Hall approach, was 16.4nm. For the same sample, the micro-strain was estimated at 0.05%. Although minor, the presence of the micro-strain can be attributed to the extremely fast cooling conditions, quenching, of the solution at the end of the reaction time. The corresponding H_c and M_s values were 80 Oe and 97 emu/g, respectively. The relatively low coercivity value is in agreement with the expected magnetic softness of the epsilon phase.

The presence of Pt ions accelerated the formation of the magnetic metastable phases drastically. The magnetic phase was formed at a reaction time as short as 10 minutes, in presence of Platinum ions provided by the hexa-chloro platinate salt in comparison with the 4 hours required when no Pt ions were present. XRD analyses suggested the presence of fcc-Pt as an isolated phase. The presence of elemental Pt is attributed to the earlier reduction of the excess of Pt ions. Cobalt was present as ϵ - and hcp-Co phases. The XRD peaks (110), (111) and (112) were assigned to highly anisotropic fct-CoPt. These results evidenced the viability in producing fct CoPt phase without annealing. This hypothesis was verified by using a strongly complex Pt salt as the acetylacetonate, $Pt(acac)_2$. SQUID analyses suggested that nanocrystals exhibited a predominant ferromagnetic behavior at RT. The H_c became as high as 248 Oe when fct-CoPt, in addition to ϵ - and hcp-Co, was formed.

We report here for the first time the direct formation, i. e. without annealing, of the fct-CoPt phase. When $\text{Pt}(\text{acac})_2$ was used instead of the hexa-chloro platinate salt, the products consisted exclusively of the fct-CoPt phase. The average crystallite size was estimated at 3 nm by using the Scherrer's equation for the (111) peak. This average crystallite size is below the superparamagnetic limit for fct CoPt. SQUID analyses for the solids produced at 'R' = 50, 0.0025M Co in TMEG, 487 K, Pt/Co mole ratio 0.15 and 10 minutes of reaction reported a maximum magnetization of 25 emu/g and a H_c of 6 Oe. These values were determined for a maximum external field of 5T at room temperature conditions. The low coercivity was expected for superparamagnetic fct-CoPt crystals.

Future work will be focused on the optimization of the crystal size in order to overcome the superparamagnetic limit. Based on obtained results we will also study the direct formation of fct-FePt nanocrystals.

REFERENCES

- [1] B. G. Livshits, V. S. Kraposhin and Ya. L. Linetshi, "Propiedades físicas de metales y aleaciones," *Editorial Mir Moscu*. 1982.
- [2] D. Jiles, "Introduction to magnetism and magnetic materials", Chapman&Hall, Chapter 6, p. 135-156, 1998.
- [3] E. F. Kneller and F- E. Luborsky, "Particle Size Dependence of Coercivity and Remanence of Single-Domain Particles," *J, Appl. Phys.* 34, 656, 1963.
- [4] B. D. Cullity, "Introduction to magnetic materials", Addison-Wesely, Chapter 11, p.387, 1972.
- [5] O. Kitakami, T. Sakurai, Y. Miyashita, K. Takeno, Y. Shimada, H. Takano, H. Awqno, K. Ando and Y. Sugita, "Fine metallic particles for magnetic domain observations," *J. Appl. Phys.* Vol. 35, pp. 1724-1728, 1996.
- [6] L. Diandra and D. Reuben, "Magnetic properties of nanostructured materials," *Chem. Mater.* Vol. 8, pp. 1770-1783, 1996.
- [7] D. Weller, A. Moser, L. Folks, M. Best, W. Lee, M. Toney, M. Schwickert, J. Thiele and F. Doerner, "High Ku materials approach to 100 Gbits/in²," *IEEE Transactions on magnetics*, vol. 36, N° 1, pp. 10-15, 1999.
- [8] Powder Diffraction File N° 00-005-0729.
- [9] Powder Diffraction File N° 00-015-0806.
- [10] D. P. Dinega and M. G. Bawendi, "A solution-phase chemical approach to a new crystal structure of cobalt," *Angew. Chem Int.* Vol. 38, pp. 1788-1791, 1999.
- [11] Gunter Schmid. "Nanoparticles from theory to application", Ed. Wiley-VCH, Chapter 3, p 204-230, 2004.
- [12] Y. Yoshizawa, "Magnetic properties and applications of nanostruced soft magnetic materials", *Scripta mater.*, vol. 44, pp. 1321-1325, 2001.
- [13] Powder Diffraction File N° 00-004-0802.
- [14] J. A. Christodoulides, "Thesis: Fabrication and characterization of FePt and CoPt nanoparticles", University of Delaware, 2001.

- [15] J. A. Aboaf, S. R. Herd and E. Klokhorn, "Magnetic Properties and Structure of Cobalt Platinum Thin-Films", IEEE Trans. Magn. 19, 15 14, 1983.
- [16] D. L. Martin, Trans. M E21 2,478, 1958.
- [17] S. Y. Shur, L. M. Magat, G. V. Ivanova, A. I. Mitsek, A. S. Yerrnolenko and O. A. Inanov, "Coercive Force of a Cobalt-Platinum Alloy in the Ordered State", Fiz. Met. Metall. 26 (2), 56, 1968.
- [18] S. H. Liou, Y. Liu, S. S. Malhotra, M. Yu and D. J. Selhnyer, "Magnetic properties of nanometer-size CoPt particles," J: Appl. Phys. 79, 5060, 1996.
- [19] J. M. Pennison, A. Bourret and P. Eurin, "Etude de la Mise en Order de L'Alliage Pt-Co Equiatomique par Microscopic Electronique: An Electron Microscopy Study of the Order Disorder Process in the Equiatomnic Pt-Co Alloy," Acta Metallurgica 19, 1195, 1971.
- [20] Powder Diffraction File N° 00-043-1358.
- [21] T. Sugimoto. "Fine particles: Synthesis, Characterization and Mechanism of growth", Editorial Marcel Dekker, Vol 92, pp. 430-496, 2000.
- [22] D. Larcher and R. Patrice, "Preparation of metallic and alloys polyol media: A thermodynamic approach," J. solid Stage chem.. Vol. 154, pp. 405-411, 2000.
- [23] G. S. Parks, K. K. Kelley and H. M. Huffman, "Thermodynamic properties of organic compounds," J. Am. chem. Soc. Vol. 51, pp. 1969-1973, 1929.
- [24] T. B. Reed, "Free energy of formation of binary compounds," MIT Press, Cambridge, 1971.
- [25] M. Figlarz, C. Ducamp-Sanguesa, F. Fievet and J. P. Lagier, "," Adv. Powder Metall. Particl. Mater Vol. 1, pp. 179, 1992.
- [26] Y. Jin, L. Dennis and S. Majetich, "Nanoscale characterization of magnetic nanoparticles," NanoStructured Materials, vol. 12, pp. 763-768, 1999.
- [27] O. Perales, B. Jeyadevan, N. Chinnasamy, K. Tohji and A. Kasuya, "Solution synthesis of monodispersed nanocrystalline metal particles: The case of cobalt". Proc. Int. Symp. on Cluster Assembled Mater, Series 3, pp. 105-108.

- [28] F. Fievet, J. Lagier and M. Figlarz, "Preparing Monodisperse metal powders in micrometer and submicrometer sizes by the polyol process", MRS bulletin, pp. 29-1325, 2001.
- [29] F. Fiévet, J. P. Lagier, B. Blin, B. Beaudoin and M. Figlarz, "Homogeneous and heterogeneous nucleation in the polyol process for the preparation of micron and submicron size metal particles," Solid State Ionics. 32/33, pp. 198-205, 1989.
- [30] N. Chakroune, G. Viau, C. Ricolleau and F. Fiévet., "Cobalt-based anisotropic particles prepared by polyol process", J. Mater. Chem., vol. 13, pp. 312- 318, 2003.
- [31] C. Chinnasamy, B. Jeyadevan, K. Shinoda and K. Tohji, "Polyol process derived CoPt nanoparticles: Structural and magnetic properties," J. Appl. Phys.. Vol. 93, N° 10, pp. 7583-7585, 2003.
- [32] Vassilios T., Dimitrios N., Gjoka M., Fidler J. and Dimitrios P., "Synthesis of CoPt nanoparticles by a modified polyol method: characterization and magnetic properties", Institute of Physics Publishing, vol. 16, pp. 287- 291, 2005.
- [33] B. D. Cullity, "Elements of x-ray diffraction", Second edition, Ed. Addison-Wesely, 1978.
- [34] Y. Huang, "Thesis: CoPt and FePt nanoparticles for high density magnetic recording", University of Delaware, 2002.
- [35] International Max Planck Research School for Advanced Materials: www.imprs-am.mpg.de
- [36] G. Viau, P. Toneguzzo, A. Pierrard, O. Acher, F. Fievet-Vincent and F. Fiévet, "Heterogeneous nucleation and growth of metal nanoparticles in polyols," *Scripta mater.*, vol. 44, pp. 2263-2267, 2001.
- [37] Powder Diffraction File N° 00-005-0727.
- [38] F. Liu, K. Stoev, X. Shi, H. Tong, C. Chien, Z. Dong, X. Yan, M. Gibbons, S. Funada, Y. Liu, P. Prabhu, S. Dey, M. Schultz, S. Malhotra, B. Lal, J. Kimmal, M. Russak and P. Kern, "Demonstration and characterization of 36 Gb/in² recording sustems," *IEEE Transactions on magnetics*, vol. 36, N° 5, pp. 2140-2142, 2000.
- [39] C. Petit, S. Rusponi and H. Brune, "Magnetic properties of cobalt and cobalt-platinum nanocrystals investigated by magneto-optical Kerr effect," J. Appl. Phys.. Vol. 95, N° 8, pp. 4251-4260, 2004.

- [40] Chen Chen, O. Kitachkani, S. Okamoto and Y. Shimada, "Large coercivity and granular structure of CoPt/SiO₂ films," IEEE Trans. Magn.. Vol. 35, N° 5, pp. 3466-3468, 1999.